Ph.D. Thesis

Probing Electroweakly Interacting Massive Particles with Drell-Yan Process at 100 TeV Colliders

So Chigusa

Department of Physics

THE UNIVERSITY OF TOKYO

December 2019

Abstract

(♣ **To be written** ♣) The main part of this thesis is based on our works [1, 2].

Acknowledgments

I would like to thank my supervisor, Takeo Moroi, who provided stimulating discussions, helpful comments, fruitful suggestions and collaboration and proofread the earlier version of this thesis.

(♣ **Appreciate more** ♣)

Contents

Section 1

Introduction

1.1 Overview

There are many models that extend the standard model (SM) of the particle physics by introducing weakly interacting massive particles (WIMPs), which have interactions with SM particles whose size is comparable to the electroweak gauge coupling. We have many theoretical and phenomenological motivations to introduce WIMPs, some of which are listed below.

- One of the motivations is the existence of the dark matter (DM) in our universe. When we assume a stable WIMP, its thermal relic abundance agrees with the observation if its mass is of $\mathcal{O}(\text{TeV})$ or so.

- Such $\mathcal{O}(\text{TeV})$ new particle is likely to be discovered by many kinds of experiments such as the dark matter searches and the particle colliders.

- Such $\mathcal{O}(\text{TeV})$ WIMPs often appear in well-motivated ultraviolet (UV) completions of the SM. For example, the following two models contain such WIMPs: the minimally supersymmetric standard model (MSSM) introduced to solve the hierarchy problem and the minimal dark matter (MDM) model that can explain the existence and stability of the DM in a minimal extension of the SM.

Considering the third point, many of the WIMPs in the UV completions mentioned above have non-zero electroweak charges, which explain its weak interaction with SM particles. In this thesis, we would like to focus on such kind of WIMPs and seek ways to search for them.[♮1]

In the MSSM, it is known that the supersymmetric (SUSY) partner of the electroweak gauge bosons or the Higgs boson can be the lightest supersymmetric particles (LSP) and are natural DM candidate. In particular, there are well motivated scenarios where the so-called Higgsino or Wino play the role of the LSP, which transform as doublet and triplet under the weak $SU(2)_L$ gauge symmetry, respectively; light Higgsino is preferred to reduce the amount

---

[♮1]The word "WIMPs" is usually used in a broader sense that includes particles with some unknown weak interactions with SM particles. To distinguish this usage with ours, which only denotes some particles with non-zero electroweak charge, it may be better to call them as "WIMPs", abbreviation of electroweakly interacting massive particles. However, within this thesis, we will just use "WIMPs" in a narrow sense obeying the widely spread custom.

of the fine-tuning of the electroweak scale as in the "natural SUSY" set up [3–6], while the so-called "mini-split" spectrum [7–12] with anomaly mediation [13, 14] makes Wino LSP. Another example, the MDM scenario, introduces a larger $SU(2)_L$ multiplet, whose stability is automatically ensured by the charge assignment. In particular, a 5-plet Majorana fermion with hypercharge zero is a good DM candidate that escape from the DM search experiments so far.

To search for WIMPs, several different approaches are adopted. One way is to rely on DM search experiments, assuming that the WIMPs are the dominant component of the DM. Firstly, there exist several direct detection experiments that utilize a scattering between the DM and the nucleus [15–17]. Wino is the most promising target of these experiments, whose spin independent scattering cross section with a nucleon is almost mass independently given as $\sigma_p^{\rm SI} \simeq 2.3 \times 10^{-47}\,{\rm cm}^2$ [18–22], which is still an order of magnitude below the current experimental limit. It is unlikely to detect Higgsino DM in this way since its small $SU(2)_L$ charge makes scattering cross section comparable to or below the neutrino floor [19]. The detection of MDM may also be difficult [23] since its possibly larger mass of $\mathcal{O}(10)\,{\rm TeV}$ weakens the sensitivity of direct detection experiments.

Secondly, a lot of effort is devoted to detecting cosmic rays resulting from DM annihilation, namely the DM indirect detection [24–27]. Although the results suffer from some astrophysical uncertainties, they have already excluded, for example, Wino with mass less than $400\,{\rm GeV}$ and also around $2\,{\rm TeV}$ [28]. On the other hand, the corresponding Higgsino bound is weaker and it has been probed only up to $350\,{\rm GeV}$ [29] again due to the smallness of its $SU(2)_L$ charge. For the MDM, 5-plet fermion is analyzed as an example in [30] and the mass less than 2 TeV and several narrow regions are excluded. Note again that the WIMPs must be the dominant component of the DM for these approaches to be sensitive.

Another way of probing WIMPs is the direct production at the large hadron collider (LHC). The main strategy is to use the disappearing charged track, which indicates a long-lived charged particle, the charged components of the WIMP in the current case. Both ATLAS and CMS collaborations announced a result of this method with the data of $\sqrt{s} = 13\,{\rm TeV}$ LHC [31–33]. The current lower bound on the mass of the pure Higgsino-like (Wino-like) state is 152 (460) GeV at $95\,\%$ C.L. We can obtain a similar bound for the MDM using the same method [34]. In this method, however, the bound strongly depends on the lifetime of the charged component, which is sensitive to the mass difference between the charged and the neutral components. In particular, it is often the case in the SUSY model that the Higgsino-like LSP and its charged counterpart possess a non-negligible fraction of Wino, which significantly enhances the mass difference compared to the pure Higgsino case. In such a case, the lifetime of the charged component is extremely short, making the disappearing track method challenging. There is another option called mono-X search to search for a new physics signal in general. However, the corresponding bound is usually very weak due to the

large SM background and no bound is imposed on Higgsino at $\sqrt{s} = 14\,\text{TeV}$ LHC [35].

   To acquire somewhat stronger bounds on the WIMPs, independent of the decay product or the lifetime and whether they are the dominant component of the DM or not, it has been discussed that indirect search of WIMPs at collider experiments is useful [36–40]. It utilizes the WIMP loop effect on various observables. We pursue this possibility and study the effects of WIMPs on the oblique correction to the electroweak gauge bosons. In particular, in this paper, we study the prospect of the indirect search method at future $100\,\text{TeV}$ hadron colliders such as FCC-hh at CERN [41–43] or SppC in China [44, 45]. We concentrate on the Drell-Yan process that has two leptons in the final state since it provides a very clean signal without any hadronic jets at least from the final state particles. We will show that it provides a comparable or better experimental reach for Higgsino compared to the direct production search of WIMPs at future colliders [46–49]. This method also provides independent and additional information about Wino and the MDM. Besides, we will reveal that this method is useful to investigate WIMP properties, such as charges, masses, and spins.

1.2   Organization of this thesis

This thesis is organized as follows.

In Sec. 2, we briefly review models with WIMPs considered in the thesis. Sec. 2.1 is devoted to the minimally supersymmetric standard model, while Sec. 2.2 to the minimal dark matter model. The mass splitting among the multiplet, which is a phenomenologically important property of WIMPs, is described in Sec. 2.3. The WIMP properties are summarized in Sec. 2.4.

In Sec. 3, we summarize the WIMP properties as a DM candidate. We show the calculation of thermal relic abundance and derive the required mass for WIMP DMs in Sec. 3.1. (♣ More later ♣)

In Sec. 4, we study the WIMP production at the hadron collider experiments and its detection. Possible production processes and the kinematics of the produced WIMPs are summarized in Sec. 4.1. Using the production processes described here, the current status and the prospect at the future $100\,\mathrm{TeV}$ colliders are reviewed in the following subsections. Sec. 4.2 is devoted to the description of the most promising way for the WIMP search called the disappearing track search. (♣ More later ♣)

In Sec. 5, we discuss our own ideas [1, 2] to probe the one-loop effect of WIMPs on the lepton pair production processes through the precise measurement at $100\,\mathrm{TeV}$ colliders. Here, we will describe our statistical analysis, show the obtained reach for WIMPs, and see the possibility to determine the WIMP properties after its discovery. Conclusions of the thesis are presented in Sec. 6.

In Appendices, we first summarize the conventions and notations used in the thesis in A. Then, we briefly review the $\mathcal{N} = 1$ supersymmetry in Appendix B, the properties of the so-called transverse mass used in our analysis in Appendix D, and the statistical analysis method called the profile likelihood method in Sec. E.

Section 2

Models with WIMPs

There are several examples of models that contain WIMP DM candidates. In this section, two of them are briefly reviewed, which are intensely studied in this thesis: the minimally supersymmetric model (MSSM) described in Sec. 2.1 and the minimal dark matter (MDM) model described in Sec. 2.2. Sec. 2.4 is devoted to the summary table of properties of WIMPs frequently considered below.

2.1   Minimally supersymmetric standard model

(♣ **Summary of SUSY particle names somewhere** ♣)

The MSSM is the simple extension of the SM with $\mathcal{N} = 1$ supersymmetry (SUSY).[♮2] One of the motivations to introduce SUSY is to solve the so-called hierachy (or naturalness) problem [50–52] in the SM. The problem is related to the quantum correction to the SM Higgs boson mass from heavy new physics particles. For example, we can consider the one-loop correction to the Higgs mass from a Weyl fermion f and a complex scalar S as illustrated in Fig. 1. The corrections to the Higgs mass is given by

$$\Delta m_h^2 = -\frac{|\lambda_f|^2}{8\pi^2}\left[\Lambda_{\rm UV}^2 - 2m_f^2 \ln\left(\frac{\Lambda_{\rm UV}}{m_f}\right) + \cdots\right] \qquad \text{(fermion)}, \qquad (2.1)$$

$$\Delta m_h^2 = \frac{\lambda_S}{16\pi^2}\left[\Lambda_{\rm UV}^2 - 2m_S^2 \ln\left(\frac{\Lambda_{\rm UV}}{m_S}\right) + \cdots\right] \qquad \text{(scalar)}, \qquad (2.2)$$

(♣ **Check! Derive MSbar formula?** ♣) where λ_f and m_f are the Higgs-fermion coupling constant and the fermion mass, respectively, while λ_S and m_S are those for the scalar S.
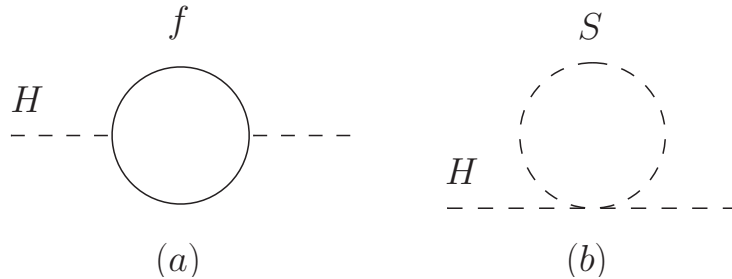

Figure 1: One-loop correction to the Higgs mass from (a) a Weyl fermion f and (b) a complex scalar S.

[♮2] For a brief review of the $\mathcal{N} = 1$ SUSY, see Sec. B.

Notation	$SU(3)_C$	$SU(2)_L$	$U(1)_Y$	boson	fermion
$\hat{Q}_i$	**3**	**2**	1/6	squark	left-handed quark
$\hat{L}_i$	**1**	**2**	−1/2	slepton	left-handed lepton
$\hat{U}_i$	**$\bar{3}$**	**1**	−2/3	squark	right-handed up-type quark
$\hat{D}_i$	**$\bar{3}$**	**1**	1/3	squark	right-handed down-type quark
$\hat{E}_i$	**1**	**1**	1	slepton	right-handed lepton
$\hat{H}_u$	**1**	**2**	1/2	Higgs	Higgsino
$\hat{H}_d$	**1**	**2**	−1/2	Higgs	Higgsino

Table 1:   Notations and quantum numbers of the chiral superfields in the MSSM. Also shown are names of bosonic and fermionic components of each suprefield used in this thesis.

Notation	$SU(3)_C$	$SU(2)_L$	$U(1)_Y$	boson	fermion
$\hat{g}$	**8**	**1**	0	gluon	gluino
$\hat{W}$	**1**	**3**	0	W boson	Wino
$\hat{B}$	**1**	**1**	0	B boson	Bino

Table 2:   Notations and quantum numbers of the vector superfields in the MSSM. Also shown are names of bosonic and fermionic components of each suprefield.

We take the cut-off scale of the theory to be Λ_{UV} to regularize the otherwise divergent loop integral and neglect the lower order terms of Λ_{UV}. Eqs. (2.1) and (2.2) show the quadratic dependence of Δm_H^2 on Λ_{UV}, which means that the Higgs mass is sensitive to the energy scale of the beyond the SM physics. However, there is at least one extremely high energy scale physics in nature, gravity at the Planck scale $M_{\mathrm{pl}} \sim 10^{18-19}\,\mathrm{GeV}$. By substituting $\Lambda_{\mathrm{UV}} = M_{\mathrm{pl}}$ in Eqs. (2.1) and (2.2) and assuming $\lambda_f \sim \lambda_S \sim \mathcal{O}(1)$, we notice that orders-of-magnitude fine-tuning is required to obtain the correct Higgs mass $m_h = 125.10\,\mathrm{GeV}$ [53], which is unnatural.

SUSY provides a nice solution to this fine-tuning problem. As is summarized in Appendix B, each Weyl fermion in a supersymmetric model is accompanied by two complex scalars with the same mass $m_f = m_S$. In addition, their coupling constants to the Higgs boson should have a relationship $|\lambda_f|^2 = \lambda_S$ due to the fact that λ_S is a coupling constant in the F-term potential sourced by a superpotential term proportional to λ_f. By using both equations and summing the corrections (2.1) and (2.2) with a factor of two multiplied to the latter, we obtain a result independent of the cut-off scale Λ_{UV} without fine-tuning. This cancellation is ensured by the so-called non-renormalization theorem. [54, 55]

We now summarize the notations and quantum numbers of the chiral and vector su-

perfields in the MSSM in Table 1 and 2, respectively. In the tables, we also summarize the names of bosonic and fermionic components of each superfield used in this thesis. The supersymmetric part of the MSSM Lagrangian is described by the superpotential[♮3]

$$W = Y_u^{ij}\hat{U}_i\hat{Q}_j\hat{H}_u - Y_d^{ij}\hat{D}_i\hat{Q}_j\hat{H}_d - Y_e^{ij}\hat{E}_i\hat{L}_j\hat{H}_d + \mu\hat{H}_u\hat{H}_d, \tag{2.3}$$

where $i, j = 1, 2, 3$ labels the quark and lepton generation, while Q, L, U, D, E are superfields that contain the left-handed quark, left-handed lepton, right-handed up-type quark, right-handed down-type quark, and right-handed charged lepton, respectively. In Eq. (2.3), proper contraction of $SU(3)_C$ and $SU(2)_L$ indices is assumed. Note that two Higgs doublets H_u and H_d with opposite values of $U(1)_Y$ hypercharges are introduced, which is needed to cancel the contributions to the gauge anomaly from fermionic partners of the Higgs doublets.

Postulating SM gauge symmetries as a unique guideline to construct a model, there are a few more terms allowed in the superpotential:

$$W_{\Delta L=1} = \lambda^{ijk}\hat{L}_i\hat{L}_j\hat{E}_k + \lambda'^{ijk}\hat{L}_i\hat{Q}_j\hat{D}_k + \mu^i\hat{L}_i\hat{H}_u, \tag{2.4}$$

$$W_{\Delta B=1} = \lambda''^{ijk}\hat{U}_i\hat{D}_j\hat{D}_k, \tag{2.5}$$

where $\Delta L = 1$ and $\Delta B = 1$ represents the breaking of the lepton and baryon numbers by one, respectively. These terms with a lepton or baryon number breaking are phenomenologically problematic since they may cause a too fast proton decay, depending on parameters (see for example [57]). To avoid this problem, we often rely on a symmetry called the R-parity [58] or the matter parity [57, 59–61]. Charges of the R-parity, which is basically a Z_2 symmetry, are calculated as

$$P_R = (-1)^{3(B-L)+2s}, \tag{2.6}$$

where B, L, and s are the baryon number, lepton number, and spin of the particle, respectively. According to the definition, we can see that all the SM particles have even parity ($P_R = +1$), while all the supersymmetric particles have odd parity ($P_R = -1$). Then it is easy to check that Eqs.(2.4) and (2.5) lead to the R-parity violating terms in the Lagrangian and thus are forbidden, while all the terms in Eq. (2.3) are allowed. From now on, we only focus on the R-parity preserving MSSM.

Since no superpartner of any SM particle is observed yet, SUSY should be broken at some scale to give large masses to superpartners. The SUSY breaking part of the Lagrangian is

---

[♮3]For a more detailed review of the MSSM, see for example [56].

expressed as

$$\begin{aligned}
\mathcal{L}_{\text{soft}} = -\,\frac{1}{2}&\left(M_3 \tilde{g}\tilde{g} + M_2 \tilde{W}\tilde{W} + M_1 \tilde{B}\tilde{B} + \text{h.c.} \right)\\
&-\left(A_u^{ij} \tilde{U}_i \tilde{Q}_j H_u - A_d^{ij} \tilde{D}_i \tilde{Q}_j H_d - A_e^{ij} \tilde{E}_i \tilde{L}_j H_d \right)\\
&-m_Q^{2ij}\tilde{Q}_i^\dagger \tilde{Q}_j - m_L^{2ij}\tilde{L}_i^\dagger \tilde{L}_j - m_U^{2ij}\tilde{U}_i^\dagger \tilde{U}_j - m_D^{2ij}\tilde{D}_i^\dagger \tilde{D}_j - m_E^{2ij}\tilde{E}_i^\dagger \tilde{E}_j\\
&-m_{H_u}^2 H_u^* H_u - m_{H_d}^2 H_d^* H_d - (b H_u H_d + \text{h.c.})\,, \tag{2.7}
\end{aligned}$$

where the tilde is used to express the superpartner of the SM particle contained in a superfield, while fields without hat nor tilde denote particles in the SM. An exception is two Higgs doublets, where H_u and H_d express the scalar components, while $\tilde{H}_u$ and $\tilde{H}_d$ express their superpartners called Higgsinos. The SM-like Higgs doublet H corresponds to a linear combination of H_u and H_d, while the other combination becomes heavy.

It is known that, within the MSSM, almost all SUSY breaking mechanisms, such as the F-term (O′Raifeartaigh) [62] or D-term (Fayet-Iliopoulos) SUSY breaking [63, 64], fail to generate masses of superpartners with remaining the SM gauge group in the low energy effective theory. Thus, we need a so-called hidden sector in addition to the MSSM sector, in which SUSY is spontaneously broken. For the MSSM sector to have Lagrangian terms (2.7), we also need some mediation mechanism of the SUSY breaking. The relative size of the SUSY breaking parameters in Eq. (2.7) and thus the phenomenology of the model highly depends on the mediation mechanism. Among many mediation mechanisms of SUSY breaking, the anomaly mediated SUSY breaking [13, 14] leads to an interesting phenomenology with relatively light WIMPs, so it will be reviewed later.

Dark matter candidate in the MSSM

There is another motivation to consider the R-parity preserving MSSM; it naturally contains the candidate for DM. Since there is a sizable amount of DM in the current universe, a DM candidate should be stable or have a sufficiently small decay width. In many models, the stability of DM is ensured by imposing a symmetry and/or by kinematically forbidding the DM decay. In the MSSM, the role of stabilizer can be played by the R-parity described above. Recalling that all the SM (supersymmetric) particles have even (odd) parity, each interaction vertex in the MSSM Lagrangian should contain an even number of supersymmetric particles. If we consider the lightest supersymmetric particle (LSP), such vertices can not construct the kinematically allowed LSP decay chain and, as a result, the LSP becomes a stable DM candidate.

The DM phenomenology, such as the production and annihilation of DM in the universe and processes that allow us to efficiently detect it, highly depends on which species of the supersymmetric particle becomes the LSP. Hereafter, we only focus on the cases where one

Value	Description	Reference
$M_W = 80.384 \pm 0.014\,\mathrm{GeV}$	Pole mass of the W boson	[65, 66]
$M_Z = 91.1876 \pm 0.0021\,\mathrm{GeV}$	Pole mass of the Z boson	[67]
$M_h = 125.15 \pm 0.24\,\mathrm{GeV}$	Pole mass of the Higgs	[68, 69]
$M_t = 173.34 \pm 0.82\,\mathrm{GeV}$	Pole mass of the top quark	[70]
$\left(\sqrt{2}G_\mu\right)^{-1/2} = 246.21971 \pm 0.00006\,\mathrm{GeV}$	Fermi constant for μ decay	[71]
$\alpha_3(M_Z) = 0.1184 \pm 0.0007$	$\overline{\mathrm{MS}}$ $SU(3)_C$ gauge coupling	[72]

Table 3: Experimentally measured SM parameters used for the derivation of Eq. (2.9).

of the gauginos and Higgsinos becomes the LSP, whose motivations are described below. Besides, all the LSP candidates described below (*i.e.,* Wino and Higgsino) have non-zero electroweak charges and they can be viewed as examples of the WIMPs.

Higgs mass in the MSSM

Under the spontaneously or softly broken SUSY, the cancellation of the quantum correction to the Higgs boson mass discussed above is not exact. One obvious consequence of the SUSY breaking in Eqs. (2.1) and (2.2) is the hierarchy between m_f and m_S that appear in the second term of each contribution. In the case of the MSSM, the largest contribution comes from the superpartner of the top quark, stop, which has the largest Yukawa coupling with the Higgs boson.

When there is a large hierarchy between the SUSY breaking scale M_S, which is comparable to stop masses, and the top mass M_t, the stop contributions to the Higgs mass contains a large logarithm of the form of $\log(M_S^2/M_t^2)$. To resum the large logarithm and obtain a precise result, it is easy to rely on the renormalization group equation (RGE). In this framework, the value of the Higgs self-coupling λ at the electroweak scale is closely related to the Higgs mass. We define the potential for the SM Higgs doublet H as

$$V(H) = -\frac{m^2}{2}|H|^2 + \lambda|H|^4, \tag{2.8}$$

and assume the SM parameters summarized in Table 3. Then, according to [73], we obtain the relationship[♮4]

$$\lambda(M_t) = 0.12604 + 0.00206\left(\frac{M_h}{\mathrm{GeV}} - 125.15\right) - 0.00004\left(\frac{M_t}{\mathrm{GeV}} - 173.34\right), \tag{2.9}$$

[♮4]Although the values listed in Table 3 are different from the latest ones given in [53], we use older ones because the change in input values may cause the slight change in coefficients of second and third terms of Eq. (2.9). The latest central values of the Higgs and top masses are $M_h = 125.10\,\mathrm{GeV}$ and $M_t = 173.1\,\mathrm{GeV}$, with which we can estimate $\lambda(M_t) = 0.12595$.
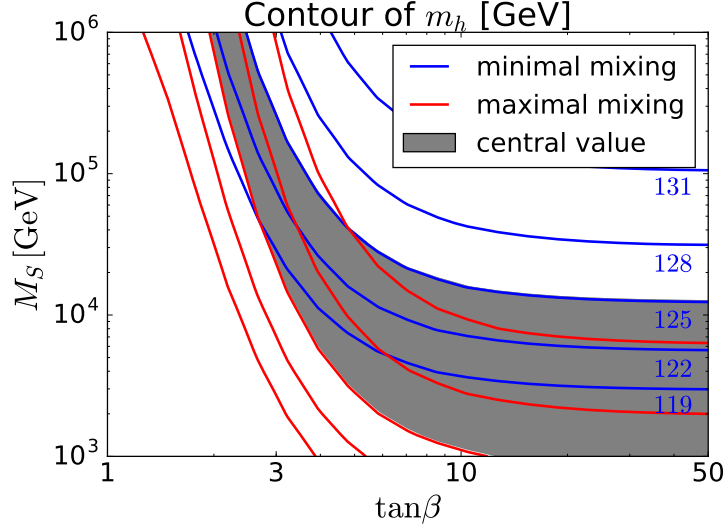
Figure 2:   Contour of the Higgs mass m_h in the $\tan\beta$ vs. M_S plane. The universal mass M_S is assumed for all the SUSY particles. Blue (red) lines correspond from top to bottom to the contours of $m_h = 131, 128, 125, 122, 119\,\text{GeV}$ for the minimal (maximal) stop mixing. Gray shade corresponds to the region where $m_h = 125.10\,\text{GeV}$ can be explained.

where the $\overline{\text{MS}}$ scheme is used to renormalize the divergence of loop integrals.

In the MSSM, the value of λ at the SUSY breaking scale M_S is given by

$$\lambda(M_S) = \frac{g_1^2(M_S) + g_2^2(M_S)}{8} \cos^2 2\beta + \delta\lambda, \tag{2.10}$$

where g_1 and g_2 are $U(1)_Y$ and $SU(2)_L$ gauge coupling constants, respectively, while β parametrizes the ratio of the vacuum expectation values

$$\frac{\langle H_u^0 \rangle}{\langle H_d^0 \rangle} = \tan\beta, \tag{2.11}$$

with H_u^0 and H_d^0 being electromagnetically neutral components of the corresponding Higgs doublets. In Eq. (2.10), the first term shows the tree-level contribution from the D-term potential and $\delta\lambda$ denotes the threshold correction from heavy superpartners. M_S is often chosen to be the geometric mean of stop masses to minimize the largest contribution to $\delta\lambda$ from stops. Once the spectrum of the MSSM particles is fixed, we can evaluate the Higgs self-coupling using Eq. (2.10), calculate its running according to the RGE, and obtain the prediction for the Higgs mass through Eq. (2.9).

In Fig. 2, we show the contour plot of the Higgs mass m_h in the $\tan\beta$ vs. M_S plane. We assume the universal mass M_S for all the SUSY particles. Under this assumption, the

largest contribution to the threshold correction $\delta\lambda$ from stops is expressed as

$$\delta\lambda \simeq \frac{9y_t^2(M_S)}{16\pi^2}\tilde{X}_t\left[1 - \frac{\tilde{X}_t}{12}\right], \tag{2.12}$$

$$\tilde{X}_t \equiv \frac{(A_t - \mu\cot\beta)^2}{M_S^2}, \tag{2.13}$$

with $y_t \equiv Y_u^{33}$ and $A_t \equiv A_u^{33}$. It is obvious from Eq. (2.12) that, for a moderate value of $\tilde{X}_t \lesssim \mathcal{O}(1)$, $\tilde{X}_t = 0$ ($\tilde{X}_t = 6$) corresponds to the case with minimum (maximum) threshold correction, often called as the minimal (maximal) stop mixing.[♮5]

The red (blue) lines in Fig. 2 denote from top to bottom the contours of $m_h = 131$, 128, 125, 122, 119 GeV for the minimal (maximal) stop mixing. Gray shade corresponds to the region where the central value of the observation $m_h = 125.10$ GeV can be explained. From the figure, we can see that the discovery of the Higgs with $m_h = 125.10$ GeV may indicate a somewhat heavy SUSY breaking scale $M_S \gtrsim 10$ TeV for the case with a small stop mixing or a small $\tan\beta$. Combined with the fact that there is still no sign of the superpartners at the collider experiment, this motivates us to consider a heavy SUSY scenario.

Light Higgsino and its relation to the naturalness

When we consider a heavy SUSY model concerning the Higgs mass, there is another problem called the little hierarchy problem. This mentions the hierarchy between the electroweak scale and the heavy SUSY breaking scale and an accompanying fine-tuning. Although the degree of the required fine-tuning is several orders of magnitude smaller than that for the large hierarchy between the electroweak and Planck scales, it will be more acceptable if some mechanism relieves the fine-tuning. The required fine-tuning can be clearly expressed in the equation

$$\frac{1}{2}m_Z^2 = \frac{m_{H_d}^2 - m_{H_u}^2\tan^2\beta}{\tan\beta^2 - 1} - \mu^2, \tag{2.14}$$

where the right-handed side is the MSSM prediction for the Z-boson mass assuming the successful electroweak symmetry breaking. If some of the MSSM parameters m_{H_d}, m_{H_u}, μ are much larger than m_Z, there should be some amount of fine-tuning to satisfy the equation.

There is a measure of the fine-tuning in this sense, proposed in [74, 75]:

$$\Delta_{a_i} \equiv \frac{a_i}{m_Z^2}\frac{\partial m_Z^2}{\partial a_i}, \tag{2.15}$$

[♮5]Eq. (2.12) shows that $\delta\lambda < 0$ for $\tilde{X}_t > 12$, resulting in the prediction of a lighter Higgs mass than the minimal stop mixing case. However, the parameter space with $\tilde{X}_t \gtrsim 6$ is severely constrained by the requirement of the stability of the electroweak vacuum (♣ **Citation** ♣) and is not considered here.

where a_i is an MSSM model parameter. In order for the model to be "natural", we require $|\Delta_{a_i}| < \Delta$ for any a_i with a typical choice of $\Delta \sim \mathcal{O}(10-100)$. Since m_Z is sensitive to the Higgsino mass μ, this gives an upper bound on the "natural" choice of the Higgsino mass

$$\mu^2 < \frac{m_Z^2}{2}\Delta, \tag{2.16}$$

predicting the (sub-)TeV scale Higgsino. As we will see in Sec. 3.1, the light Higgsino is also fascinating as a dark matter candidate.

Even when the SUSY breaking scale is much higher than the electroweak scale, it is not strange for Higgsino to be around the electroweak scale since it is protected by an R-symmetry and a Peccei Quinn symmetry. (♣ **Definition?** ♣) The symmetry protection is also important for a solution to the so-called "μ-problem" [76], where the large hierarchy between the SUSY preserving parameter μ and the cut-off scale of the MSSM such as $M_{\rm pl}$ is discussed. When we consider the low energy effective field theory in which SUSY is broken and all the squarks and sleptons are decoupled, a unique linear combination of the R-symmetry and the Peccei Quinn symmetry is enhanced only if both gauginos and Higgsinos are massless. This fact leads to the framework of the split SUSY [10], in which there is a hierarchy between the masses of Higgsinos/gauginos and the other SUSY particles. In this framework, the phenomenology is determined by the ordering and hierarchy of Higgsino and gaugino masses. In particular, the collider phenomenology of Higgsino will be summarized in Sec. 4 for the case when gauginos are heavier than Higgssino.

Finally, the naturalness requirement discussed above also imposes an upper bound on other parameters, in particular, on $m_{H_u}^2$ for $\tan^2\beta \gg 1$. The small value of $m_{H_u}^2$ can be realized by the focus point mechanism [77–79], where the choice of the SM parameters in our universe, in particular that of y_t, allows $m_{H_u}^2$ at the low energy scale to be insensitive to its boundary condition at the high energy scale.

Light Wino in the anomaly mediated SUSY breaking model

Among many heavy SUSY models, the anomaly mediated SUSY breaking [13, 14] and the pure gravity mediation scenario based on it [80–82] is of particular interest since it naturally predicts the existence of WIMPs (in particular Winos denoted as $\tilde{W}$) in the TeV range. In this scenario, the SUSY breaking effect is directly mediated to the quark and lepton supermultiplets, and they obtain masses comparable to the scale of the SUSY breaking, which is roughly equal to the gravitino mass $m_{3/2}$. Higgsino is also considered to be heavy contrary to the model described above. In fact, it is easy to realize the hidden sector dynamics that generates the μ-term of $\mathcal{O}(m_{3/2})$. On the other hand, the superpartners of gauge bosons, gauginos, feel the SUSY breaking effect only through a one-loop diagram, which is related to the conformal anomaly. As a result, gaugino mass parameters in Eq. (2.7) are one-loop

suppressed compared with other mass parameters and given by

$$M_i(M_S) = - \left.\frac{\beta_i}{2g_i^2}\right|_{M_S} m_{3/2}, \tag{2.17}$$

where $i = 1, 2, 3$ is a gauge index and β_i denote the beta functions of gauge coupling constants. (♣ M_S? $M_{\rm GUT}$? ♣) At the one-loop level, this gives

$$M_1(M_S) = \frac{11g_1^2(M_S)}{16\pi^2} m_{3/2}, \tag{2.18}$$

$$M_2(M_S) = \frac{g_2^2(M_S)}{16\pi^2} m_{3/2}, \tag{2.19}$$

$$M_3(M_S) = -\frac{3g_3^2(M_S)}{16\pi^2} m_{3/2}. \tag{2.20}$$

Since Higgsinos are assumed to have a mass comparable to $m_{3/2} \sim M_S$, they decouple from the effective theory below the scale M_S. To take account of the correction to the gaugino masses from the Higgs-Higgsino loop, one has to include the threshold correction at M_S

$$\Delta M_1 = \frac{g_1^2(M_S)}{16\pi^2} L, \quad \Delta M_2 = \frac{g_2^2(M_S)}{16\pi^2} L, \tag{2.21}$$

with

$$L \equiv \mu \sin 2\beta \frac{m_A^2}{|\mu|^2 - m_A^2} \ln \frac{|\mu|^2}{m_A^2}, \tag{2.22}$$

where m_A is the mass of the heavy CP-odd Higgs.

Below M_S, gaugino mass parameters further run towards the gaugino mass scale $M_{\tilde{G}}$, where the physical gaugino masses are determined. Note that the Bino and Wino masses are well approximated by $|M_1(M_{\tilde{G}})|$ and $|M_2(M_{\tilde{G}})|$, while the gluino pole mass $m_{\tilde{g}}$ includes a sizable effect from the threshold correction as [10]

$$m_{\tilde{g}} = |M_3(M_{\tilde{G}})| \left[1 + \frac{g_3^2}{16\pi^2} \left(12 + 9 \ln \frac{M_{\tilde{G}}^2}{|M_3|^2} \right) \right]. \tag{2.23}$$

The gaugino scale is often defined through $M_3(M_{\tilde{G}}) = M_{\tilde{G}}$ to make the logarithmic term in Eq. (2.23) vanish.

In Fig. 3, we show the dependence of gaugino masses on $m_{3/2}$ and L. In the left panel, we take $\tan \beta = 2.5$ and $L = 0$, and the $m_{3/2}$ dependence is shown. Blue, green, and red lines denote the masses of Bino, Wino, and gluino, respectively. We can see that, throughout the parameter region used here, Wino becomes the lightest gaugino and becomes the LSP
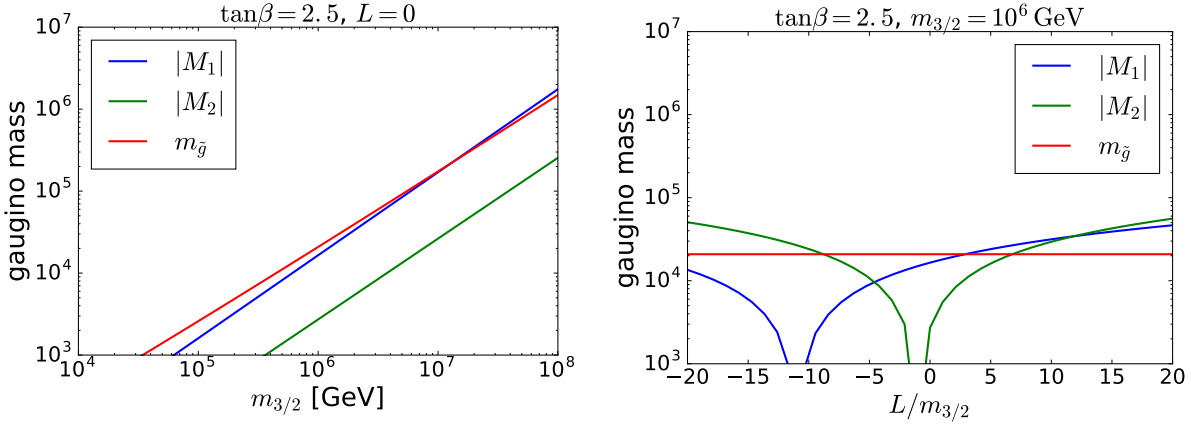
Figure 3:   Gaugino masses as a function of $m_{3/2}$ with a fixed value of $L = 0$ (left) and that of $L/m_{3/2}$ with a fixed value of $m_{3/2} = 10^6 \, \text{GeV}$ (right). Blue, green, and red lines denote the masses of Bino, Wino, and gluino, respectively. $\tan \beta = 2.5$ is used in both figures.

that can be a dark matter candidate. In this choice of parameters, $m_{3/2} = 10^6 \, \text{GeV}$ roughly corresponds to the observed value of the Higgs mass $m_h \sim 125 \, \text{GeV}$, which at the same time realizes the $\mathcal{O}(1) \, \text{TeV}$ mass for Wino. As we will see in Sec. 3.1, the Wino dark matter in this mass range is well-motivated since it gives us a collect relic abundance of the dark matter.

In the right panel of Fig. 3, we also show the L dependence of gaugino masses for $\tan \beta = 2.5$ and $m_{3/2} = 10^6 \, \text{GeV}$. For simplicity, we neglect the relative phase of $m_{3/2}$ and L and only consider the relative sign of them. It can be seen that the hierarchy between gaugino masses is changed when a large value of $|L|$ is considered. However, we can safely say that when the threshold correction is sufficiently small, $|L| \lesssim \mathcal{O}(m_{3/2})$, Wino remains to be the LSP. Besides, the dependence of m_h on L is negligibly small and m_h changes only $\mathcal{O}(0.1) \, \text{GeV}$ within the parameter choice of the right panel.

2.2   Minimal dark matter model

The MDM [83–85] is another example model that contains a WIMP DM candidate. This model attempts to explain the existence of stable DM by extending the SM as simply as possible. More specifically, we just assume the same gauge groups as the SM and add only one $SU(2)_L$ n-plet with $U(1)_Y$ hypercharge Y in the model.[♮6] Y is chosen such that one component of the multiplet, after the electroweak symmetry breaking, has vanishing $U(1)_{\text{EM}}$

[♮6]This new particle, even if it is a fermion, does not contribute to the $SU(2)_L^2 \, U(1)_Y$, $U(1)_Y^3$, nor $U(1)_Y \, \text{grav}^2$ anomalies when $Y = 0$. When $Y \neq 0$, we always consider a vector-like pair of Weyl fermions, similar to the Higgsinos $\tilde{H}_u$ and $\tilde{H}_d$, which as a whole consists of a Dirac fermion and cancels the contributions to the gauge anomalies.

charge, and thus can be a DM candidate. This condition leaves only n discrete choices of Y for an $SU(2)_L$ n-plet.

In the $SU(2)_L$ limit, masses of all the components in the multiplet are the same. Since $SU(2)_L$ symmetry is spontaneously broken, the mass difference among them is generated at the one-loop level and a heavy component can decay into a lighter component. For the multiplet to explain the DM in the current universe, the $U(1)_{\text{EM}}$ neutral component should have the lowest mass. We will return to this point in Sec. 2.3.

In some sense, WIMPs contained in the MSSM can also be viewed as an example of the MDM (if we assume all the other superpartners are decoupled). In fact, if we choose the set of $SU(2)_L$ and $U(1)_Y$ charges as $(n, Y) = (2, \pm 1/2)$ and $(3, 0)$, they correspond to the Higgsino and Wino, respectively. However, for these choices, the stability of the $U(1)_{\text{EM}}$ neutral component is not automatically ensured, and some extra symmetry (in this case the R-parity) is needed for the DM to survive until now. The important point of the new framework MDM is that, when we use large $n \geq 5$, there are examples of multiplets that automatically contain a sufficiently long-lived DM candidate.

The stability of such multiplets can be understood through a simple group theoretical argument. To write down the effective operator that describes the decay of a n-plet field to SM particles, we have to make a n-plet representation out of several SM fields. However, since the largest $SU(2)_L$ representation in the SM is doublet, we need at least $n-1$ SM fields in the operator. The operator made out of this large number of fields should be suppressed by a power of the cutoff scale Λ, at least by Λ^{4-n} (Λ^{3-n}) for a scalar (fermion) MDM, and results in a small decay rate. Since the well-motivated DM mass is of $\mathcal{O}(\text{TeV})$ as we will see in Sec. 3.1, the resulting lifetime of the DM candidate is estimated as $\tau \sim \Lambda^{-2p}(\text{TeV})^{2p-1}$ for an operator with a suppression factor Λ^{-p}. By demanding τ to be larger than the age of the universe under the assumption for the cut off scale $\Lambda < M_{\text{pl}}$, we can conclude that the operator of the DM decay should have a dimension larger than five. Then, we recast this condition to that for n and obtain

$$n \geq \begin{cases} 6 & \text{for scalar MDM,} \\ 5 & \text{for fermion MDM.} \end{cases} \tag{2.1}$$

On the other hand, since we consider large $SU(2)_L$ multiplets, the RGE running of the $SU(2)_L$ gauge structure constant α_2 above the MDM mass is drastically modified. At the one-loop level, we have (see for example [86])

$$\alpha_2^{-1}(Q) = \alpha_2^{-1}(M_{\text{MDM}}) - \frac{b_2}{2\pi} \ln \frac{Q}{M_{\text{MDM}}}, \tag{2.2}$$

$$b_2 \equiv -\frac{19}{6} + c \, \frac{n^3 - n}{18}, \tag{2.3}$$

Quntum numbers			DM	Not excluded by	Examples
$SU(2)_L$	$U(1)_Y$	Spin	stability	direct detection	
2	1/2	Scalar			
2	1/2	Fermion			Higgsino
3	0	Scalar		✓	[87]
3	0	Fermion		✓	Wino
3	1	Scalar/Fermion			[87]
4	1/2	Scalar/Fermion			[87]
4	3/2	Scalar/Fermion			[87]
5	0	Scalar		✓	[87]
5	0	Fermion	✓	✓	[83–85]
5	1	Scalar			
5	1	Fermion	✓		
5	2	Scalar			
5	2	Fermion	✓		
6	1/2, 3/2, 5/2	Scalar	✓		
7	0	Scalar	✓	✓	[83–85]
7	1, 2, 3	Scalar	✓		

Table 4:   Table of the MDM properties. In the first three columns, we show the quantum numbers of our choice. In the next two columns, DM stability (the checkmark means "stable") and its status under the DM direct detection experiment (the checkmark means it is still alive) are shown. The last column is devoted to the examples in the literature.

with $c = 1$ (1/4) for a Majorana/Weyl fermion (real scalar). Note that the first and second term of Eq. (2.3) represent the contributions from SM particles and the MDM, respectively. Then, assuming the perturbativity of the $SU(2)_L$ gauge coupling up to $M_{\rm pl}$, this relationship puts an upper bound on the choice of n. According to the strong dependence on n of b_2, a strong bound is obtained,

$$n \leq \begin{cases} 8 & \text{real scalar MDM,} \\ 5 & \text{Majorana fermion MDM.} \end{cases} \tag{2.4}$$

In Table 4, we summarize the properties of MDMs for several different choices of (n, Y). Throughout the table, the checkmark represents a suitable property as a DM candidate.

In the first three columns, we show the quantum numbers of our choice, namely the set of (n, y) and spin. In the next column, we show the condition for the DM stability, namely, whether all the DM decay operators have dimensions larger than five or not. The checkmarks correspond to the automatically stable DM candidates. The next column shows if the DM direct detection experiment has already excluded these DM candidates or not. Since the non-zero value of Y usually leads to the large cross section as will be discussed in Sec. 3.2, only $Y = 0$ candidates are associated with checkmarks.   (♣ **Correct?** ♣) However, note that these properties may be changed due to a small modification to the model, such as the imposition of an extra symmetry or the mixing between other new physics particles. The final column shows examples of the viable DM candidates analyzed in the literature.

From the table, we can see that there are two fascinating targets, a 5-plet fermion and a 7-plet scalar both of which have $Y = 0$. Among them, we neglect the latter possibility because it has been pointed out [88,89] that a dimension five operator combined with a loop consisted of the TeV scale 7-plet scalar induces a sizable decay rate for the $U(1)_{\rm EM}$ neutral component. Instead, we will take a 5-plet scalar with $Y = 0$ just as a working example, assuming that its stability is ensured by some other mechanism.

2.3   Mass splitting among an $SU(2)_L$ multiplet

As a final remark in this section, we consider an important property of $SU(2)_L$ multiplets after the spontaneous breakdown of the electroweak symmetry: the mass splitting among the components of a multiplet. This mass splitting, which we will call Δm_χ, is typically much smaller compared with the WIMP mass m_χ, but its value is phenomenologically important as we will see in later sections.

First, we start with the tree-level propagation of heavy particles, such as the SUSY particles other than the LSP, or other unknown particles. After integrating out all the heavy particles other than the SM particles or the light WIMP, we may obtain operators of the form of $\mathcal{O} = M_{ij}\chi_i\chi_j$, where χ denotes the WIMP and i is the $SU(2)_L$ index. This operator causes the mass splitting only when M_{ij} transforms non-trivially under the $SU(2)_L$ symmetry. Then, we can explicitly construct the lowest dimensional operator among those relevant for the mass splitting. For Higgsino,

$$\mathcal{O} = \frac{1}{\Lambda}(\bar{\chi}H^*)(H\chi), \tag{2.1}$$

where $\chi = (\tilde{H}_u, -i\sigma_2\tilde{H}_d^*)^t$, Φ is the SM Higgs doublet with $Y = 1/2$, Λ is the cut-off scale of the effective theory, *i.e.*, the typical mass scale of the relevant heavy particles, and the parenthesis denotes the $SU(2)_L$ invariant product of fundamental representations. Similarly,

for Wino, [90]

$$\mathcal{O} = \frac{1}{\Lambda^3}(H^\dagger \sigma^a H)(H^\dagger \sigma^b H)\tilde{W}^a \tilde{W}^b, \tag{2.2}$$

is the lowest dimensional operator that causes the mass splitting. A simple implication of this observation is that, for multiplets with large n, there are suppression factors that keep the tree-level mass splitting small. For Wino, the suppression is of $\mathcal{O}(M_W^4/\Lambda^3)$, which yields a splitting smaller than $10\,\mathrm{MeV}$ for heavy particles with a few TeV masses. For fermionic MDMs with $n \gtrsim 5$, a similarly small mass splitting at the tree-level is expected.[47] This is the main reason why the loop correction plays a more important role in the mass splitting of Wino and MDMs.

The situation is different for Higgsino because of the much less drastic suppression factor of $\mathcal{O}(M_W^2/\Lambda)$, which generates $\mathcal{O}(100)\,\mathrm{MeV}$ mass splitting for $\Lambda \lesssim 10\,\mathrm{TeV}$.[48] In fact, in models like the split SUSY, the mixing between Higgsino and heavier gauginos can generate the large mass splitting among the Higgsino components. As a result, neutral components that originally forms a Dirac fermion splits into two Majorana fermions with mass difference Δm_0, and the charged components also become heavier than the lighter neutral component by $\Delta m_+^{(\mathrm{tree})}$. According to [91], their approximate expressions are given by

$$\Delta m_0 \simeq \frac{M_W^2}{g_2^2}\left(\frac{g_1^2}{M_1} + \frac{g_2^2}{M_2}\right), \tag{2.3}$$

$$\Delta m_+^{(\mathrm{tree})} \simeq \frac{M_W^2}{2g_2^2}\left[\left(\frac{g_1^2}{M_1} + \frac{g_2^2}{M_2}\right) + \mathrm{sgn}(\mu)\sin 2\beta\left(\frac{g_1^2}{M_1} - \frac{g_2^2}{M_2}\right)\right], \tag{2.4}$$

assuming the CP invariance for simplicity. Note that the results agree with the previous order estimation with $\Lambda \sim M_1$, M_2.

Next, we consider the loop correction to the WIMP masses. When the loop is composed of heavy particles, the effective operator that causes the mass splitting again becomes the same as above, which is now associated with a small loop factor. Thus, the largest contribution comes from the gauge boson – WIMP loop. For the charged components of Higgsino, the one-loop result is known: [91]

$$\Delta m_+^{(\mathrm{rad})} \simeq \frac{1}{2}\alpha_2 M_Z \sin^2\theta_W\left(1 - \frac{3M_Z}{2\pi m_\chi}\right) \sim 355\,\mathrm{MeV}\left(1 - \frac{3M_Z}{2\pi m_\chi}\right), \tag{2.5}$$

---

[47]For scalar MDMs, there is another renormalizable operator that generates a mass splitting

$$\mathcal{O} = -\lambda_H\left(\chi^* \sigma^a \chi\right)\left(H^\dagger \sigma^a H\right).$$

Here, we just assume that λ_H is sufficiently small and the discussion below is not affected by the above term.

[48]For the order estimation of the mass splitting, we have taken account of the size of the coupling constants omitted in Eq. (2.1), using the rough estimation $g_1^2 \sim g_2^2 \sim \mathcal{O}(10^{-1})$.

WIMP DM candidate	Quantum numbers			Masses	
	$SU(2)_L$	$U(1)_Y$	Spin	m_χ/TeV	Δm_χ/MeV
Higgsino	2	1/2	Dirac fermion	1.1	341
Wino	3	0	Majorana fermion	2.9	166
5-plet scalar	5	0	real scalar	9.4	166
5-plet fermion	5	0	Majorana fermion	10	166

Table 5:   Table of properties of WIMPs discussed in this thesis. In the "Quantum numbers" block, the $SU(2)_L$ and $U(1)_Y$ charges and spin nature are shown. In the "Masses" block, the proper mass of the thermally produced DM m_χ and mass difference between the neutral and charged components of the multiplet Δm_χ are shown. See Sec. 3.1 for the descriptions and implications of m_χ and Sec. 2.3 for those of Δm_χ.

with θ_W being the Weinberg angle, which gives $\Delta m_+^{\text{(rad)}} \simeq 341\,\text{MeV}$ for $m_\chi = 1.1\,\text{TeV}$ and may be comparable to $\Delta m_+^{\text{(tree)}}$. On the other hand, for Wino, we have the two-loop result [92]

$$\frac{\Delta m}{\text{MeV}} = -413.315 + 305.383 \left(\log \frac{m_\chi}{\text{GeV}} \right) - 60.8831 \left(\log \frac{m_\chi}{\text{GeV}} \right)^2 \tag{2.6}$$

$$+ 5.41948 \left(\log \frac{m_\chi}{\text{GeV}} \right)^3 - 0.181509 \left(\log \frac{m_\chi}{\text{GeV}} \right)^4, \tag{2.7}$$

which exhibits $\Delta m \simeq 165\,\text{MeV}$ for $m_\chi = 2.9\,\text{TeV}$. For the MDM, there are neutral, singly charged, doubly charged, and so on, components. Among them, the neutral and singly charged components have the smallest mass difference of $\Delta m \simeq 166\,\text{MeV}$ [83], which is the most important value for the phenomenology.

2.4   Summary

In Table 5, we summarize the properties of WIMPs discussed in this thesis. In the first block named "Quantum numbers", we show the $SU(2)_L$ electroweak charge, $U(1)_Y$ hypercharge, and spin nature. In the second block named "Masses", two types of masses are shown. m_χ is the required masses to explain the DM relic abundance without non-thermal production (see Sec. 3.1 for the detail). Δm_χ is the mass difference between the electromagnetically neutral and (singly) charged components of the multiplet discussed in the previous section. Values are taken from [84, 87, 93–96].

Section 3

WIMP as a dark matter

In this section, we review the properties of WIMPs as DM candidates. It is revealed that, when we take a close look at the relic abundance of WIMP DM in Sec. 3.1, a WIMP with the TeV scale mass is a good DM candidate, which is sometimes called *WIMP miracle* and is a strong motivation to consider WIMPs. In Sec. 3.2 and 3.3, we will consider two different ways to search for WIMP DM, called the direct and indirect detection. Finally, Sec. 3.4 is devoted to the summary and concluding remarks of this section.

3.1　WIMP DM relic abundance

One of the most important evidence of the beyond SM phenomena is the existence of DM [97]. DM is an unknown object that occupies a large fraction of the total energy of our universe but has not yet been directly observed because of its weak interaction with the SM particles.[♮9] In spite of its invisibility, the existence of DM is confirmed by several astrophysical observations such as the mass measurement using the gravitational lensing effect caused by galaxies and clusters [98, 99], the flatness of galactic rotation curves further the optical radius [100, 101], the measurement of the power spectrum of the cosmic microwave background (CMB), and so on. In particular, the observation of CMB allows us the precise determination of various cosmological parameters [102, 103] including the normalized density of the non-relativistic matter Ω_m and that of baryon Ω_b, which is currently determined as [104]

$$\Omega_m h^2 = 0.1430 \pm 0.0011, \tag{3.1}$$

$$\Omega_b h^2 = 0.02237 \pm 0.00015, \tag{3.2}$$

where $h \sim \mathcal{O}(1)$ is the Hubble constant in units of $100\,\mathrm{km\,s^{-1}\,Mpc^{-1}}$. The difference between $\Omega_m h^2$ and $\Omega_b h^2$ implies the existence of DM and its abundance $\Omega_\chi h^2 \simeq 0.12$.

In cosmology, DM production mechanisms that explain the DM abundance are divided into two large categories: thermal and non-thermal production. The former assumes the equilibrium between the DM and the thermal bath in the early universe. As the universe expands, the interaction rate that maintains the thermal equilibrium becomes smaller and the DM decouples from the thermal bath at some time, which is the so-called *freezeout*. As we will see below, the resulting abundance of the DM in this scenario is mainly controlled by the temperature of the thermal bath T_f when the freezeout occurs. On the other hand,

---

[♮9]At worst DM interacts with the SM particles through gravity, which is considerably weaker than all the other known interactions.

non-thermal production assumes the DM production by some processes irrespective of the thermal bath such as the decay of a heavy particle. From now on, we mainly focus on the case only with the thermal production, which gives the smallest possible relic abundance for WIMPs that have an interaction with the thermal bath through the electroweak interaction.

We assume the stable DM particle χ with mass m_χ that pair annihilates into SM particles with some cross section σ. When DM is in thermal equilibrium with the thermal bath of temperature T, DM velocity obeys the corresponding Boltzmann distribution. Let v be the relative velocity of annihilating DM particles and $\langle \sigma v \rangle$ be the thermal average of the product of σ and v. By using this quantity, we can write down the Boltzmann equation for the DM number density n_χ as

$$\frac{d(n_\chi a^3)}{dt} = -a^3 \langle \sigma v \rangle (n_\chi^2 - n_{\text{eq}}^2), \tag{3.3}$$

where t and a are the time coordinate and the scale factor, respectively, of the Friedmann Robertson Walker metric

$$ds^2 = -dt^2 + a(t)^2 d\boldsymbol{x}^2, \tag{3.4}$$

while n_{eq} denotes the number density of DM in equilibrium. When DMs are non-relativistic, its temperature dependence is given by $n_{\text{eq}} \propto T^{3/2} \exp(-m_\chi/T)$. The first term of the right-handed side of Eq. (3.3) represents the annihilation rate of DM pairs that should be proportional to n_χ^2, while the second term describes the DM creation through the inverse process. As desired, the number density does not change in time if $n_\chi = n_{\text{eq}}$. Recalling the total entropy conservation in a comoving volume $sa^3 = (\text{const})$, it turns out to be convenient to define the ratio $Y \equiv n_\chi/s$. In fact, this modification cancels the effect of the expansion of the universe $da/dt > 0$ from Eq. (3.3), leading to a simpler equation

$$\frac{dY}{dt} = -s \langle \sigma v \rangle (Y^2 - Y_{\text{eq}}^2), \tag{3.5}$$

with $Y_{\text{eq}} \equiv n_{\text{eq}}/s$.

Here, we assume that the freezeout occurs when the relativistic radiation dominates the total energy of the universe, which will be verified to be correct later. In this case, we can derive $a \propto T^{-1}$ from the entropy conservation with $s \propto T^3$. For the numerical calculation, we define a dimensionless parameter $x \equiv m_\chi/T$. Then Eq. (3.5) can be rewritten as

$$\frac{x}{Y_{\text{eq}}} \frac{dY}{dx} = -\frac{\Gamma}{H} \left(\frac{Y^2}{Y_{\text{eq}}^2} - 1 \right), \tag{3.6}$$

where Γ denotes the DM interaction rate defined as

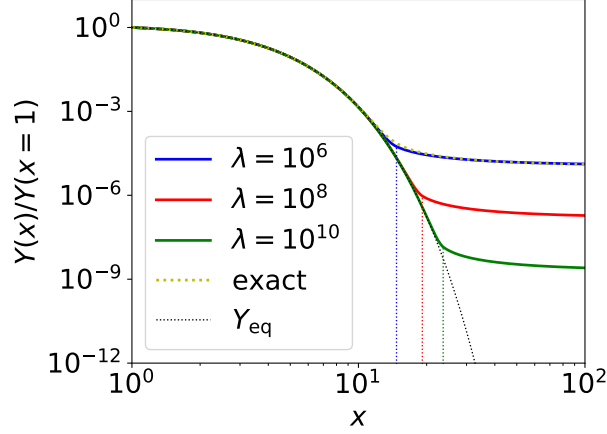$$\Gamma \equiv n_{\text{eq}} \langle \sigma v \rangle. \tag{3.7}$$

Figure 4:   Plot of $Y(x)/Y(x = 1)$ with $Y(x)$ being a solution of the evolution equation Eq. (3.6). The yellow dotted line is a solution for $\lambda \equiv \Gamma/H|_{x=1} = 10^6$, while the black dotted line denotes $Y_{\text{eq}}(x)/Y_{\text{eq}}(x = 1)$. The solid lines are the approximation to the solutions described in the text. The blue, red, and green colors correspond to $\lambda = 10^8$, 10^{10}, and 10^{12}, respectively. The vertical dotted lines denote the freezeout temperature x_f.

Finally, $\langle \sigma v \rangle$ is known to be expanded as [105]

$$\langle \sigma v \rangle = \langle \sigma v \rangle_s + \langle \sigma v \rangle_p \, x^{-1} + \cdots , \tag{3.8}$$

corresponding to the s-wave, p-wave, and so on, contributions to the cross section. When $x \gg 1$, which is the same as the non-relativistic limit, the term with the highest power of x dominates the cross section. When the x^{-p} term dominates ($p \geq 0$), the temperature dependence of the interaction rate is $\Gamma \propto x^{-3/2-p} e^{-x}$, while the Hubble parameter only reduces as $H \propto \rho^{1/2} \propto x^{-2}$. As a result, at some point Γ becomes smaller than H and Y freezes out as Eq. (3.6) indicates. Hereafter, we focus on the case of the s-wave domination with $\langle \sigma v \rangle_s \neq 0$ for simplicity.   (♣ **Also comment on p-wave** ♣) In Fig. 4, we show the solution of Eq. (3.6) for $\lambda \equiv \Gamma/H|_{x=1} = 10^6$ by the yellow dotted line. In the calculation, we use the boundary condition $Y(x = 1) = Y_{\text{eq}}(x = 1)$ and plot the normalized value $Y(x)/Y(x = 1)$. We also plot the function $Y_{\text{eq}}(x)/Y_{\text{eq}}(x = 1)$ by the black dotted line.

Unfortunately, it is computationally hard to solve Eq. (3.6) for larger values of λ because of the almost complete cancellation between two terms of the right-handed side for small $x \sim \mathcal{O}(1)$ and its amplification caused by large λ. We adopt instead to use an approximation that is the same as the one adopted in the public code `MicrOMEGAs` [106, 107]. For the small x region, temperature is still high enough to maintain the equilibrium $Y \simeq Y_{\text{eq}}$, which means that $d\Delta Y/dx \ll dY_{\text{eq}}/dx$ with $\Delta Y \equiv Y - Y_{\text{eq}}$. From this approximation, we obtain a formula

$$\Delta Y \simeq -\frac{x}{2\lambda} \frac{dY_{\text{eq}}}{dx}. \tag{3.9}$$

Then we define the time x_f, or equivalently the so-called freezeout temperature T_f, when the approximation becomes invalid through the equation[10]

$$\Delta Y(x_f) = 2.5 Y_{\mathrm{eq}}(x_f). \tag{3.10}$$

After the freezeout $x > x_f$, the annihilation of the DM pairs rapidly slows down and the DM abundance far exceeds its equilibrium value: $Y \gg Y_{\mathrm{eq}}$. Then we can neglect the second term of the right-handed side of Eq. (3.6) and obtain the analytical solution

$$Y(x) \simeq -\frac{x}{c_1 x + \lambda/Y_{\mathrm{eq}}(x=1)}, \tag{3.11}$$

where c_1 is an integration constant. In Fig. 4, we show results obtained with these two approximations Eqs. (3.9) and (3.11) for $\lambda = 10^6$ (blue), 10^8 (red), and 10^{10} (green). In particular, the blue and the yellow lines almost completely overlap with each other, which proves the validity of the approximations. The vertical dotted lines in the figure show the freezeout temperature. It can be seen from the figure that $x = x_f$ does correspond to the time when Y starts to deviate from Y_{eq}. Note also that as $\lambda \propto \langle \sigma v \rangle$ becomes larger, the freezeout time becomes later and the resulting relic abundance becomes smaller.

When the DM properties (*i.e.*, the mass m_χ and the annihilation cross section $\langle \sigma v \rangle$ for a given temperature T) are given, corresponding relic abundance can be calculated using above procedure. In particular, m_χ determines the normalization of the figure, namely $Y_{\mathrm{eq}}(x=1) = Y_{\mathrm{eq}}(T=m_\chi)$, and $\langle \sigma v \rangle$ determines the freezeout temperature through the combination of Eq. (3.7). Assuming the absence of a non-thermal production, there should be a unique choice of m_χ corresponding to some $\langle \sigma v \rangle$ to explain the current relic abundance of the DM. From the numerical calculation, we obtain an order estimation formula

$$\Omega_\chi h^2 \sim \frac{3 \times 10^{-27}\,\mathrm{cm^3/s}}{\langle \sigma v \rangle_0} \sim 0.1 \left(\frac{0.01}{\alpha} \right)^2 \left(\frac{m_\chi}{300\,\mathrm{GeV}} \right)^2, \tag{3.12}$$

where the rough estimation $\langle \sigma v \rangle \sim \alpha^2/m_\chi^2$ is used in the last equation with α being the fine structure constant for the DM-SM coupling. What is fascinating in Eq. (3.12) is that a particle can be DM if it has a mass comparable to the electroweak scale and coupling constant comparable to the electroweak coupling constant. This is the so-called *WIMP miracle*, which supports the hypothesis of the WIMP as a candidate of the DM. Such TeV-scale WIMPs are theoretically well-motivated in connection with problems of the SM such as the naturalness problem as reviewed in Sec. 2. Also, phenomenologically such TeV-scale WIMPs are of great interest, since they can be detected using several different methods as will be described in this thesis.

---

[10]One can easily check that the final relic abundance is not sensitive to the choice of the numerical coefficient 2.5 in Eq. (3.10).

In Table 5, we summarize the value of m_χ for each WIMP model that predicts the correct relic abundance $\Omega_\chi h^2 \sim 0.12$. As described above, TeV scale masses are suitable for all WIMP DMs and the required mass becomes larger when we consider a larger $SU(2)_L$ n-plet because of the larger annihilation cross section. However, note that the precise estimation of the relic abundance solely using the last term of Eq. (3.12) is not possible, because of the so-called Sommerfeld enhancement effect [94, 108] that significantly modifies the annihilation cross section. We will review this effect in more detail in Sec. 3.3 in relation to the indirect detection experiments. Note also that m_χ in the table is only an upper bound on the WIMP DM mass because the existence of non-thermal production processes may allow lighter WIMPs to explain the whole relic abundance of DM in the current universe.

3.2   WIMP DM search : direct detection

There are many experiments aimed at the direct detection of the DM[♮11] proposed in [110]. Here, we assume some interaction between the DM and SM particles and look for the recoil of a target SM particle due to the collision with the DM in the laboratory. In the case of WIMPs of our concern, any particle with non-zero electroweak charge can be a target particle, which interacts with WIMPs through the t-channel electroweak gauge boson exchange. In the traditional setup such as the XENON1T experiment [111], a nucleus (of xenon in XENON1T) and an electron are the frequently used target particles. From now on, we focus on the nucleus target since, as will be turned out later, it gives much better sensitivity than the electron target for DMs with a mass of $\mathcal{O}(\text{TeV})$. In this case, there are several ways to read out the information of the nuclear recoil depending on the deposited energy, such as the use of heat (or photons), an excitation of the nucleus associated with the emission of scintillation light, and the ionization of the atom. Among them, the XENON1T experiment uses the scintillation light.

To evaluate the event rate for this kind of experiment, it is important to know the DM energy density ρ_0 and velocity distribution around us. For this purpose, we model the DM profile in our galaxy using the so-called standard halo model (SHM) and adjust the parameters to the observations. In the SHM, we assume the DM velocity distribution in the galactic rest frame

$$f(\boldsymbol{v}) = \frac{1}{\sqrt{2\pi}\sigma} \exp\left[-\frac{\boldsymbol{v}^2}{2\sigma^2}\right], \tag{3.1}$$

with $\sigma \equiv \sqrt{3/2}v_c$, where v_c denotes the local circular speed of DMs around the galactic center. From the combination of different analyses, we obtain the values $\rho_0 = 0.3\,\text{GeV}/\text{cm}^3$ and $v_c = 220\,\text{km/s}$ [112, 113]. Also, the DM velocity within the halo cannot be arbitrarily

---

[♮11]For a recent review of the direct detection experiments, see for example [109].

large, since such energetic DM will not be gravitationally bound and will escape from our galaxy. We often introduce a cutoff velocity $v_{\mathrm{esc}} = 544\,\mathrm{km/s}$ [114] and simply assume $f(\boldsymbol{v}) = 0$ for $|\boldsymbol{v}| > v_{\mathrm{esc}}$.

Using the distribution defined above, the differential event rate per unit recoil energy E per unit material mass is given by [115]

$$\frac{dR}{dE}(E,t) = \frac{\rho_0}{m_\chi m_T} \int d^3v \, v f(\boldsymbol{v},t) \frac{d\sigma}{dE}(E,v), \tag{3.2}$$

where m_T is the mass of the target nucleus, while $d\sigma/dE$ is the differential cross section of the DM-nucleus scattering. The DM velocity distribution $f(\boldsymbol{v},t)$ is now time-dependent since it represents the distribution observed at the laboratory, which is affected by the motion of the Earth around the Sun and that of the Sun around the galactic center. Thus, $f(\boldsymbol{v},t)$ is derived by performing the Galilean transformation to $f(\boldsymbol{v})$ according to the time-dependent velocity of the Earth against the galactic rest frame. This time-dependence gives the signal a characteristic daily and yearly modulation, which helps us to distinguish it from the background events. Also, the Galilean transformation makes $f(\boldsymbol{v},t)$ highly anisotropic since the velocity of the Earth is comparable to v_c. Thus, if it is possible to use the directional information, it also helps us to reduce the background.

The differential cross section $d\sigma/dE$, which summarizes the particle physics part of the calculation, is divided into two parts: the spin-independent (SI) part and the spin-dependent (SD) part. Denoting the SI and SD scattering cross sections for zero momentum transfer as σ_0^{SI} and σ_0^{SD}, respectively, we obtain

$$\frac{d\sigma}{dE}(E,v) = \frac{m_T}{2\mu_T^2 v^2} \left(\sigma_0^{\mathrm{SI}} F_{\mathrm{SI}}^2(E) + \sigma_0^{\mathrm{SD}} F_{\mathrm{SD}}^2(E) \right), \tag{3.3}$$

with μ_T being the reduced mass of the WIMP-nucleus system. The form factors F_{SI} and F_{SD} summarize the nuclear physics part of the matrix element, both of which have properties $F(0) = 1$ and $dF/dE < 0$ for large E. Among SI and SD contributions, the SI part is of great interest thanks to the possible coherent enhancement of the cross section. When the de Broglie wavelength corresponding to the momentum transfer q is longer than the size of the nucleus (corresponding to $q \lesssim 200\,\mathrm{MeV}$ for the xenon), not the individual neutrons and protons but the whole nucleus contribute to the cross section.[♮12] This results in the coherent contribution from all nucleons for the SI case, while only the unpaired nucleons contribute to the cross section for the SD case. In fact, for the WIMP DM, the SI cross section σ_0^{SI} is originally non-zero and enhanced thanks to the coherence by a large factor A that is the

---

[♮12]When the DM is lighter and the de Broglie wavelength is even longer, the collective excitation modes of nuclei or electrons such as the phonon becomes important.   (♣ **Reference** ♣) This corresponds to $q \lesssim \mathcal{O}(1)\,\mathrm{keV}$ or $m_\chi \lesssim \mathcal{O}(1)\,\mathrm{MeV}$ and thus we neglect this possibility here.
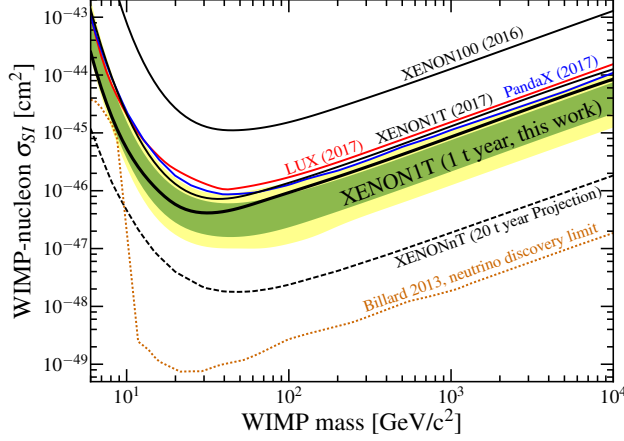
Figure 5:   Current constraint on the DM SI cross section taken from [17]. The y-axis corresponds to σ_p^{SI} in our notation.

mass number of the target nucleus ($A \simeq 130$ for the xenon) as

$$\sigma_0^{\text{SI}} = A^2 \sigma_p^{\text{SI}} \frac{\mu_T^2}{\mu_p^2} \tag{3.4}$$

where σ_p^{SI} is the SI scattering cross section for a DM and a single nucleon and μ_p is the reduced mass of the WIMP-nucleon system. The above expression dominates over the SD cross contribution for the WIMP DM.

In Fig. 5, we show the most recent constraint on the DM SI scattering cross section σ_p^{SI} as a function of its mass taken from [17] by the XENON1T collaboration. The previous results of the LUX [15] and the PandaX-II [16] experiments are also shown. In the figure, the green and yellow bands represent the upper bound on the cross section with 1σ and 2σ experimental uncertainties, respectively. Black dotted line corresponds to the prospect for the future experiment called XENONnT, while the orange dotted line represents the cross section of the background events sourced by neutrinos [116]. This background often called as the neutrino floor, which is mainly determined by the solar neutrino for the region $m_\chi \lesssim 10\,\text{GeV}$ and by the atmospheric and supernova neutrinos for $m_\chi \gtrsim 10\,\text{GeV}$, roughly represents the maximum possible sensitivity of the direct detection method.[♮13]

The qualitative description of the form of the sensitivity curve in Fig. 5 can be given using the above discussion. The sensitivity for a very light WIMP is weak because of the finite threshold E_{thr} of the recoil energy required for the detection of the signal. The threshold effect can be taken into account by choosing the lower boundary of the $\boldsymbol{v}$-integral in Eq. (3.2)

[♮13]It may be possible, in particular for the solar neutrino background, to significantly reduce the number of background events and go beyond the neutrino floor by using the directional information of the signals.

to be v_{min} defined as

$$v_{\mathrm{min}} = \sqrt{\frac{m_T E_{\mathrm{thr}}}{2\mu_T^2}}. \tag{3.5}$$

Since $v_{\mathrm{min}} \propto m_\chi^{-1}$ for $m_\chi \ll m_T$, the event rate rapidly becomes smaller for smaller m_χ. On the other hand, heavier WIMPs have less number density with the energy density ρ_0 fixed. Because of this, the sensitivity for a heavy WIMP becomes moderately worse when m_χ increases. These two behaviors determine the best suitable m_χ for each choice of m_T and E_{thr}, which is the reason why the xenon nucleus target is more suitable for the TeV-scale WIMP search than the electron target. The latter choice is suitable when we search for lighter DMs.

Although no signal of DM is observed yet, this null result is still consistent with WIMP models of our concern. For example, the calculation up to the next-to-leading order in α_s for the Wino DM reveals that the cross section almost mass-independently takes a small value of $\sigma_p^{\mathrm{SI}} \simeq 2.3 \times 10^{-47}\,\mathrm{cm}^2$ [20], which is below the current constraint but is a region of future interest. As for the MDM, the 5-plet fermion is analyzed in [23] and the scattering cross section $\sigma_p^{\mathrm{SI}} \simeq 10^{-46}\,\mathrm{cm}^2$ is obtained. However, the mass requirement $m_\chi \sim 10\,\mathrm{TeV}$ (see Table 5) makes the detection difficult and the sensitivity will not cover the whole region of the viable parameter space. For Higgsino-like LSP, the constraint is highly model-dependent since the mixing between the Higgsino and Bino or Wino significantly modifies the scattering cross section. According to [19, 117], the pure Higgsino has σ_p^{SI} below the neutrino floor, while some of the parameter space with a sizable mixing has much larger σ_p^{SI} that is already excluded. Thus, we conclude that the almost pure Higgsino-like state is difficult to search for using this method.

(♣ **Check constraints for $Y \neq 0$ MDM** ♣)

3.3   WIMP DM search : indirect detection

The indirect detection of DM[♮14] uses the DM annihilation process into SM particles to detect the DM signal. When DM is composed of WIMPs, their annihilation can be again explained by the electroweak interaction. Since DMs are non-relativistic in the current universe, the s-wave contribution to the annihilation cross section is strongly favored, which results in the dominant annihilation process coming from the t- and u-channel exchange of virtual WIMP. (♣ **Same for scalar?** ♣) Then, some of the final state particles may fly to the earth and be observed by telescopes in the form of gamma-rays, neutrinos, cosmic-rays, and so on.

The DM annihilation rate at some point $\boldsymbol{x}$ of the universe has a quadratic dependence

---

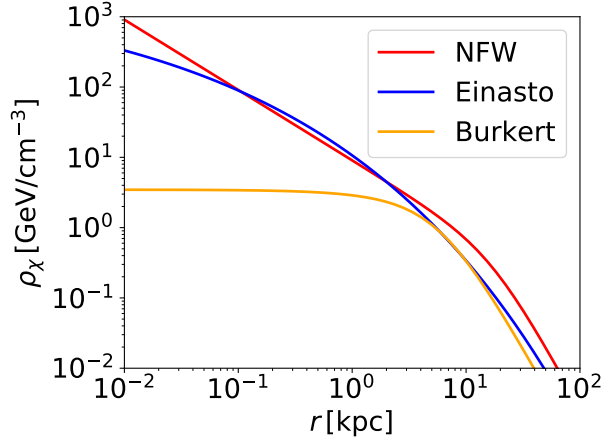[♮14]For a recent review of the indirect detection experiments, see for example [118].

Figure 6:   Dark matter energy density ρ_χ within our galaxy as a function of the distance from the galactic center r.

on the DM energy density $\rho_\chi(\boldsymbol{x})$.[♮15] Thus, the main targets of indirect detection experiments are center of galaxies or galaxy clusters, where abundant DM is expected to be accumulated thanks to the strong gravitational potential. The DM energy density distribution around each galaxy (cluster) can be determined by the observation of the rotation curve of luminous objects. One of the model functions introduced to fit such observations is the so-called the Navarro-Frenk-White (NFW) profile [119, 120] of the DM density distribution,

$$\rho_{\text{NFW}}(r) = \frac{\rho_s}{\left(\frac{r}{r_s}\right)\left[1 + \left(\frac{r}{r_s}\right)\right]^2}, \tag{3.1}$$

where r is the distance from the center of the galaxy of our concern. Free parameters ρ_s and r_s should be chosen to fit data for each galaxy, which gives for our galaxy $\rho_s \sim 1 \times 10^7 M_\odot\,\text{kpc}^{-3}$ and $r_s \sim 20\,\text{kpc}$ [121] with $M_\odot$ being the solar mass.

The inner slope of the NFW profile follows $\rho_{\text{NFW}} \propto r^{-1}$. On the other hand, many observations of the rotation curve and models of dwarf galaxies suggest the scaling behavior $\rho \propto r^0$, which is the so-called core-cusp problem (see [122] and references therein). To take account of this behavior, other profiles are also widely used: the Einasto profile [123, 124]

$$\rho_{\text{Einasto}}(r) = \rho_s \exp\left[-\frac{2}{\alpha}\left\{\left(\frac{r}{r_s}\right)^\alpha - 1\right\}\right], \tag{3.2}$$

with $\rho_s \sim 5 \times 10^6 M_\odot\,\text{kpc}^{-3}$, $\alpha \sim 0.2$, and $r_s \sim 10\,\text{kpc}$ for our galaxy, and the Burkert

---

[♮15]More precisely, the annihilation rate has a quadratic dependence on the DM number density $n_\chi(\boldsymbol{x})$. This means that, for some fixed value of $\rho_\chi(\boldsymbol{x})$, the lighter DM has more chance to annihilate since $n_\chi = \rho_\chi/m_\chi$.

Target	$\log_{10}(J(\hat{\boldsymbol{n}}, \Delta\Omega)/\mathrm{GeV}^2\mathrm{cm}^{-5})$
Galactic Center	21.5
Dwarf Galaxies	16–19
Galaxy clusters	~ 20

Table 6: Comparison of J-factors for several targets of DM indirect detection.

profile [125]

$$\rho_{\mathrm{Burkert}}(r) = \frac{\rho_s}{\left(1 + \frac{r}{r_s}\right)\left(1 + \frac{r^2}{r_s^2}\right)}, \tag{3.3}$$

with $\rho_s \sim 9 \times 10^7 M_\odot\,\mathrm{kpc}^{-3}$ and $r_s \sim 6\,\mathrm{kpc}$ for our galaxy. In Fig. 6, we show the DM energy density distribution in our galaxy.[16] As for the choice of parameters, we use the mean values of fits of several observations listed in [121] and shown above. We can see the difference of shapes among three profiles at the small r region.

The event rate at the laboratory can be divided into the particle physics part and the astrophyical part, the second of which, referred to as the J-factor, is related to the DM density distribution. The J-factor for the DM annihilation for a sky patch with solid angle $\Delta\Omega$ around a sky direction $\hat{\boldsymbol{n}}$ is given by

$$J(\hat{\boldsymbol{n}}, \Delta\Omega) = \int_{\Omega \sim \hat{\boldsymbol{n}}} d\Omega \int_{\mathrm{LOS}} \rho_\chi^2(\Omega, \ell) d\ell, \tag{3.4}$$

where ℓ is a distance along the line-of-sight (LOS) defined by the direction Ω. The first integration performed over a region $\Delta\Omega$ around the direction $\hat{\boldsymbol{n}}$, while the second one sums up all the contributions from DMs on the LOS. Using this, the flux $\Phi_x(E, \hat{\boldsymbol{n}}, \Delta\Omega)$ of a SM particle x with energy E at the sky patch is expressed as[17]

$$\Phi_x(E, \hat{\boldsymbol{n}}, \Delta\Omega) = \frac{\langle \sigma v \rangle}{8\pi m_\chi^2} \frac{dN_x}{dE} J(\hat{\boldsymbol{n}}, \Delta\Omega), \tag{3.5}$$

where $\langle \sigma v \rangle$ and dN_x/dE are the thermally averaged DM annihilation cross section and the differential spectrum of x per annihilation, respectively.

In Table 6, we summarize J-factors for several astrophysical targets suitable for the indirect detection of DM. Values are taken from [121, 126, 127]. We show the result with $\hat{\boldsymbol{n}}$

---

[16]In principle, all the profiles should reconstruct the DM density at the Sun $\rho(r \sim 8\,\mathrm{kpc}) \sim 0.3\,\mathrm{GeV/cm}^3$, which is apparently not the case. This deviation can be explained to be the effect of the fitting error, which results in an order of magnitude uncertainty in ρ_χ at the 68 % level.

[17]We identify the DM particle and anti-particle in the calculation of Eq. (3.5). If it is not the case, the right-handed side should be multiplied by an extra factor of 1/2.
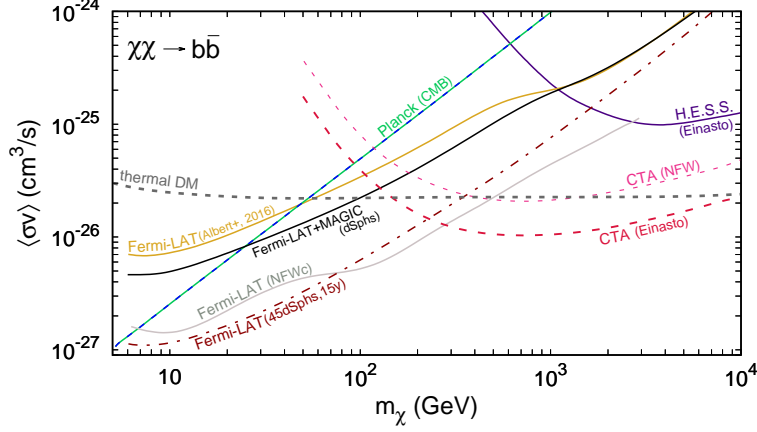
Figure 7: Constraints on the DM annihilation cross section from current and future planned indirect detection experiments. The figure is taken from [128].

and $\Delta\Omega$ being the direction of the target and the size of the target observed from the earth, respectively.[♮18] In the table, the results for the center of our galaxy, 20 dwarf galaxies in our galaxy, and 7 galaxy clusters are shown. Among the targets listed in the table, the Galactic Center seems to be the best source for the indirect detection, which is however suffered from huge background events at the same time. Dwarf galaxies may be more promising target since it provides much cleaner signals and the combined analysis of several targets can be performed to enlarge the statistics. Galaxy clusters may also be an interesting target since its power for the DM detection strongly depends on the DM profile of each galaxy cluster and a large enhancement may be expected for clusters that have relatively cusped DM profiles for some reason.

(♣ **Sommerfeld enhancement** ♣)

3.4   Summary

(♣ **To search for WIMPs that do not compose a sizable fraction of the DM, we have to rely on the collider search.** ♣)

[♮18]In [127], the authors use a different definition of the J-factor

$$J_T \equiv \frac{1}{4\pi D^2} \int dV \rho_\chi^2, \tag{3.6}$$

where D is the distance from the earth to the target, while the integral is performed over the whole volume of the target. This definition possesses an advantage especially for the assumption of the NFW profile, which becomes ill-defined around the origin in the integration process in Eq. (3.4). Due to this, it is difficult to convert the J-factor of their definition calculated with the NFW profile into that of our definition, and the result of the rough estimation is shown in the table.

Section 4

Direct collider search of WIMPs

In this section, we review the production of TeV-scale WIMPs and search for their signals using the collider experiment. In particular, we will summarize the current bounds for WIMPs obtained at the large hadron collider (LHC) and prospects at the future planned 100 TeV colliders such as the hadron option of the future circular collider (FCC-hh) [129] and the super proton-proton collider (SPPC) [44, 45]. In Sec. 4.1, we discuss the dominant production processes of WIMPs at a hadron collider. In Sec. 4.2 – 4.4, we review three different methods for the signal identification, the disappearing track, soft-lepton, and mono-jet search, and summarize the current and future bounds. (♣ **Correct?** ♣)

4.1   WIMP production

There are two relevant processes both of which significantly contribute to the production cross section of WIMPs considered here. The pair production via electroweak interaction is a universal process that can be considered for any particle with a non-zero electroweak charge. The decay of colored particles may also be efficient particularly for the MSSM. In this subsection, we will review these two in order.

Pair production via electroweak interaction

Since all the WIMPs of our interest possess non-zero $SU(2)_L$ and/or $U(1)_Y$ charges, they can be directly produced via electroweak interaction at the hadron collider as shown in
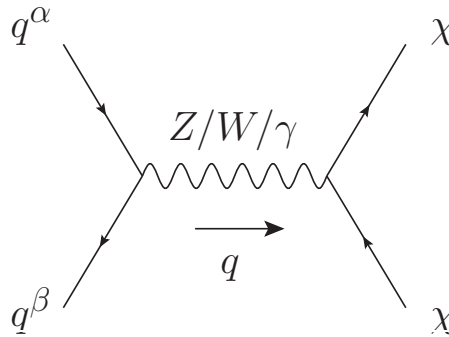

Figure 8: WIMP pair production process at the hadron collider.

Fig. 8.[♮19] In the figure, q^α and q^β denote the partons (namely, one of quarks)[♮20] of the incident protons relevant for the process, while χ denotes the WIMP and q is the momentum transfer. Assuming the WIMP to be a $SU(2)_L$ n-plet with $U(1)_Y$ charge Y and the mass m_χ, this process is well described by the effective lagrangian[♮21]

$$\mathcal{L} = \mathcal{L}_{\mathrm{SM}} + (D^\mu \chi)^\dagger (D_\mu \chi) - m_\chi^2 \chi^\dagger \chi \qquad \text{(complex scalar)}, \qquad (4.1)$$

$$\mathcal{L} = \mathcal{L}_{\mathrm{SM}} + \bar{\chi}(i\slashed{D} - m_\chi)\chi \qquad \text{(Dirac fermion)}, \qquad (4.2)$$

with $\mathcal{L}_{\mathrm{SM}}$ being the SM lagrangian, while the covariant derivative is given by

$$D_\mu \equiv \partial_\mu - ig_2 W^a T_n^a - ig_1 Y \slashed{B}, \qquad (4.3)$$

where T_n^a ($a = 1, 2, 3$) are n-dimensional representation matrices of $SU(2)_L$. Note that when χ is a real scalar (Majorana fermion) with $Y = 0$, the terms with χ in Eq. (4.1) (Eq. (4.2)) should be divided by two.

For the calculation, we neglect the effect of the electroweak symmetry breaking, which is valid because we are interested in the high-energy collision with the parton-level center-of-mass (CM) energy $\sqrt{s'} \equiv \sqrt{q^2} \gtrsim$ TeV. Then, we consider the process in the CM frame and estimate the parton-level differential cross section as

$$\left.\frac{d\sigma_{\alpha\beta}}{d\Omega}\right|_{\sqrt{s'},\mathrm{CM}} = \frac{C_{\alpha\beta}}{8s'}\left(1 - \frac{4m_\chi^2}{s'}\right)^{3/2}\sin^2\theta_{\mathrm{CM}} \qquad \text{(complex scalar)} \quad (4.4)$$

$$\left.\frac{d\sigma_{\alpha\beta}}{d\Omega}\right|_{\sqrt{s'},\mathrm{CM}} = \frac{C_{\alpha\beta}}{4s'}\sqrt{1 - \frac{4m_\chi^2}{s'}}\left[1 + \frac{4m_\chi^2}{s'} + \left(1 - \frac{4m_\chi^2}{s'}\right)\cos^2\theta_{\mathrm{CM}}\right] \quad \text{(Dirac fermion)}, \quad (4.5)$$

where θ_{CM} is the angle between the momentum of the initial parton q^α and that of a final state WIMP. These expressions are valid only when the center of mass energy exceeds the production threshold, $\sqrt{s'} > 2m_\chi$. Note also that these expressions represent inclusive cross sections, *i.e.*, the total cross section for the production of any component of the WIMP

[♮19]All the Feynman diagrams in this thesis are drawn with the public code `JaxoDraw-2.1` [130], which is a graphical user interface that allows users to draw Feynman diagrams intuitively and export them in the `eps` format with the help of the (modification of) `axodraw` style file for LaTeX [131]. Under the environment of macOS Mojave, it apparently fails to start, but one can still execute it by looking inside the application and start the Java executable file `jaxodraw-2.1-0.jar` directly. We would like to thank the authors for providing the best tools to write the thesis with.

[♮20]When we take account of the next-to-leading order QCD effect, gluon may also be one of the initial partons.

[♮21]In this subsection, we neglect the small mass splitting among different components in the multiplet χ described in Sec. 2.3. This approximation is valid since the mass splitting is by far smaller than m_χ and has only a tiny effect on the production process.

multiplet χ. The coefficient $C_{\alpha\beta}$ consists of contributions from $U(1)_Y$ and $SU(2)_L$ gauge bosons,[22]

$$C_{\alpha\beta} = c_{1\alpha\beta}Y^2\alpha_1^2 + c_{2\alpha\beta}I(n)\alpha_2^2, \tag{4.6}$$

with $I(n)$ being the Dynkin index for the n-dimensional representation given by

$$I(n) \equiv \frac{n^3 - n}{12}, \tag{4.7}$$

which is normalized so that $I(2) = 1/2$. The explicit form of $c_{1\alpha\beta}$ and $c_{2\alpha\beta}$, which are sizes of the couplings between partons of our choice and gauge bosons, can be expressed using the $U(1)_Y$ charge Y_α for the parton q^α and the reducible 13-dimensional representation matrices of $SU(2)_L$ in the parton basis $T_{\alpha\beta}^a$ as

$$c_{1\alpha\beta} = Y_\alpha^2 \delta_{\alpha\beta}, \tag{4.8}$$

$$c_{2\alpha\beta} = \sum_a \left| T_{\alpha\beta}^a \right|^2. \tag{4.9}$$

Recalling that $\alpha_1 < \alpha_2$ and that we often consider the WIMPs with large n and moderate Y, the WIMP production cross section grows as n^3 for larger multiplets according to the group theoretical factor (4.7).

In reality, the initial state of the hadron collider is not the individual partons but two protons. To obtain the cross section for the two-proton initial state, we rely on the parton distribution function (PDF), which expresses the fraction of the partons with some given momentum in each accelerated proton (see for example [132, 133]). Let $f_\alpha(x)$ $(0 < x < 1)$ be the PDF for a given parton q^α inside a proton with momentum p^μ. $f_\alpha(x)$ can be interpreted as a probability distribution to find the parton q^α with momentum xp^μ, so we have a relationship

$$\sum_\alpha \int_0^1 dx\, x f_\alpha(x) = 1, \tag{4.10}$$

associated with the total momentum conservation, and

$$\int_0^1 dx\, [f_d(x) - f_{\bar{d}}(x)] = 1, \tag{4.11}$$

$$\int_0^1 dx\, [f_u(x) - f_{\bar{u}}(x)] = 2, \tag{4.12}$$

---

[22]There is no contribution from the interference term between $U(1)_Y$ and $SU(2)_L$ contributions, since it is proportional to $\mathrm{Tr}(T_n^a) = 0$.
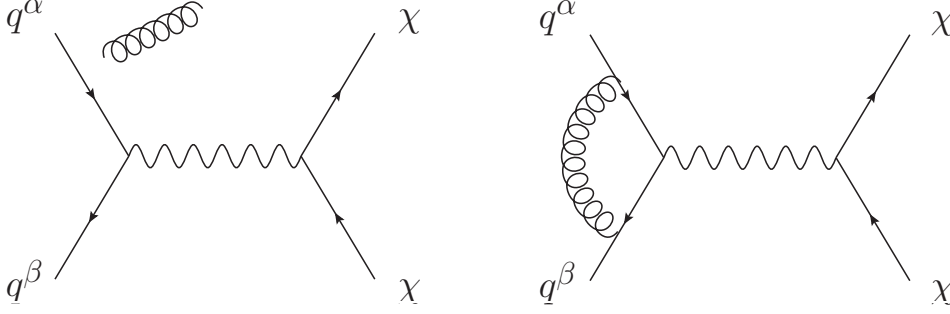
Figure 9: Example of NLO QCD contributions to the WIMP pair production process.

from the composition of the proton. Using the PDF, the cross section of the process of interest at the hadron collider is evaluated as

$$\frac{d\sigma}{d\sqrt{s'}d\Omega} = \sum_{\alpha,\beta} \int_0^1 dx_1 dx_2 \, f_\alpha(x_1) f_\beta(x_2) \delta\left(s' - s x_1 x_2\right) \left.\frac{d\sigma_{\alpha\beta}}{d\Omega}\right|_{\sqrt{s'},\mathrm{lab}}, \qquad (4.13)$$

where $\sqrt{s}$ is the CM energy of the proton-proton collision. Note that $d\sigma_{\alpha\beta}/d\Omega|_{\sqrt{s'},\mathrm{lab}}$ in the integrand is a function of x_1 and x_2, which is obtained by applying the appropriate Lorentz transformation to $d\sigma_{\alpha\beta}/d\Omega|_{\sqrt{s'},\mathrm{CM}}$. Precisely speaking, the PDF has an energy scale dependence which is determined by the Dokshitzer-Gribov-Lipatov-Altarelli-Parisi (DGLAP) equation [134–137]. Thus, the PDF is a function of the form $f(x, \mu_F)$, where μ_F is the analog of the renormalization scale for the PDF often called the factorization scale.

   Hadron colliders have several more features related to the strong interaction of quantum chromodynamics (QCD). Firstly, the next-to-leading order (NLO) QCD contribution to each process is not necessarily negligible. For the WIMP pair production, the real and virtual emission of a gluon shown in the left and right panels of Fig. 9, respectively, give the NLO QCD contributions, which will also be taken into account from now on. In particular, when the large transverse momentum is important for the phenomenology of our concern, such as the case in Sec. 4.2, the real emission of a gluon with sizable transverse momentum significantly modifies the cross section relevant for the analysis. Also, an additional real emission may be required to trigger the event, in particular when the other products are invisible for detectors like in Sec. 4.4. Secondly, all the colored particles in the initial, intermediate, and final states should be accompanied by numbers of soft emissions of gluons, which can be treated by the semi-classical approximation called the parton shower. In practice, there is a difficulty caused by the partial overlap of the gluon phase space between the one-gluon emission cross section calculated as an NLO QCD effect and the same calculated by the parton shower. To avoid the overlap, we often perform the matching procedure, in which we set some merging energy scale by hand and include the contribution to the cross section with gluon energy above (below) the scale only from the NLO QCD (parton shower) calculation.

WIMP name	Higgsino	Wino	5-plet Majorana fermion	5-plet real scalar
$\sigma_{\rm LO}$ [fb]	15	85	423	(♣ ??? ♣)
$\sigma_{\rm NLO}$ [fb]	17	93	461	(♣ ??? ♣)
K-factor	1.15	1.09	1.09	

Table 7: Table of pair production cross sections of several types of WIMPs. The CM energy $\sqrt{s} = 100\,{\rm TeV}$ is assumed and WIMP masses are set to be $1\,{\rm TeV}$.

Finally, the colored particles in the final states should eventually be confined, which is called the hadronization, and observed as some energetic and collimated sprays of hadrons, which as a whole is called a jet.

In the following, we perform the numerical calculation, taking account of all the above complexities. For this purpose, we make use of the Monte Carlo generator `MadGraph5 aMC@NLO (v2.6.3.2)` [138, 139] with the successive use of `Pythia8` [140] for the parton shower, hadronization, and matching and `Delphes (v3.4.1)` [141] for the detector simulation, including the definition of jets as observed objects. We use the MLM-style matching [142] with the merging scale of $67.5\,{\rm GeV}$ and `NNPDF2.3QED` with $\alpha_3(M_Z) = 0.118$ [143] as a canonical set of PDFs. For the renormalization and factorization scales, we adopt the default values of MadGraph5 aMC@NLO, *i.e.*, the central m_T^2 scale after k_T-clustering of the event. The one-loop level contributions such as the right panel of Fig. 9 can be taken into account by using a properly prepared model file and the `[QCD]` option of `MadGraph5`. However, just for simplicity of the analysis, we generate the tree-level pair production process with up to one jet.♮23

In Table 7, we list the production cross sections of various WIMPs via a weak gauge boson exchange at a $\sqrt{s} = 100\,{\rm TeV}$ hadron collider. As for the WIMP mass, we use the common value $m = 1\,{\rm TeV}$ to compare the cross sections among a different choice of quantum numbers. $\sigma_{\rm LO}$ and $\sigma_{\rm NLO}$ denote the production cross sections without and with the NLO QCD correction, respectively, while the last line is the so-called K-factor defined as $\sigma_{\rm NLO}/\sigma_{\rm LO}$. From the table, by comparing the results for the triplet (*i.e.* Wino) and 5-plet Majorana fermions, we can roughly see the correct dependence of the cross section on the $SU(2)_L$ charge $\sigma \propto n^3$.

In Table 8, we also show the mass dependence of the Wino pair production cross section. For heavier mass, a wider range of $\sqrt{s'}$ is below the production threshold $2m_\chi$ or accompanied with a small suppression factor $\left(1 - 4m_\chi^2/s'\right)^{1/2}$ as shown in Eq. (4.5), and the cross section becomes significantly smaller. However, values in the tables still denote that plenty of well-

---

♮23In spite of the lack of the one-loop contributions, this procedure is free from the infrared divergence since the matrix element with an additional jet is considered only when the jet energy scale is larger than the merging scale.

Wino mass [TeV]	1.0	1.5	2.0	2.9
$\sigma_{\rm LO}$ [fb]	85	19	6.1	1.3
$\sigma_{\rm NLO}$ [fb]	93	21	6.8	1.5
K-factor	1.09	1.11	1.11	1.15

Table 8:   Table of pair production cross sections of Wino with several choice of masses. The CM energy $\sqrt{s} = 100$ TeV is assumed.
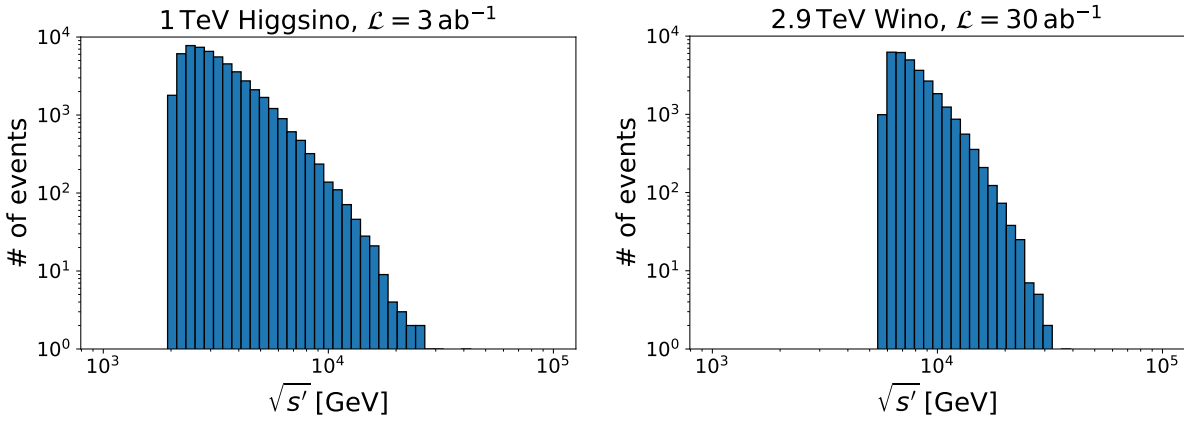

Figure 10:   Histogram of the $\sqrt{s'}$ distribution for $\sqrt{s} = 100$ TeV. *Left:* Production of 1 TeV Higgsino at $\mathcal{L} = 3\,{\rm ab}^{-1}$. *Right:* Production of 2.9 TeV Wino at $\mathcal{L} = 30\,{\rm ab}^{-1}$.

motivated WIMP DM candidates, such as 1 TeV Higgsino and 2.9 TeV Wino, are produced at, for example, the $30\,{\rm ab}^{-1}$ option of the FCC-hh.

In Fig. 10, we show the $\sqrt{s'}$ distribution for the pair production process at a $\sqrt{s} = 100$ TeV collider. Left and right figures correspond to the production of $m_\chi = 1$ TeV Higgsino at the integrated luminosity $\mathcal{L} = 3\,{\rm ab}^{-1}$ and of $m_\chi = 3$ TeV Wino at $\mathcal{L} = 30\,{\rm ab}^{-1}$, respectively. At around $\sqrt{s'} \sim 2m_\chi$, we clearly see the production threshold and the suppression effect $\sigma \propto (1 - 4m_\chi^2/s')^{1/2}$. On the other hand, when $\sqrt{s'}$ becomes much larger than $2m_\chi$, the cross section rapidly decreases because of both the scaling of the parton-level cross section $\sigma \propto (\sqrt{s'})^{-3}$ as in Eq. (4.5) and the smaller values of the PDF. Note that these properties are universal among several processes, including one of the contributions to the gluino pair production process through the s-channel gluon exchange discussed in the next subsection, and the lepton pair production via an electroweak gauge boson that is the main topics of Sec. 5.

(♣ **Histogram of angular dependence** ♣)

gluino mass [TeV]	6.0	7.0	8.0
$\sigma(pp \to \tilde{g}\tilde{g})$ [fb]	7.9	2.7	1.0

Table 9: Gluino pair production cross section at $\sqrt{s} = 100\,\text{TeV}$ taken from [144].

Decay of colored particles

In hadron colliders, a particle with the color charge have far more chance to be produced than a non-colored particle with the same mass. When we consider the split SUSY or the anomaly mediation model reviewed in Sec. 2.1, gluino tends to be relatively light, whose decay produces WIMPs. Without fine-tuning of Higgsino and gaugino masses, gluino lifetime is sufficiently short and only its decay products are observed by the detectors. Since all the SUSY particles finally decay into the LSP as described in Sec. 2.1, the gluino production cross section can effectively be counted as the production cross section of WIMPs in these models.

Keeping the R-parity conservation in our mind, the dominant process accompanied by gluinos in these models is the gluino pair production. In Table 9, we summarize the gluino pair production cross section for various gluino masses at $\sqrt{s} = 100\,\text{TeV}$, taken from [144]. The values in the table show that the gluino pair production process, depending on masses of gluino and WIMP, may give a much larger cross section for the WIMP production than the purely electroweak processes described above. We will mainly focus on, however, the electroweak pair production process below, in case gluino is out of the reach at 100 TeV colliders.

4.2   Disappearing track search

In the last section, we have checked the possibility that a large number of WIMPs are produced at hadron colliders. On the other hand, the detection of produced WIMPs is not a straight-forward task, because there are huge background events with many charged and/or colored particles. To reduce the background events and obtain the best possible reach for WIMPs, we consider several methods using typical properties for the WIMP signals, one of which is the disappearing track signal described here.

As mentioned in Sec. 2.3, the spontaneous breaking of the electroweak symmetry leads to the mass splitting among an $SU(2)_L$ multiplet, leaving the neutral component as the lightest one. As a result, the charged components of a multiplet, if produced, eventually decay into the neutral component. However, the mass splitting is so small in many cases that the typical flight length of the charged components is comparable to the detector size. Such long-lived charged particles, which travel for a few cm and then decay into an invisible counterpart, can be detected as charged tracks disappearing in the middle. They are very

characteristic signals and can be used as the most efficient discriminator between the SM background and the WIMP signals. In this section, we will study what we have summarized above in more detail.

Lifetime of charged components

The small mass splitting among a WIMP multiplet allows the heavier charged component to decay into the neutral component and SM particles via an off-shell W boson. Depending on the size of the relevant mass difference Δm, several channels contribute to the decay [145]. For tiny $\Delta m < m_\pi$ with m_π being the charged pion mass, $\chi^\pm \to \ell^\pm \nu_\ell \chi^0$ ($\ell = e, \mu$) are the unique decay modes. Once Δm exceeds m_π, the mode $\chi^\pm \to \pi^\pm \chi^0$ opens up and becomes the dominant one. After $\Delta m \gtrsim 1\,\text{GeV}$, final states with two and three pions start to give a sizable contribution, and the total decay rate asymptotes to that for $\chi^\pm \to q'\bar{q}\chi^0$. For a larger mass splitting, the mode $\chi^\pm \to \tau^\pm \nu_\tau \chi^0$ may also be allowed. As a whole, these decay modes determine the lifetime of a charged component of a WIMP, which is typically long enough to be probed by experiments thanks to the small mass difference.

Let τ be the lifetime of the (singly) charged component of a WIMP, defined using the total decay rate Γ as $\tau \equiv 1/\Gamma$. Taking into account that a WIMP, if produced at colliders with sufficiently high energy, has a velocity comparable to the speed of light c, $c\tau$ expresses a rough estimation of its flight length inside detectors. For Higgsino with $m_\pi < \Delta m \lesssim 1\,\text{GeV}$,[24] we can estimate [145, 146]

$$c\tau \simeq 0.7\,\text{cm} \left[\left(\frac{\Delta m_+}{340\,\text{MeV}} \right)^3 \sqrt{1 - \frac{m_\pi^2}{\Delta m_+^2}} \right]^{-1}, \tag{4.1}$$

where $\Delta m_+ \equiv \Delta m_+^{\text{tree}} + \Delta m_+^{\text{rad}}$ with using Eqs. (2.4) and (2.5). Since the mass difference for Wino is a factor two smaller than Higgsino, we obtain a much longer flight length

$$c\tau \simeq 3.1\,\text{cm} \left[\left(\frac{\Delta m}{165\,\text{MeV}} \right)^3 \sqrt{1 - \frac{m_\pi^2}{\Delta m^2}} \right]^{-1}, \tag{4.2}$$

which gives $c\tau \simeq 5.8\,\text{cm}$ for $\Delta m = 165\,\text{MeV}$. The same calculation applies to the fermionic MDMs with $n \geq 5$ and $\Delta m = 166\,\text{MeV}$, resulting in somewhat shorter flight length that scales as $c\tau \sim 44\,\text{cm}/(n^2 - 1)$ [83] due to the stronger interaction with W bosons.

(♣ Scalar MDM ♣)

---

[24]We are not interested in Higgsino with $\Delta m \gtrsim 1\,\text{GeV}$ here since the corresponding flight length will be much shorter than $\mathcal{O}(1)\,\text{cm}$, which is the scale of the detectors.

Disappering track signal

Once a long-lived charged component of WIMP is produced, it is detected by the trackers installed in the innermost part of the detectors for the case of ATLAS and CMS collaborations at the LHC. For example, in the ATLAS setup, several tracking detectors are equipped cylindrically around the beamline from the radius $r = 3$ cm to 108 cm. The pixel detector spans the radius from 3 cm to 12 cm, the strip semiconductor tracker (SCT) from 30 cm to 52 cm, and the transition radiation tracker from 56 cm to 108 cm. In particular, the pixel detector is the most important for our discussion, which is composed of four layers, with the innermost one being the recently equipped so-called the insertable B-layer [147–149]. To detect the charged track signal of a long-lived WIMP with the typical flight length of $\mathcal{O}(1)$ cm, they require the hit at every layer of the pixel detector and apply the SCT veto to search for the track signal disappearing in between 12 cm $< r <$ 30 cm. As for the fake events within the SM, the SCT veto denies the possibility for a stable SM particle to mimic the signal. However, there are two important sources of the fake track generated by hadrons/electrons and the so-called pile-up.

The first possibility with hadrons/electrons is a physical background caused by the interaction of hadrons with detector material or by the hard photon emission of electrons. After these interactions, the orbit of a hadron/electron is bent and, if this secondary interaction occurs in between 12 cm $< r <$ 30 cm, two tracks in the pixel detector and the SCT are not identified with each other. As a result, the first track in the pixel detector seems to disappear in the middle, which mimics the true WIMP signals. In the LHC, this type of background dominates and generates $\mathcal{O}(10\text{–}100)$ fake events for $\sqrt{s} = 13$ TeV, $\mathcal{L} = 36.1$ fb^{-1} (see Fig. 7 of [31]).

On the other hand, for future hadron colliders, the second possibility of the fake track from the pile-up may be more important. In hadron colliders, a bunch of protons is accelerated at the same time and two bunches "collide" with each other with some given frequency. Since there are many protons inside a bunch, typically more than one collisions of two protons occur for each bunch crossing. The average number of collisions per bunch crossing is often denoted as $\langle \mu \rangle$ and the values of $\langle \mu \rangle \sim 20$, 80, and 200 are expected for LHC Run-2, Run-3, and HL-LHC. With this large number of collisions, there are a lot of collision products detected almost at the same time, which makes the signal significantly messy. Then, among a huge number of hits on tracking detectors, several of them occasionally form a straight line in position and time, which is sometimes called the fake track. Since this track is only a fake, it can easily pass the SCT veto and mimic the disappearing track signal of WIMPs. In the real experiment, the rate for fake track reduces as we require more hits on trackers. See the results reviewed below for a concrete estimation of the fake track rate at the FCC-hh.

From now on, we estimate how many events are expected at the FCC-hh. Recalling that the detectors are installed in a cylindrical geometry, the transverse distance d_T of the
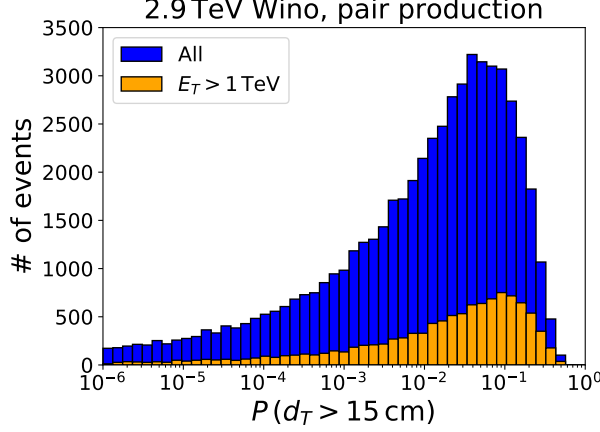
Figure 11:   Distribution of the survival probability $P(d_T > 15\,\mathrm{cm})$ for 2.9 TeV Wino. The pair prodction process at $\sqrt{s} = 100\,\mathrm{TeV}$ and $\mathcal{L} = 30\,\mathrm{ab}^{-1}$ is assumed.

charged WIMP flight measured from the beamline plays an important role. We can estimate the probability for d_T to be larger than d as

$$P(d_T > d) = \exp\left(-\frac{d}{\beta\gamma c\tau \sin\theta}\right),\tag{4.3}$$

where β is the WIMP velocity, $\gamma \equiv (1 - \beta^2)^{-1/2}$, and θ is the angle between the WIMP momentum and the beamline. One of the implications of the above expression is that WIMPs with large transverse momentum have a larger possibility to reach outer layers of the pixel detector. This enlarges the importance of considering the NLO (and higher-order) QCD processes with real emissions for the pair production. Due to the hard emission of the gluon, the produced pair of WIMPs recoil in the opposite direction, and WIMPs tend to have larger transverse momentum than the case without gluon emission. It can be directly checked that, for $\sqrt{s} = 100\,\mathrm{TeV}$, even the two-gluon emission process possesses non-negligible contribution to the simulation of the disappearing track search for WIMPs.

In Fig. 11, we show the distribution of $P(d_T > 15\,\mathrm{cm})$, which is motivated by the FCC-hh detector setup assumed below, for the 2.9 TeV Wino, $\sqrt{s} = 100\,\mathrm{TeV}$, and $\mathcal{L} = 30\,\mathrm{ab}^{-1}$. The blue and orange histograms show the distributions without and with the cut on the missing transverse momentum $\not{E}_T > 1\,\mathrm{TeV}$, respectively, which has been revealed to be efficient to reduce the number of backgrounds [144]. Here, we only consider the WIMP pair production process with up to one gluon emission as an example. Note that $\tau \simeq 5.8\,\mathrm{cm}$ and $\exp(-15\,\mathrm{cm}/\tau) \sim 7.5 \times 10^{-2}$ for this setup. We can see that the effect of the large Lorentz boost $\beta\gamma \gg 1$ pushes the probability to $P \gtrsim \mathcal{O}(10^{-1})$ for some Winos, while the angular distribution of Winos makes a wide tail of the distribution at $P \lesssim \mathcal{O}(10^{-2})$ when
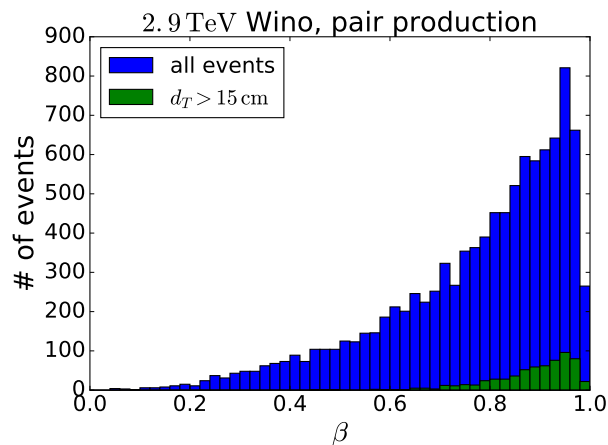
Figure 12:   Distribution of the Wino velocity β for 2.9 TeV Wino. The pair prodction process at $\sqrt{s} = 100$ TeV and $\mathcal{L} = 30$ ab^{-1} is assumed.

$\sin\theta \sim 0$. By summing the shown probabilities for all produced Winos, we can obtain the expectation value N_{15} for the number of Winos with $d_T > 15$ cm. We find $N_{15} \sim 2700$ (700) with (without) the $\not{E}_T$ cut, to which a lot of Winos with $P \gtrsim \mathcal{O}(10^{-1})$ significantly contribute. Thus, we infer that we can detect the Wino signal if we can suppress the number of background events to $\lesssim \mathcal{O}(10^5)$. In the next subsection, we will see that this may be the case for the FCC-hh and the parameter space for the Wino DM candidate can fully be covered.

In Fig. 12, we show the distribution of the Wino velocity β for the same process. The blue and orange histograms show the distributions without and with the $\not{E}_T$ cut, respectively, while the green one shows that with $\not{E}_T > 1$ TeV and $d_T > 15$ cm, picked up randomly according to the survival probability Eq. (4.3). As already seen in Fig. 10, the center of mass energy of the two-Wino system distributes from a few to $\mathcal{O}(10)$ TeV, and many Winos are highly boosted with $\beta \sim 1$. Since a charged Wino tends to survive for a longer distance when it is more accelerated, a non-negligible fraction of the boosted Winos with $\beta \gtrsim 0.6$ satisfy the requirement $d_T > 15$ cm.

Current constraints and future prospects

So far, the disappearing track search is performed by both ATLAS [31] and CMS [33] collaborations. Below, we will focus particularly on the ATLAS collaboration and discuss current constraints.

In Fig. 13, we show the result of the disappearing track search taken from [31]. As for the production process, only the pair production via an electroweak gauge boson is considered. The yellow band shows the current constraint on the WIMP mass and lifetime plane and the
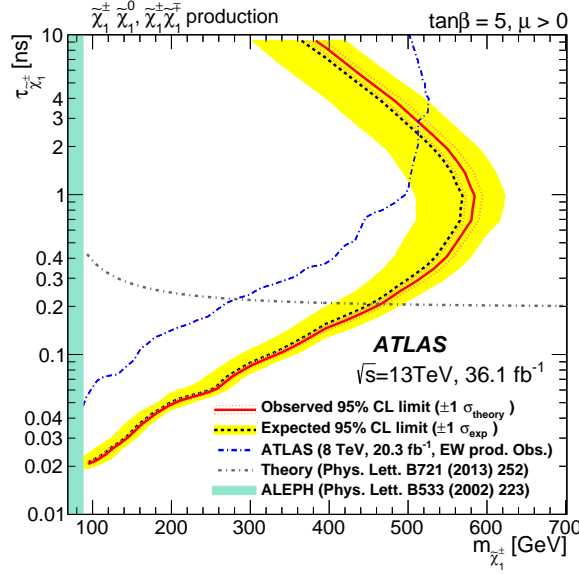
Figure 13:   Current status of the disappearing track search using the pair production process via an electroweak gauge boson. The figure is taken from [31].

WIMP	pure Higgsino	Wino	5-plet fermion
Upper bound on m_χ	152 GeV	460 GeV	267 GeV

Table 10:   Current upper bounds for WIMP masses obtained from the disappearing track search. Results are taken from [31–34].

left part of the band is already excluded. The sensitivity becomes weak when we consider $\tau \gtrsim 1$ ns or $c\tau \gtrsim 30$ cm due to the requirement of the SCT veto. In the figure, the lifetime of Wino as a function of its mass is also shown by the black dot-dashed line. It can be seen that the current constraint on Wino mass is $m_\chi \lesssim 460$ GeV.

Using the lifetime evaluated in the previous subsection, we summarize the current status for several WIMPs in Table 10, which exhibits upper limits of $\mathcal{O}(100)$ GeV. However, note that the bound for the Higgsino listed in the table neglects the mixing between Higgsino and gauginos. Actually, Δm_+ and thus τ are sensitive to the mixing, and an order estimation shows that the mixing lowers the lifetime to be $\tau \lesssim 0.01$ ns and spoils the bound for Higgsino when M_1, $M_2 \lesssim 100$ TeV without any non-trivial cancellation in Eq. (2.4). Note also that the bound for 5-plet fermion is weaker than that for Wino in spite of the much larger production cross section because of the smaller lifetime.

The analysis of the disappearing track search at future hadron colliders is performed in [48, 150]. Since the detector setup for future colliders such as the FCC-hh is undetermined

Detector setup	pure Higgsino	Wino
$r_5 = 15\,\text{cm}$	0.9–1.2 TeV	> 4.0 TeV
$r_5 = 27\,\text{cm}$	< 0.7 TeV	2.9–4.0 TeV

Table 11:   Prospects of 5σ discovery reach of the disappearing track search at the FCC-hh with $\mathcal{L} = 30\,\text{ab}^{-1}$ using the pair production process via an electroweak gauge boson. The results are based on [150].

yet, in [150], the authors assume several setups and compare the result. In each setup, five layers of the pixel detector are installed and the fifth layer position (which we call r_5) ranges from 15 cm to 27 cm.[♮25] For the background reduction, hits to all of the five layers are required. By varying the average number of pp interactions per bunch crossing from $\langle \mu \rangle = 200$ to 500, the fake background rate is estimated to range from 10^{-7} to 10^{-5}.

In Table 11, we summarize the obtained 5σ discovery reach for pure Higgsino and Wino for two detector setups with the integrated luminosity $\mathcal{L} = 30\,\text{ab}^{-1}$, again using the pair production process via an electroweak gauge boson. The uncertainty of the reach corresponds to the variation of $\langle \mu \rangle = 200$–500 and the uncertainty in soft QCD processes. Recalling the discussion in Sec. 3.1, Table 11 shows that the FCC-hh can cover the whole region of the parameter space consistent with Wino DM $m_\chi \lesssim 2.9\,\text{TeV}$. On the other hand, there is a sensitivity up to the mass of the thermal Higgsino DM $m_\chi \sim 1.1\,\text{TeV}$ only when we adopt the most optimistic assumption, *i.e.*, the pure Higgsino with small Δm_+ searched for with $r_5 = 15\,\text{cm}$. Thus, it is an important task to consider another way of search for Higgisno, in particular, a way that is unaffected by the mass splitting Δm_+. The authors do not give any comment on the MDM search, but we can give some very rough estimates of the reach from Table 11. For example, considering the 5-plet fermion with $c\tau \sim 1.8\,\text{cm}$, the size of the significance of the signal should be in between that for Higgsino and Wino assuming the same production cross section, while the cross section scales as n^3 as a function of the $SU(2)_L$ charge as we have seen so far. Thus, the reach for the 5-plet fermion should be a few TeV, which covers a non-negligible fraction of the parameter space viable as a DM candidate.

4.3   Soft lepton search

(♣ If possible ♣)

[♮25]For simplicity of the discussion, we just assume that the detectors outside the pixel detector are far apart from the beamline so that all the WIMPs decay before reaching them. Then, we can estimate the discovery reach by counting the number of WIMP signals that reach the fifth layer of the pixel detector.

systematic error σ_B	Higgsino	Wino
1 %	0.5 TeV	1 TeV
2 %	0.2 TeV	0.5 TeV

Table 12:   Prospects of 5σ discovery reach of the mono-jet search at the FCC-hh with $\mathcal{L} = 30\,\text{ab}^{-1}$ using the pair production process via an electroweak gauge boson. The results are based on [48].

4.4   Mono-jet search

Another way of identifying the WIMP events is to look for the mono-jet events. The relevant process is shown in the left panel of Fig. 9; if the WIMP pair production occurs with an initial state radiation (ISR) jet but both of the WIMPs are unobserved by detectors, the unique object that is observed is the ISR jet. In the mono-jet search, we require this jet to be sufficiently hard and use it to trigger and tag the event as an event related to the new physics.

Since the event topology is astonishingly simple, there are a huge number of background events within the SM. The dominant background comes from the Z+jet production with Z decaying into two neutrinos. Besides, the W+jet production followed by the leptonic decay of the W-boson has a comparable contribution because the charged lepton in the final state may fall outside the detector coverage. Finally, a sub-dominant but non-negligible contribution to the background comes from the top pair production process and so on. These background events lead to the small signal-to-background ratio (S/B) of the 1 % level both within the current setup and the future prospect, which makes this method highly challenging.

Considering the small ratio S/B, the systematic errors may also shrink the discovery reach of WIMPs in this method. At worst, these errors should be as small as the 1 % level to obtain some meaningful result. However, this may be overcome by future endeavors both in the theory and experimental sides. For example, the theoretical and experimental values of the relevant cross sections are already controlled with high precision. In the theory side, the errors in the calculation is reduced to a few percent level by including the next-to-next-to-leading order QCD and the NLO electroweak effects, and performing the next-to-leading logarithmic resummation of the electroweak Sudakov factors [151]. In the experimental side, the uncertainties on the estimation of the cross section of background events from the date are also at a few percent level [152]. These errors are expected to be reduced with the calculation of the higher order loop effects and the accumulation of more data.

The main focus of this method is on the short lifetime Higgsino since the other long-lived WIMPs will be more efficiently searched for by the disappearing track search. Unfortunately, due to the small ratio S/B, there is no constraint on the Higgsino from the mono-jet search

[35]. As for the future prospects, we show the prospects of 5σ discovery reach for Higgsino and Wino taken from [48] in Table 12. To obtain the result, the authors introduce the parameter σ_B (σ_S) that expresses the unknown systematic uncertainty on the background (signal) and define the p-value as

$$p \equiv \frac{S}{\sqrt{B + (\sigma_B B)^2 + (\sigma_S S)^2}}, \tag{4.1}$$

where B and S are the number of background and signal events, respectively. The denominator combines the errors from the statistical fluctuation (the corresponding standard deviation equals $\sqrt{B}$), the systematic errors on the background ($\sigma_B B$), and those on the signal ($\sigma_S S$), assuming that all of the above are uncorrelated with each other. They fix $\sigma_S = 10\,\%$ and use two different choices $\sigma_B = 1\,\%$ and $2\,\%$ as the table shows. The values on the table correspond to the WIMP masses that give $p = 5$.

From the table, we can see that the result highly depends on the choice of σ_B. In particular, it is important to suppress $\sigma_B \lesssim 1\,\%$ to obtain a strong discovery reach on Higgsino. Besides, it can be checked that the coverage of the Wino parameter space is much smaller than that of the disappearing track search, mainly due to the small ratio S/B.

Section 5

Indirect search of WIMPs using Drell-Yan process

(♣ **Histogram of lepton invariant mass?** ♣)

So far, we have argued several ways to search for WIMPs using DM searches and collider experiments. We have seen that, while WIMPs with relatively large $SU(2)_L$ charges such as Wino and the 5-plet fermion are promising for these searches, Higgsino is typically more challenging to probe. Given this situation, another search strategy attracts a lot of attention [1, 2, 36–40, 153, 154] that probes WIMPs via the electroweak precision measurement at colliders. It utilizes a pair production of charged leptons or that of a charged lepton and a neutrino, where WIMPs affect the pair production processes through the vacuum polarizations of the electroweak gauge bosons as shown in Fig. 14. It is an indirect search method in the sense that it does not produce on-shell WIMPs as final states. A virtue of this method is that it is robust against the change of the lifetime and the decay modes of WIMPs and whether a WIMP constitutes a sizable portion of the DM or not. Another important point is that, due to WIMPs, the invariant mass distributions of the final state particles show sharp dip-like behavior at the invariant mass close to twice the WIMP mass. It helps us to distinguish the WIMP effects from backgrounds and systematic errors.

In this section, we pursue this indirect search method further. In particular, we study the prospect of the indirect search method at future $100\,\mathrm{TeV}$ hadron colliders such as FCC-hh [41–43, 129] and SppC [44, 45]. We concentrate on the Drell-Yan processes that have
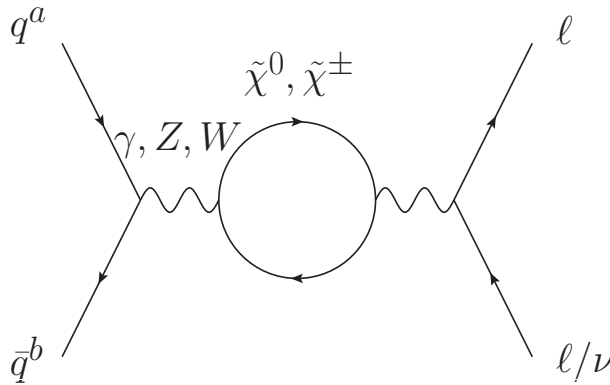

Figure 14: WIMP effect on the Drell-Yan processes considered in this section. (♣ **Correct the figure to** $q_\alpha q_\beta \to \cdots$. ♣)

two charged leptons or mono-lepton plus a neutrino in the final state since they provide a very clean signal without any hadronic jets at least from the final state particles. We will show that it provides *a comparable or better experimental reach for Higgsino* compared to the direct production search of WIMPs at future colliders [46–49]. Besides, we demonstrate that the indirect search method can be applied not only to discover WIMPs but also *to investigate their properties, such as charges, masses, and spins.* To this end, it is important to consider both the charged current (CC) process with two-lepton final state and the neutral current (NC) process with mono-lepton final state to break some degeneracy among different WIMP charge assignments; the NC and CC processes depend on different combinations of the $SU(2)_L$ and $U(1)_Y$ charges of WIMP, and hence the inclusion of both processes allows us to extract these charges separately.

This section is based on our works [1, 2].

5.1 WIMP effect on the Drell-Yan processes

We investigate contributions of the WIMPs to the Drell-Yan processes through the vacuum polarization of the electroweak gauge bosons at the loop level. Throughout this section, we assume that all the other beyond the SM particles are heavy enough so that they do not affect the following discussion. After integrating out the WIMPs, the effective lagrangian is expressed as

$$\mathcal{L}_{\text{eff}} = \mathcal{L}_{\text{SM}} + C_2 g^2 W^a_{\mu\nu} f\left(-\frac{D^2}{m^2}\right) W^{a\mu\nu} + C_1 g'^2 B_{\mu\nu} f\left(-\frac{\partial^2}{m^2}\right) B^{\mu\nu}, \tag{5.1}$$

where $\mathcal{L}_{\text{SM}}$ is the SM Lagrangian, D is a covariant derivative, m is the WIMP mass,[26] g and g' are the $SU(2)_L$ and $U(1)_Y$ gauge coupling constants, and $W^a_{\mu\nu}$ and $B_{\mu\nu}$ are the field strength associated with the $SU(2)_L$ and $U(1)_Y$ gauge group, respectively. The function $f(x)$ is defined as[27]

$$f(x) = \begin{cases} \dfrac{1}{16\pi^2} \displaystyle\int_0^1 dy\, y(1-y) \ln(1 - y(1-y)x - i0) & \text{(Fermion)}, \\[4mm] \dfrac{1}{16\pi^2} \displaystyle\int_0^1 dy\, (1-2y)^2 \ln(1 - y(1-y)x - i0) & \text{(Scalar)}, \end{cases} \tag{5.2}$$

---

[26]Here we neglect a small mass splitting among the $SU(2)_L$ multiplet.

[27]If a WIMP interacts only through the electroweak interaction, its decay width is of O(1)% or less of its mass even if it is unstable. We assume that this is the case, and neglect the small effect on the function $f(x)$ due to the small decay width. Also, $f(x)$ corresponds to the finite part of the WIMP loop contribution after performing the renoramlization in the $\overline{\text{MS}}$ scheme.

Fermion f	$v_f^{(\gamma)}$	$a_f^{(\gamma)}$	$v_f^{(Z)}$	$a_f^{(Z)}$	$v_f^{(W)}$	$a_f^{(W)}$
up-type quark	$\frac{2}{3}e$	0	$(\frac{1}{4} - \frac{2}{3}s_W^2)g_Z$	$-\frac{1}{4}g_Z$	$\frac{1}{2\sqrt{2}}g$	$-\frac{1}{2\sqrt{2}}g$
down-type quark	$-\frac{1}{3}e$	0	$(-\frac{1}{4} + \frac{1}{3}s_W^2)g_Z$	$\frac{1}{4}g_Z$	$\frac{1}{2\sqrt{2}}g$	$-\frac{1}{2\sqrt{2}}g$
lepton	$-e$	0	$(-\frac{1}{4} + s_W^2)g_Z$	$\frac{1}{4}g_Z$	$\frac{1}{2\sqrt{2}}g$	$-\frac{1}{2\sqrt{2}}g$

Table 13: Coefficients of the weak interaction defined as $\Gamma_f^{(V)} \equiv v_f^{(V)} + a_f^{(V)}\gamma_5$. Here, $e = gs_W$ and $g_Z = g/c_W$, where $s_W \equiv \sin\theta_W$ and $c_W \equiv \cos\theta_W$ with θ_W being the weak mixing angle.

where the first (second) line corresponds to a fermionic (scalar) WIMP, respectively. The coefficients C_1 and C_2 for an $SU(2)_L$ n-plet WIMP with hypercharge Y are given by

$$C_1 = \frac{\kappa}{8}nY^2, \tag{5.3}$$

$$C_2 = \frac{\kappa}{8}I(n), \tag{5.4}$$

where $\kappa = 1, 2, 8, 16$ for a real scalar, a complex scalar, a Weyl or Majorana fermion, and a Dirac fermion, respectively. $I(n)$ is the Dynkin index for the n dimensional representation of $SU(2)_L$ defined in Eq. (??). The coefficients are uniquely determined by the representation of the WIMPs. For example, $(C_1, C_2) = (1, 1)$ for Higgsino, and $(C_1, C_2) = (0, 2)$ for Wino. We emphasize that, contrary to the usual effective field theory, our prescription is equally applied when the typical scale of the gauge boson four-momentum q is larger than the WIMP mass scale m since we do not perform a derivative expansion of f in Eq. (5.1). It is important because, as we see soon, the effect of the WIMPs is maximized when $\sqrt{q^2} \sim m$, where the derivative expansion is not applicable.

At the leading order (LO), we are interested in $u(p)\,\bar{u}(p') \to \ell^-(k)\,\ell^+(k')$ and $d(p)\,\bar{d}(p') \to \ell^-(k)\,\ell^+(k')$ as the NC processes and $u(p)\,\bar{d}(p') \to \nu(k)\,\ell^+(k')$ and $d(p)\,\bar{u}(p') \to \ell^-(k)\,\bar{\nu}(k')$ as the CC processes. Here, u and d collectively denote up-type and down-type quarks, respectively, and p, p', k, and k' are initial and final state momenta. In the SM, the amplitudes for both the NC and CC processes at the LO are expressed as

$$\mathcal{M}_{\text{SM}} = \sum_V \frac{\left[\bar{v}(p')\gamma^\mu \Gamma_q^{(V)} u(p)\right]\left[\bar{u}(k)\gamma_\mu \Gamma_\ell^{(V)} v(k')\right]}{s' - m_V^2}, \tag{5.5}$$

where $\sqrt{s'}$ is the invariant mass of the final state leptons, which is denoted as $m_{\ell\ell}$ for the NC processes and $m_{\ell\nu}$ for the CC processes. The relevant gauge bosons are $V = \gamma, Z$ for the NC processes and $V = W^\pm$ for the CC processes, with m_V being the corresponding gauge boson mass. In addition,

$$\Gamma_f^{(V)} \equiv v_f^{(V)} + a_f^{(V)}\gamma_5, \tag{5.6}$$

with $v_f^{(V)}$ and $a_f^{(V)}$ given in Tab. 13. The WIMP contribution is given by

$$\mathcal{M}_{\mathrm{WIMP}} = \sum_{V,V'} C_{VV'} s' f\left(\frac{s'}{m^2}\right) \frac{\left[\bar{v}(p')\gamma^\mu \Gamma_q^{(V)} u(p)\right]\left[\bar{u}(k)\gamma_\mu \Gamma_\ell^{(V')} v(k')\right]}{(s'-m_V^2)(s'-m_{V'}^2)}, \tag{5.7}$$

where $C_{\gamma\gamma} = 4(C_1 g'^2 c_W^2 + C_2 g^2 s_W^2)$, $C_{\gamma Z} = C_{Z\gamma} = 4(C_2 g^2 - C_1 g'^2)s_W c_W$, $C_{ZZ} = 4(C_1 g'^2 s_W^2 + C_2 g^2 c_W^2)$, and $C_{WW} = 4C_2 g^2$. Again $V, V' = \gamma, Z$ for the NC processes and $V, V' = W^\pm$ for the CC processes.

We use $d\Pi_{\mathrm{LIPS}}$ for a Lorentz invariant phase space factor for the two particles final state. Then, using Eqs. (5.5) and (5.7), we define

$$\frac{d\sigma_{\mathrm{SM}}}{d\sqrt{s'}} = \sum_{\alpha,\beta} \frac{dL_{\alpha\beta}}{d\sqrt{s'}} \int d\Pi_{\mathrm{LIPS}} \left|\mathcal{M}_{\mathrm{SM}}(q_\alpha q_\beta \to \ell\ell/\ell\nu)\right|^2, \tag{5.8}$$

$$\frac{d\sigma_{\mathrm{WIMP}}}{d\sqrt{s'}} = \sum_{\alpha,\beta} \frac{dL_{\alpha\beta}}{d\sqrt{s'}} \int d\Pi_{\mathrm{LIPS}} \, 2\Re\left[\mathcal{M}_{\mathrm{SM}}\mathcal{M}_{\mathrm{WIMP}}^*(q_\alpha q_\beta \to \ell\ell/\ell\nu)\right], \tag{5.9}$$

where we take the average and summation over spins. Here, $dL_{\alpha\beta}/d\sqrt{s'}$ is the so-called luminosity function for a fixed $\sqrt{s'}$:

$$\frac{dL_{\alpha\beta}}{d\sqrt{s'}} \equiv \frac{1}{s} \int_0^1 dx_1 dx_2 \, f_\alpha(x_1) f_\beta(x_2) \delta\left(\frac{s'}{s} - x_1 x_2\right), \tag{5.10}$$

where α and β denote species of initial partons, $\sqrt{s} = 100\,\mathrm{TeV}$, and $f_a(x)$ is the PDF used in Sec. 4.1. Eq. (5.8) represents the SM cross section, while Eq. (5.9) the WIMP contribution to the cross section. For the statistical treatment in the next section, we introduce a parameter μ that parametrizes the strength of the WIMP effect, and express the cross section with μ as

$$\frac{d\tilde{\sigma}}{d\sqrt{s'}} = \frac{d\sigma_{\mathrm{SM}}}{d\sqrt{s'}} + \mu \frac{d\sigma_{\mathrm{WIMP}}}{d\sqrt{s'}}. \tag{5.11}$$

Obviously, $\mu = 0$ corresponds to the pure SM, while $\mu = 1$ corresponds to the SM+WIMP model. Hereafter, we use

$$\delta_\sigma(\sqrt{s'}) \equiv \frac{d\sigma_{\mathrm{WIMP}}/d\sqrt{s'}}{d\sigma_{\mathrm{SM}}/d\sqrt{s'}}, \tag{5.12}$$

to denote the correction from the WIMP. Note that this ratio remains unchanged even if we take into account the next-to-leading order (NLO) QCD effect because the EWIMPs affect the cross sections only through the vacuum polarization.[28]

---

[28]When the NLO QCD effect is included, one of the initial partons can be gluon with the real emission of one jet in the final state. However, we can easily see that $\delta_\sigma^{ug} = \delta_\sigma^{uu}$ and so on.
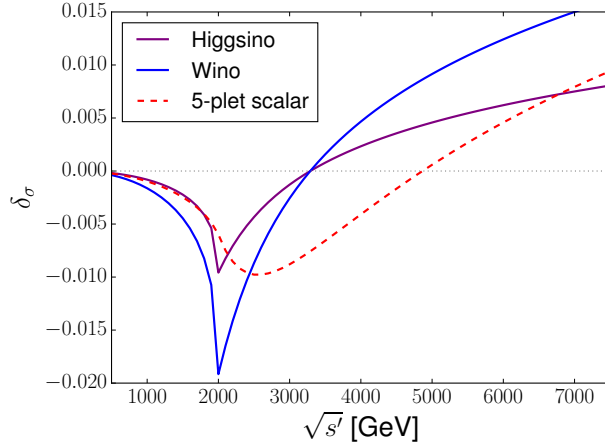
Figure 15: δ_σ for the CC processes as a function of $\sqrt{s'} = m_{\ell\nu}$. The purple, blue, and red lines correspond to Higgsino, Wino, and 5-plet real scalar, respectively.
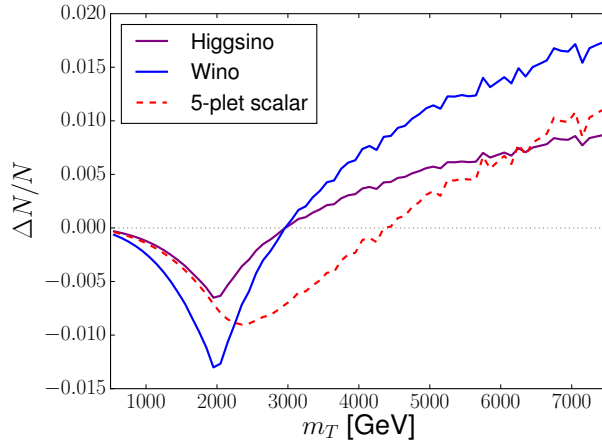

Figure 16:   The WIMP effect on the ratio of the number of events $\Delta N/N$ as a function of m_T. The line colors are the same as Fig. 15.

In Fig. 15, we plot δ_σ for the CC processes as a function of $\sqrt{s'}$. The purple, blue, and red lines correspond to Higgsino, Wino, and 5-plet scalar, respectively. There is a dip around $\sqrt{s'} = 2m$ for all the cases of the WIMPs which originates from the loop function f in Eq. (5.2). The WIMP contributions to the NC processes show a similar dip structure that again comes from f. This dip is crucial not only for the discovery of the WIMP signal (see Sec. 5.2.3) but also for the determination of the properties of the WIMPs (see Sec. 5.2.4). In particular, the WIMP mass can be extracted from the dip position, while the WIMP charges (n and Y) can be determined from the depth of the dip.

For the NC processes, the momenta of two final state charged leptons are measurable and we can use the invariant mass distribution of the number of events for the study of the WIMPs. For the CC processes, on the contrary, we cannot measure the momentum of the neutrino in real experiments, and hence we instead use the missing transverse momentum $\not{p}_T$. We use the transverse mass defined as

$$m_T^2 \equiv 2p_{T,\ell}\, \not{p}_T \left(1 - \cos\phi\right), \tag{5.13}$$

where $p_{T,\ell}$ denotes the transverse momentum of the charged lepton and ϕ is the difference between the azimuth angles of $p_{T,\ell}$ and $\not{p}_T$. The important property of m_T is that the distribution of m_T peaks at $m_T = m_{\ell\nu}$ (see Appendix. D for more detailed description of the quantity m_T). Because of this property, the characteristic shape of δ_σ remains in the m_T distribution in the CC events. To see this, we plot in Fig. 16 the WIMP effect on the number of events as a function of m_T. Here, the vertical axis is the ratio of the WIMP correction to the number of events ΔN to the number of events in the SM N for each bin with the bin width of $100\,\mathrm{GeV}$.[29] We find that the dip structure remains in the m_T distribution, though the depth of the dip is smaller compared to the $m_{\ell\nu}$ distribution.

5.2   Analysis

(♣ **Some comment on lepton mis-tagging?** ♣)

5.2.1   Event generation

Now we discuss how well we can extract information about WIMPs from the invariant mass and transverse mass distributions for the processes of our concern at future $100\,\mathrm{TeV}$ pp collider experiments. We take into account the effects of the next-to-leading order QCD corrections in the events as well as detector effects through Monte-Carlo simulations.

In our analysis, we first generate the SM event sets for the NC processes $pp \to e^-e^+/\mu^-\mu^+$ and for the CC processes $pp \to e^\pm\nu_e/\mu^\pm\nu_\mu$. We use `MadGraph5_aMC@NLO` (`v2.6.3.2`) [138,139] for the event generation with the successive use of `Pythia8` [140] for the parton shower and the hadronization and `Delphes` (`v3.4.1`) [141] with the card `FCChh.tcl` for the detector simulation. We use `NNPDF2.3QED` with $\alpha_s(M_Z) = 0.118$ [143] as a canonical set of PDFs. For the renormalization and factorization scales, we use the default values of `MadGraph5_aMC@NLO`, i.e., the central m_T^2 scale after k_T-clustering of the event (which we denote by Q). We take into account the NLO QCD effect by the `[QCD]` option of `MadGraph5_aMC@NLO` since

---

[29]Just for an illustrative purpose, we generate events corresponding to the integrated luminosity $\mathcal{L} = 1\,\mathrm{ab}^{-1}$ for this figure, which is not the same luminosity as we use in the next section (see Sec. 5.2.1 for details of the event generation).

it enhances the cross section roughly by a factor of 2 compared to the LO calculation.[30] The events are binned by the characteristic mass m_{char} for each process: we use the lepton invariant mass $m_{\mathrm{char}} = m_{\ell\ell}$ for the NC processes, and the transverse mass $m_{\mathrm{char}} = m_T$ for the CC processes, respectively. In both cases, we generated events with the characteristic mass within the range of $500\,\mathrm{GeV} < m_{\mathrm{char}} < 7.5\,\mathrm{TeV}$ and divide them into 70 bins with the equal width of $100\,\mathrm{GeV}$.

As for the event selection by a trigger, we may have to impose some cut on the lepton transverse momentum p_T. As we will see, we concentrate on events with high p_T charged lepton(s) with which we expect the event may be triggered. For the NC processes, we use events with at least two high p_T leptons. For our analysis, we use events with $m_{\ell\ell} > 500$ GeV; we assume that such events are triggered by using two energetic charged leptons so that we do not impose extra kinematical requirements. On the contrary, the CC events are characterized only by a lepton and a missing transverse momentum. For such events, we require that the p_T of the charged lepton should be larger than $500\,\mathrm{GeV}$. [31] For the CC events, the cut reduces the number of events in particular for the bins with the low transverse mass $m_T \sim 500\,\mathrm{GeV}$, and thus affects the sensitivity of the CC processes to relatively light WIMPs. We will come back to this point later.

The WIMP effect is incorporated by rescaling the SM event by δ_σ defined in Eq. (5.12). With the parameter μ defined in Eq. (5.11), the number of events corresponding to the SM+WIMP hypothesis in i-th bin, characterized by $m_{i,\mathrm{min}} < m_{\mathrm{char}} < m_{i,\mathrm{max}}$, is

$$x_{f,i}(\mu) = \sum_{m_{i,\mathrm{min}}<m_{\mathrm{char}}<m_{i,\mathrm{max}}} \left[1 + \mu\delta_\sigma(\sqrt{s'})\right], \tag{5.1}$$

where the sum runs over all the events of the final state f whose characteristic mass m_{char} (after taking into account the detector effects) falls into the bin. Note that the true value of $\sqrt{s'}$ should be used for each event for the computation of δ_σ: we extract it from the hard process information.[32]

---

[30]This large enhancement implies that the next-to-next-to-leading order QCD effect may also have a non-negligible effect on the cross section, and its calculation remains as a future task. However, due to its smooth dependence on $\sqrt{s'}$, it may not much affect the detection reach of the EWIMPs. See Sec. 5.2.2 for the details.

[31]In the ATLAS analysis of the mono-lepton signal during the 2015 (2016) data taking period [155], they use the event selection condition $p_T > 24\,(60)\,\mathrm{GeV}$ for leptons that satisfy the *medium* identification criteria. In the CMS analysis during the period on 2016 [156], they use the condition $p_T > 130(53)\,\mathrm{GeV}$ for an electron (a muon).

[32]The p_T cut for the CC process does not affect this estimation since the WIMP does not modify the angular distribution of the final lepton and neutrino for the CC process.

5.2.2   Statistical treatment

We now explain the statistical method we will adopt in our analysis. Throughout this section, we rely on the so-called profile likelihood method, which is described in detail in Appendix E. We collectively denote our theoretical model as $\boldsymbol{x}_f(\mu) = \{x_{f,i}(\mu)\}$, where $x_{f,i}(\mu)$ is given by Eq. (5.1). We denote the experimental data set as $\check{\boldsymbol{x}}_f$ that in principle is completely unrelated to our theoretical model $\boldsymbol{x}_f(\mu)$. Since we do not have an actual experimental data set for 100 TeV colliders for now, however, we take $\check{\boldsymbol{x}}_f = \boldsymbol{x}_f(\mu = 1)$ (for some fixed values of the WIMP mass and charges) throughout our analysis, assuming that the WIMP does exist. In particular, this choice tests the SM-only hypothesis if we take our theoretical model as $\boldsymbol{x}_f(\mu = 0)$.

   If the expectation values of $x_{f,i}(\mu)$ are precisely known, the sensitivity to WIMPs can be studied only with statistical errors. In reality, however, the computation of $x_{f,i}(\mu)$ suffers various sources of uncertainties, which results in systematic errors in our theoretical model. The sources include errors in the integrated luminosity, the beam energy, choices of the renormalization and the factorization scales, choices of PDF, the pile-up effect, higher order corrections to the cross section, and so on. In order to deal with these uncertainties, we introduce sets of free parameters $\boldsymbol{\theta}_f = \{\theta_{f,\alpha}\}$ (i.e. nuisance parameters) which absorb (smooth) uncertainties of the number of events, and modify our theoretical model as

$$\tilde{x}_{f,i}(\boldsymbol{\theta}_f, \mu) \equiv x_{f,i}(\mu) f_{\mathrm{sys},i}(\boldsymbol{\theta}_f), \tag{5.2}$$

where $f_{\mathrm{sys},i}(\boldsymbol{\theta}_f)$ is a function that satisfies $f_{\mathrm{sys},i}(\boldsymbol{0}) = 1$. We expect that, if the function $f_{\mathrm{sys},i}$ is properly chosen, the true distribution of the number of events in the SM is given by $\tilde{\boldsymbol{x}}_f(\boldsymbol{\theta}_f, 0) = \{\tilde{x}_{f,i}(0) f_{\mathrm{sys},i}(\boldsymbol{\theta}_f)\}$ for some value of $\boldsymbol{\theta}_f$. In our analysis, we adopt the five parameters fitting function given by [157]

$$f_{\mathrm{sys},i}(\boldsymbol{\theta}_f) = e^{\theta_{f,1}} (1 - p_i)^{\theta_{f,2}} p_i^{(\theta_{f,3} + \theta_{f,4} \ln p_i + \theta_{f,5} \ln^2 p_i)}, \tag{5.3}$$

where $p_i = 2m_i/\sqrt{s}$ with m_i being the central value of the lepton invariant mass (transverse mass) of the i-th bin for the NC (CC) processes. As we will see, the major effects of systematic errors can be absorbed into $\boldsymbol{\theta}_f$ with this fitting function.

   To test the SM-only hypothesis, we define the following test statistic [158]:

$$q_0 \equiv -2 \sum_{f=\ell\ell,\ell\nu} \ln \frac{L(\check{\boldsymbol{x}}_f; \hat{\hat{\boldsymbol{\theta}}}_f, \mu = 0)}{L(\check{\boldsymbol{x}}_f; \hat{\boldsymbol{\theta}}_f, \hat{\mu})}. \tag{5.4}$$

Here, $\hat{\hat{\boldsymbol{\theta}}}_f$ and $\{\hat{\boldsymbol{\theta}}_f, \hat{\mu}\}$ are determined so that $\prod_f L(\check{\boldsymbol{x}}_f; \boldsymbol{\theta}_f, \mu = 0)$ and $\prod_f L(\check{\boldsymbol{x}}_f; \boldsymbol{\theta}_f, \mu)$ are maximized, respectively. The likelihood function is defined as

$$L(\check{\boldsymbol{x}}_f; \boldsymbol{\theta}_f, \mu) \equiv L_{\boldsymbol{\theta}_f}(\check{\boldsymbol{x}}_f; \mu) L'(\boldsymbol{\theta}_f; \boldsymbol{\sigma}_f), \tag{5.5}$$

where

$$L_{\boldsymbol{\theta}_f}(\check{\boldsymbol{x}}_f; \mu) \equiv \prod_i \exp\left[-\frac{(\check{x}_{f,i} - \tilde{x}_{f,i}(\boldsymbol{\theta}_f, \mu))^2}{2\tilde{x}_{f,i}(\boldsymbol{\theta}_f, \mu)}\right], \tag{5.6}$$

$$L'(\boldsymbol{\theta}_f; \boldsymbol{\sigma}_f) \equiv \prod_\alpha \exp\left[-\frac{\theta_{f,\alpha}^2}{2\sigma_{f,\alpha}^2}\right]. \tag{5.7}$$

The product in Eq. (5.6) runs over all the bins, while the product in Eq. (5.7) runs over all the free parameters we introduced. For each $\theta_{f,\alpha}$, we define the "standard deviation" $\sigma_{f,\alpha}$, which parametrizes the possible size of $\theta_{f,\alpha}$ within the SM with the systematic errors.[♮33] If the systematic errors are negligible compared with the statistical error, we can take $\boldsymbol{\sigma}_f \to \boldsymbol{0}$, while the analysis with $\boldsymbol{\sigma}_f \to \infty$ assumes no knowledge of systematic errors and gives a conservative result. We identify $\sqrt{q_0} = 5$ (1.96) as the detection reach at the 5σ (95 % C.L.) level, since q_0 asymptotically obeys a chi-square distribution with the degree of freedom one.

In order to determine $\boldsymbol{\sigma}_f$, we consider the following sources of the systematic errors:

- Luminosity ($\pm 5\,\%$ uncertainty is assumed),

- Renormalization scale ($2Q$ and $Q/2$, instead of Q),

- Factorization scale ($2Q$ and $Q/2$, instead of Q),

- PDF choice (We use 101 variants of NNPDF2.3QED with $\alpha_s(M_Z) = 0.118$ [143] provided by LHAPDF6 [159] with IDs ranging from 244600 to 244700).

The values of $\boldsymbol{\sigma}_f$ are determined as follows. Let $\boldsymbol{y}_f$ be the set of number of events in the SM for the final state f with the canonical choices of the parameters, and $\boldsymbol{y}_f'$ be that with one of the sources of the systematic errors being varied. We minimize the chi-square function defined as

$$\chi_f^2 \equiv \sum_i \frac{\left(y_{f,i}' - \tilde{y}_{f,i}(\boldsymbol{\theta}_f)\right)^2}{\tilde{y}_{f,i}(\boldsymbol{\theta}_f)}, \tag{5.8}$$

where

$$\tilde{y}_{f,i}(\boldsymbol{\theta}_f) \equiv y_{f,i} f_{\mathrm{sys},i}(\boldsymbol{\theta}_f), \tag{5.9}$$

for each final state f, and determine the best-fit values of $\boldsymbol{\theta}_f$ for each set of $\boldsymbol{y}_f'$. We repeat this process for different sets of $\boldsymbol{y}_f'$, and $\boldsymbol{\sigma}_f$ are determined from the distributions of the best-fit values of $\boldsymbol{\theta}_f$. For example, let us denote the best-fit values for the fit associated with

---

[♮33]Here we assume the Gaussian form for the nuisance parameter distribution. The dependence of the results on the choice of the distribution will be discussed later in Sec. 5.2.3.

Sources of systematic errors	$\sigma_{ee,1}$	$\sigma_{ee,2}$	$\sigma_{ee,3}$	$\sigma_{ee,4}$	$\sigma_{ee,5}$
Luminosity: $\pm 5\%$ ($\boldsymbol{\sigma}_{ee}^{\text{lumi.}}$)	0.05	0	0	0	0
Renormalization scale: $2Q, Q/2$ ($\boldsymbol{\sigma}_{ee}^{\text{ren.}}$)	0.4	0.6	0.3	0.05	0.004
Factorization scale: $2Q, Q/2$ ($\boldsymbol{\sigma}_{ee}^{\text{fac.}}$)	0.3	0.5	0.2	0.06	0.004
PDF choice ($\boldsymbol{\sigma}_{ee}^{\text{PDF}}$)	0.4	0.7	0.3	0.06	0.004

Table 14: Values of $\boldsymbol{\sigma}_{ee}$ for each source of systematic errors. The result is the same for the $\mu\mu$ final state.

Sources of systematic errors	$\sigma_{e\nu_e,1}$	$\sigma_{e\nu_e,2}$	$\sigma_{e\nu_e,3}$	$\sigma_{e\nu_e,4}$	$\sigma_{e\nu_e,5}$
Luminosity: $\pm 5\%$ ($\boldsymbol{\sigma}_{e\nu_e}^{\text{lumi.}}$)	0.05	0	0	0	0
Renormalization scale: $2Q, Q/2$ ($\boldsymbol{\sigma}_{e\nu_e}^{\text{ren.}}$)	0.3	0.4	0.2	0.04	0.003
Factorization scale: $2Q, Q/2$ ($\boldsymbol{\sigma}_{e\nu_e}^{\text{fac.}}$)	1.0	1.6	0.6	0.1	0.01
PDF choice ($\boldsymbol{\sigma}_{e\nu_e}^{\text{PDF}}$)	0.6	0.9	0.4	0.08	0.006

Table 15: Best fit values of fit parameters for several sources of systematic errors for the $e\nu_e$ final state. The result is the same for the $\mu\nu_\mu$ final state.

the luminosity errors $\pm 5\%$ as $\boldsymbol{\theta}_f^{\pm}$. We estimate $\boldsymbol{\sigma}_f$ associated with these errors, denoted here as $\boldsymbol{\sigma}_f^{\text{lumi.}}$, as

$$\sigma_{f,\alpha}^{\text{lumi.}} = \sqrt{\frac{(\theta_{f,\alpha}^+)^2 + (\theta_{f,\alpha}^-)^2}{N}}, \tag{5.10}$$

where N denotes the number of fitting procedures we have performed: $N = 2$ for this case. We estimate $\boldsymbol{\sigma}_f$ associated with the other sources of the errors, denoted as $\boldsymbol{\sigma}_f^{\text{ren.}}$, $\boldsymbol{\sigma}_f^{\text{fac.}}$, and $\boldsymbol{\sigma}_f^{\text{PDF}}$, in a similar manner. Finally, the total values of $\boldsymbol{\sigma}_f$ are obtained by combining all the sources together as[34]

$$\sigma_{f,\alpha} = \sqrt{(\sigma_{f,\alpha}^{\text{lumi.}})^2 + (\sigma_{f,\alpha}^{\text{ren.}})^2 + (\sigma_{f,\alpha}^{\text{fac.}})^2 + (\sigma_{f,\alpha}^{\text{PDF}})^2}. \tag{5.11}$$

In Tables 14 and 15, we show the values of $\boldsymbol{\sigma}_{ee}$ and $\boldsymbol{\sigma}_{e\nu_e}$ associated with each source of the systematic errors, respectively. These values can be interpreted as the possible size of the fit parameters within the SM, which is caused by the systematic uncertainties. As explained in Eq. (5.11), we combine these values in each column to obtain $\boldsymbol{\sigma}_f$. In Table 16, we summarize the result of the combination for all the final states. The values of $\boldsymbol{\sigma}_f$ are

---

[34]There may be some correlations between the distribution of nuisance parameters $\boldsymbol{\theta}_f$. In this section, we treat each of them as obeying to an independent Gaussian distribution for simplicity.

Final state f	$\sigma_{f,1}$	$\sigma_{f,2}$	$\sigma_{f,3}$	$\sigma_{f,4}$	$\sigma_{f,5}$
ee	0.7	1.0	0.4	0.09	0.008
$\mu\mu$	0.7	1.0	0.4	0.09	0.008
$e\nu_e$	1.2	1.9	0.7	0.2	0.01
$\mu\nu_\mu$	1.2	1.9	0.7	0.2	0.01

Table 16: Summary of standard deviations $\boldsymbol{\sigma}_f$ for each final state.

independent of the final state lepton flavors since the energy scale of our concern is much higher than the lepton masses. However, we use different sets of fit parameters $\boldsymbol{\theta}_{ee}$ and $\boldsymbol{\theta}_{\mu\mu}$ for the NC processes and $\boldsymbol{\theta}_{e\nu_e}$ and $\boldsymbol{\theta}_{\mu\nu_\mu}$ for the CC processes because of the different detector response to electrons and muons.

Several comments on other possible sources of systematic errors are in order. As for the beam energy error, we could not generate events at NLO due to the lack of sufficient computational power. Instead, we checked at LO that the corresponding values of $\boldsymbol{\sigma}$ (assuming that the uncertainty of the beam energy is $1\,\%$) are small enough, and hence we simply ignored it. Two of the remaining sources are the pile-up effect and the underlying event, but they may be thought of as negligible since we are focusing on the very clean signal of two energetic leptons. Another one is the effect of higher order corrections to the cross section and that of background processes which are not considered in our analysis. It is in principle possible to estimate their effects through the simulation and improve the analysis but here we just leave it as a future task. Related to this, we note here that a smooth change of the number of events in general, possibly including the uncertainty listed above, could be absorbed by a minimization procedure using some fitting function like in Eq. (5.3). On the other hand, as we will discuss below, the WIMP signal can not be fully absorbed by the fit because of the sharp bend we mentioned before.

We have also neglected the systematic errors from the detector effect. The main errors are expected to come from the lepton identification, in which some of the leptons in any process are overlooked or identified incorrectly, resulting in the mis-reconstruction of the event topology. Again, it is expected that the small and smooth modification of the number of events may be absorbed into the choice of nuisance parameters, if the corresponding values of $\boldsymbol{\sigma}_f$ are properly taken into account in addition to the values in Tables 14 and 15. What is dangerous is the possible jerky modification that mimics the WIMP signal, which may be induced by the detector setup, the complicated detector response to leptons, and so on. Such unwanted fake signals may be avoided by checking the consistency between the electron and muon channels. This is because there should be the same size signals at the same lepton invariant mass in both channels for the WIMP signal, while the detector response to electrons
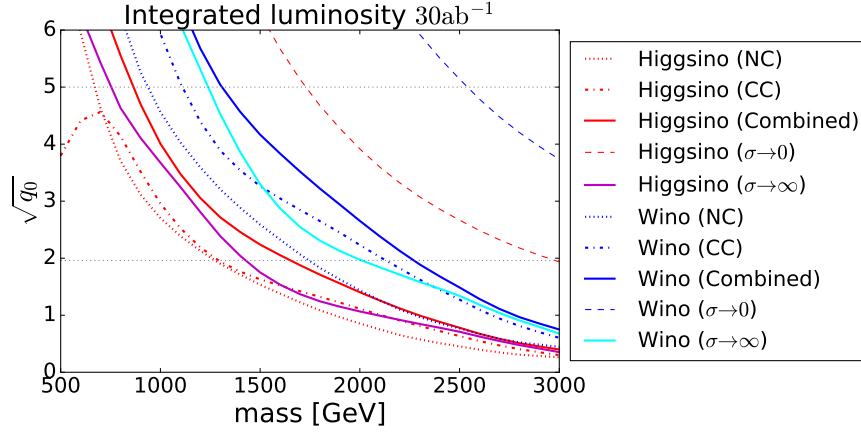
Figure 17: $\sqrt{q_0}$ as a function of the WIMP mass. Red and blue lines correspond to the Higgsino and Wino, respectively, while line styles represent the result from the NC processes, the CC processes, the combined analysis, and the combined analysis with the optimistic $\boldsymbol{\sigma_f \to 0}$ limit. The purple and cyan lines correspond to the results from the conservative analysis with $\boldsymbol{\sigma_f \to \infty}$ for the Higgsino and Wino, respectively. **(♣ Also show a figure for MDM! ♣)**

and muons is different and such a coincidence is not expected in general. It may also be helpful to look for similar fake signals in different processes associated with several leptons. In this section, we just assume that these systematic errors from the detector effect are well controlled once the real experiment will start and focus on the theoretical uncertainties listed in tables.

5.2.3 Detection reach

Now we show the detection reach of WIMPs at future $100\,\mathrm{TeV}$ colliders. In Fig. 17, we plot the value of $\sqrt{q_0}$ as a function of the WIMP mass, with the integrated luminosity $\mathcal{L} = 30\,\mathrm{ab}^{-1}$. As representative scenarios, we show the cases for Higgsino (the red lines) and Wino (the blue lines). The dotted and dash-dotted lines are the result obtained only from the NC processes and the CC processes, respectively. We find that the CC processes are more sensitive to the effect of the WIMPs than the NC processes because of the larger cross section. This result is consistent with Refs. [153, 154]. The sensitivity of the CC processes is weakened for $m \lesssim 700\,\mathrm{GeV}$ because of the lepton p_T cut we have applied.[♮35] The combined

---

[♮35]We note here that the sensitivity of the CC processes depends on the lepton p_T cut. For example, adopting the tighter cut, lepton-$p_T > 1\,\mathrm{TeV}$, the CC processes have almost no sensitivity to WIMPs with $m < 1\,\mathrm{TeV}$. Thus, in particular for the purpose of the Higgsino search, it is important to realize the lepton p_T cut as low as $\sim 500\,\mathrm{GeV}$.
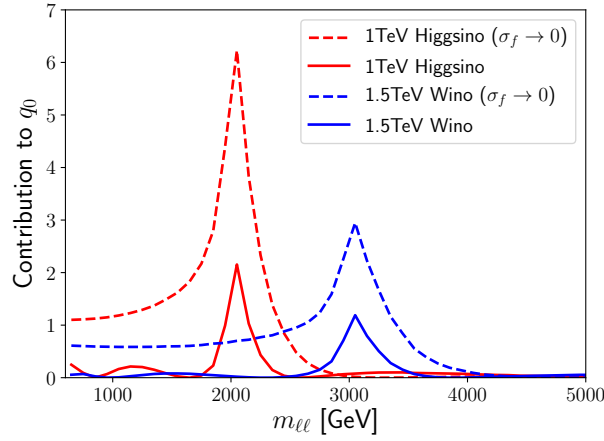
Figure 18:   Plot of the contribution of each bin to the value of q_0 for the NC processes. The red (blue) lines correspond to the 1 TeV Higgsino (1.5 TeV Wino). The solid and dotted lines correspond to the results with the fitting procedure and those without it (*i.e.,* the $\boldsymbol{\sigma}_f \to 0$ limit), respectively.

results of the NC and CC processes are shown by the solid lines. By combining the two types of processes, the 5σ discovery reaches (95 % C.L. bounds) for Higgsino and Wino are 850 GeV (1.7 TeV) and 1.3 TeV (2.3 TeV), respectively. We find that the combination of the NC and CC processes improves the sensitivity of the WIMP mass. Furthermore, if we understand all the systematic uncertainties quite well and effectively take the $\boldsymbol{\sigma}_f \to \boldsymbol{0}$ limit in the combined result, the detection reach will be pushed up significantly as shown by the dashed lines: 1.1 TeV Higgsino signal at well above 5σ level and a 4σ hint of the 2.9 TeV Wino. These lines should be compared with the combined results and also with those obtained from the conservative analysis with $\boldsymbol{\sigma}_f \to \infty$, assuming no knowledge about sources of systematic errors. The plot shows us that it is essential to reduce the systematic uncertainties for the detection of WIMPs through the NC and CC processes.

    We also show the detection reach of the MDM scenario in Fig. **??**. The 5σ reaches are ??? TeV and ??? TeV for 5-plet fermion and 7-plet scalar, while the 95 % reaches are ??? TeV and ??? TeV. They are lowered to ??? TeV and ??? TeV (5σ) and ??? TeV and ??? TeV (95 % C.L.) when the systematic errors are included. If we assume the vanilla thermal freeze-out scenario, the mass should be 10 TeV for 5-plet fermion and 25 TeV for 7-plet scalar [84]. Thus, our method probes only a part of the allowed mass range for these multiplets.   (♣ Fill the values, and 5-plet scalar, maybe? ♣)

    Next, we plot in Fig. 18 the contribution of each bin to the value of q_0 to take a closer look at the significance of the dip structure, focusing on the NC processes as an example. The red (blue) lines correspond to the 1 TeV Higgsino (1.5 TeV Wino), while the solid and

dotted lines correspond to the results with the fitting procedure and those without it (*i.e.,* the $\boldsymbol{\sigma}_f \to 0$ limit), respectively. We can see that the most contributions come from the bins around the peak at $m_{\ell\ell} = 2m$. This feature is clearer for the fitting based approach, where all the smooth parts of the correction are absorbed into the fit parameters, thus there is almost no contribution to q_0 from the bins other than $m_{\ell\ell} \sim 2m$. Note also that, for the $\boldsymbol{\sigma}_f \to 0$ analysis, there are more contributions from the bins with lower $m_{\ell\ell}$ than those with higher $m_{\ell\ell}$, though sometimes the WIMP effect on the cross section is much larger in the latter bins. This is just because of the difference of number of events in each bin, that is $\mathcal{O}(10^7)$ for $500\,\mathrm{GeV} < m_{\ell\ell} < 600\,\mathrm{GeV}$, while $\mathcal{O}(10^3)$ for $4900\,\mathrm{GeV} < m_{\ell\ell} < 5000\,\mathrm{GeV}$ in our set up, for instance. The similar behavior can be expected also for the CC processes.

So far, we have adopted the assumption that the distribution of the nuisance parameters is the Gaussian form and that the fitting function Eq. (5.3) is sufficient for treating systematic errors. In order to discuss the dependence of the results on these assumptions, we have repeated the same analysis using another distribution or fitting function. In the former case, we have adopted the top-hat distribution: the likelihood function for the nuisance parameters L' is given by

$$L'(\boldsymbol{\theta}_f; \boldsymbol{\sigma}_f) \equiv \prod_\alpha \Theta\left(\sqrt{3}\,\sigma_{f,\alpha} - |\theta_{f,\alpha}|\right), \tag{5.12}$$

where Θ is the Heaviside step function. This corresponds to the top-hat distribution of $\theta_{f,\alpha}$ with the variance $\sigma_{f,\alpha}^2$ for each α. As for an example of another fitting function, we have adopted a simple one parameter extension of Eq. (5.3)

$$f_{\mathrm{sys},i}(\boldsymbol{\theta}_f) = e^{\theta_{f,1}}(1 - p_i)^{\theta_{f,2}} p_i^{(\theta_{f,3} + \theta_{f,4}\ln p_i + \theta_{f,5}\ln^2 p_i + \theta_{f,6}\ln^3 p_i)}, \tag{5.13}$$

which consists of six parameters. The variances of the nuisance parameters are estimated in the same way as Sec. 5.2.2, but now with the six parameters.

In Fig. 19, we show the corresponding results for Higgsino and Wino as an example. The convention for the line colors is the same as Fig. 17, while the line styles denote different procedures: the dashed and dotted lines correspond to the result with the top-hat distribution and that with the six parameters fitting function, respectively, while solid lines are the same as Fig. 17. From the figure, we can see that the choice of the distribution may slightly affect the result, while the addition of a nuisance parameter as Eq. (5.13) causes almost no effect. The size of the effect of the choice of the distribution for the current estimation of errors $\boldsymbol{\sigma}_f$ is about $100\,\mathrm{GeV}$ ($200\,\mathrm{GeV}$) for the 5σ ($95\,\%$ C.L.) bounds. We expect that such uncertainties due to the procedure to include the systematic errors will be reduced once the data from the real experiment (and hence better understanding of the systematic errors) will become available.
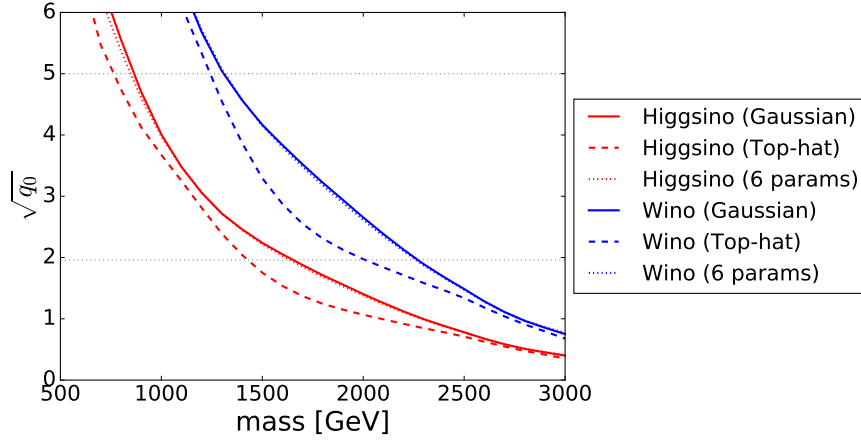
(♣ **Comment on bound state effect somewhere** ♣)

Figure 19: $\sqrt{q_0}$ as a function of the WIMP mass using both the NC and CC processes. The convention for the line colors is the same as Fig. 17. The line styles denote the result same as Fig. 17 (solid), that with the top-hat distribution (dashed), and that with the six parameters fitting function (dotted).

5.2.4   Determination of WIMP properties

In this subsection, we show that it is possible to determine the properties of the WIMPs from the NC and CC processes, thanks to the fact that we can study the $m_{\ell\ell}$ and m_T distribution in great detail for these processes. Some information about the mass, charge, and spin of the WIMPs can be extracted because the corrections to these distributions from the WIMPs are completely determined by these WIMP properties. Firstly, we can extract the WIMP mass from the position of the dip-like structure in the correction since it corresponds to roughly twice the WIMP mass as we have shown in Sec. 5.1. Secondly, the overall size of the correction gives us information about the $SU(2)_L$ and $U(1)_Y$ charges. The CC processes depend only on the $SU(2)_L$ charge, while the NC processes depend both on the $SU(2)_L$ and $U(1)_Y$ charges. Consequently, we can obtain information about the gauge charges of the WIMPs from the NC and CC processes.

We now demonstrate the mass and charge determination of fermionic WIMPs. This is equivalent to the determination of the parameter set (m, C_1, C_2). We generate the data assuming the SM + WIMP model ($\mu = 1$) with some specific values of m, n, Y, and κ, with which we obtain (m, C_1, C_2). We fix $\mu = 1$ for our theoretical model as well, and hence the theoretical predictions of the number of events also depend on these three parameters, $\boldsymbol{x}_f = \boldsymbol{x}_f(m, C_1, C_2)$. We define the likelihood function $L(\tilde{\boldsymbol{x}}_f; \boldsymbol{\theta}_f, m, C_1, C_2)$ in the same form as Eqs. (5.2) and (5.5) with the theoretical prediction $\boldsymbol{x}_f$ now understood as a function of
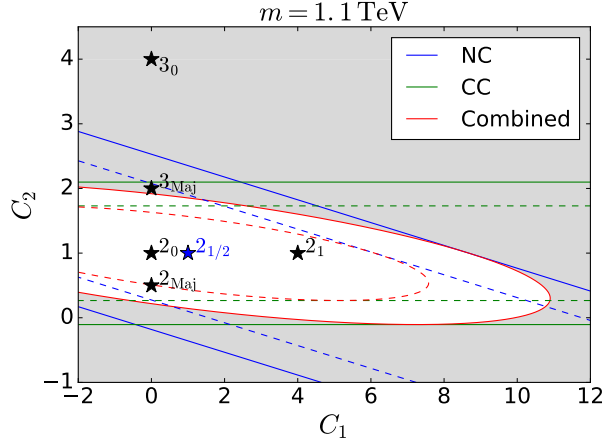
Figure 20:   Contour of $\sqrt{q}$ in the C_1 vs. C_2 plane with $m = 1.1\,\mathrm{TeV}$, where we assume $1.1\,\mathrm{TeV}$ Higgsino signal. The dotted and solid lines denote 1σ and 2σ contours, respectively, and the gray region corresponds to the parameter space that is in tension with the observation at more than 2σ level. The blue, green, and red lines correspond to the result from the NC processes, the CC processes, and the combined analysis, respectively. Each star marker annotated as "n_Y" represents a point corresponding to a $SU(2)_L$ n-plet Dirac fermion with hypercharge Y, while that with "n_{Maj}" corresponds to an $SU(2)_L$ n-plet Majorana fermion.

(m, C_1, C_2), not of μ.[36] The test statistic is defined as

$$q(m, C_1, C_2) \equiv -2 \sum_f \ln \frac{L(\check{\boldsymbol{x}}_f; \hat{\hat{\boldsymbol{\theta}}}_f, m, C_1, C_2)}{L(\check{\boldsymbol{x}}_f; \hat{\boldsymbol{\theta}}_f, \hat{m}, \hat{C}_1, \hat{C}_2)}, \tag{5.14}$$

where the parameters $(\{\hat{\boldsymbol{\theta}}_f\}, \hat{m}, \hat{C}_1, \hat{C}_2)$ maximize $\prod_f L(\check{\boldsymbol{x}}_f; \boldsymbol{\theta}_f, m, C_1, C_2)$, while $\hat{\hat{\boldsymbol{\theta}}}_f$ maximize $L(\check{\boldsymbol{x}}_f; \boldsymbol{\theta}_f, m, C_1, C_2)$ for fixed values of (m, C_1, C_2). It follows the chi-squared distribution with three degrees of freedom in the limit of a large number of events [53]. The test statistic defined in this way examines the compatibility of a given WIMP model (i.e. a parameter set (m, C_1, C_2)) with the observed signal.

Once a deviation from the SM prediction is observed in a real experiment, we may determine (m, C_1, C_2) using the above test statistic q. In the following, we show the expected accuracy of the determination of (m, C_1, C_2) for the case where there exists $1.1\,\mathrm{TeV}$ Higgsino.[37]

---

[36]As shown in Eqs. (5.3) and (5.4), C_1 and C_2 are positive quantities (and C_2 is discrete). In the figures, however, we extend the C_1 and C_2 axes down to negative regions just for presentation purposes.

[37]The expected significance is 3.5σ for $1.1\,\mathrm{TeV}$ Higgsino in our estimation. Even though it is slightly below the 5σ discovery, we take $1.1\,\mathrm{TeV}$ Higgsino as an example because it is a candidate of the thermal relic DM.
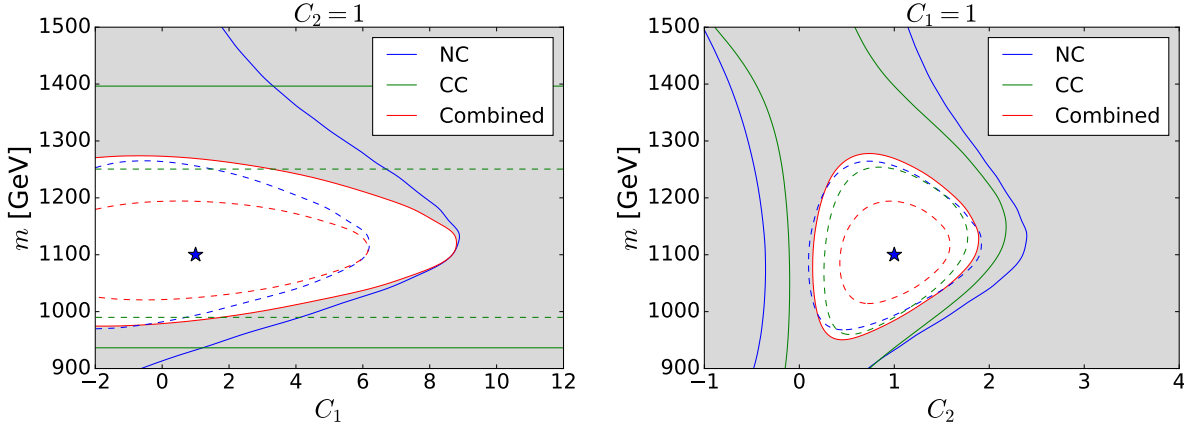
Figure 21:   **Left:** Contour of $\sqrt{q}$ in the C_1 vs. m plane with $C_2 = 1$, where we assume the 1.1 TeV Higgsino signal. The colors and styles of lines and the meaning of the gray region are the same as Fig. 20. The star maker corresponds to the true Higgsino property $(C_1, m) = (1, 1.1\,\text{TeV})$. **Right:** Contour of $\sqrt{q}$ in the C_2 vs. m plane for $C_1 = 1$, where we assume the 1.1 TeV Higgsino signal. The star maker corresponds to the true Higgsino property $(C_2, m) = (1, 1.1\,\text{TeV})$.

In Fig. 20, we show the contours of 1σ (dotted) and 2σ (solid) constraints, which correspond to the values $\sqrt{q} = 1.9$ and $\sqrt{q} = 2.8$, respectively, in the C_1 vs. C_2 plane for $m = 1.1\,\text{TeV}$. The blue, green, and red lines denote the result obtained from the NC processes, the CC processes, and the combined analysis, respectively. The models in the gray region are in more than 2σ tension with the observation. We also show several star markers that correspond to the single $SU(2)_L$ multiplet contributions: the markers with "n_Y" represent an $SU(2)_L$ n-plet Dirac fermion with hypercharge Y, while those with "n_{Maj}" an $SU(2)_L$ n-plet Majorana fermion. Both the NC and CC constraints are represented as straight bands in the C_1 vs. C_2 plane since each process depends on a specific linear combination of C_1 and C_2. In particular, the CC constraint is independent of C_1, or Y. In this sense, the NC and CC processes are complementary to each other, and thus we can separately constrain C_1 and C_2 only after combining these two results. For instance, we can exclude a single fermionic $SU(2)_L$ multiplet with $n \neq 2$ at more than 2σ level, although each process by itself cannot exclude the possibility of 3_{Maj}. We can also constrain the hypercharge, yet it is not uniquely determined. In addition to the Higgsino, the WIMP as an $SU(2)_L$ doublet Dirac fermion with $|Y|^2 \lesssim 2$ or an $SU(2)_L$ doublet Majorana fermion with $|Y|^2 \lesssim 5$ is still allowed.

In Fig. 21, we show the contour plots of $\sqrt{q}$ in the C_1 vs. m plane with $C_2 = 1$ (left) and those in the C_2 vs. m plane with $C_1 = 1$ (right). The star marker in each panel shows the true values of parameters $(C_1, m) = (1, 1.1\,\text{TeV})$ (left) and $(C_2, m) = (1, 1.1\,\text{TeV})$ (right).
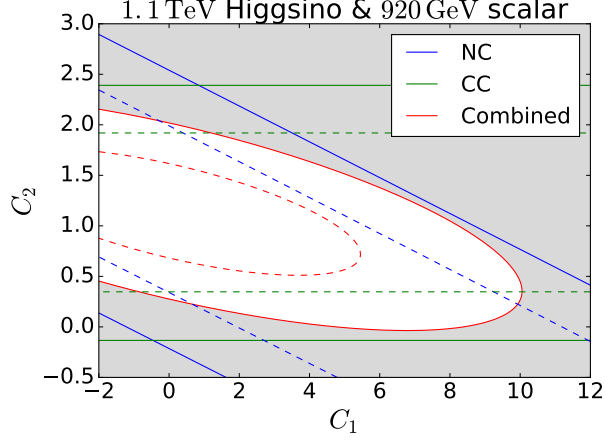
Figure 22:   Contour of $\sqrt{q}$ in the C_1 vs. C_2 plane for the 1.1 TeV Higgsino signal, tested with the scalar WIMP assumption. The plane is defined as the scalar mass of 920 GeV. The colors and styles of lines and the meaning of the gray region are the same as Fig. 20.

Again, by combining the NC and CC results, we can significantly improve the determination of WIMP properties, making 1σ and 2σ contours closed circles in the planes of our concern. In particular, as red lines show, the combined analysis allows us to determine the observed WIMP mass at the level of $\mathcal{O}(10)\%$.

Finally, we comment on the possibility of discriminating between fermionic and scalar WIMPs, whose difference comes from the loop function $f(x)$ (see Eq. (5.2)). Here we repeat the same analysis explained above, assuming the 1.1 TeV Higgsino signal for example, but use the scalar loop function to evaluate the theoretical predictions $\boldsymbol{x}_f(m, C_1, C_2)$. In Figs. 22 and 23, we show the results in the C_1 vs. C_2 plane and the C_1 (or C_2) vs. m plane, respectively, where one of the three parameters is fixed to its best fit value. It is seen that, in the case of the 1.1 TeV Higgsino signal, it is hard to distinguish between the bosonic and fermionic WIMPs only with our method. However, if a part of the WIMP properties (in particular its mass) is determined from another approach, our method may allow us to determine its spin correctly.

We also stress here that, with some favorable assumption about the observed signal, we may obtain some hint about its spin. For example, if we assume that the observed signal composes a fraction of the dark matter in our Universe, the choice of the WIMP charges is significantly constrained. Note from Fig. 22 that the only choices of WIMP charges that allow the WIMP multiplet to contain an electrically neutral component are $(n, |Y|) = (3, 0), (3, 1), (4, 1/2), (4, 3/2)$, and $(5, 0)_{\text{real}}$. The last column of the table 17 shows proper choices of WIMP masses in order for their thermal relic abundances become comparable with the dark matter abundance in the current Universe. All of those values are somewhat
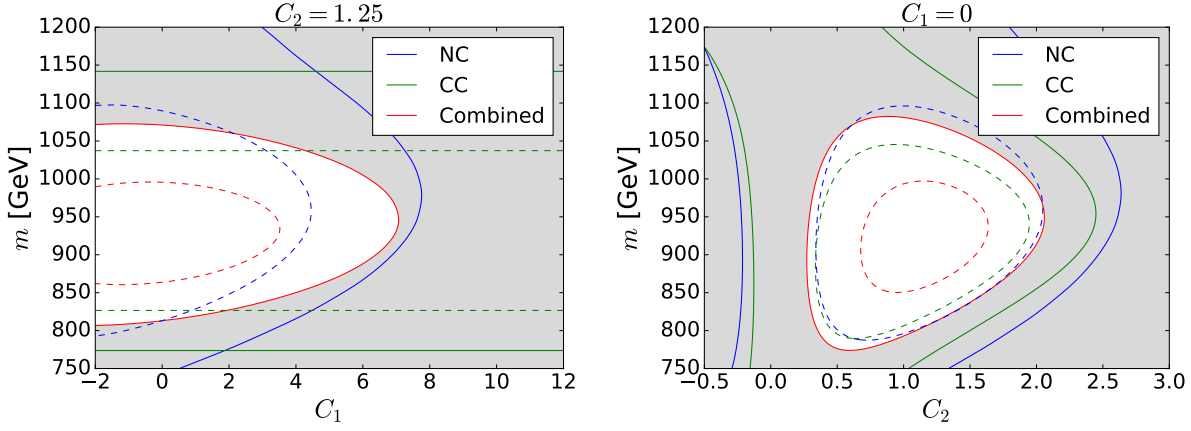
Figure 23:   **Left:** Contour of $\sqrt{q}$ in the C_1 vs. m plane with $C_2 = 1.25$ for the $1.1\,\mathrm{TeV}$ Higgsino signal, tested with the scalar WIMP assumption. The colors and styles of lines and the meaning of the gray region are the same as Fig. 20. **Right:** Contour of $\sqrt{q}$ in the C_2 vs. m plane with $C_1 = 0$ for the $1.1\,\mathrm{TeV}$ Higgsino signal, tested with the scalar WIMP assumption.

(n, Y)	C_1	C_2	$m_{\mathrm{DM}}[\mathrm{TeV}]$
$(3,0)_{\mathrm{real}}$	0	0.25	2.5 [87]
$(3,0)$	0	0.5	1.55 [89]
$(3,1)$	0.75	0.5	1.6 [87]
$(4,\frac{1}{2})$	0.25	1.25	2.4 [87]
$(4,\frac{3}{2})$	2.25	1.25	2.9 [87]
$(5,0)_{\mathrm{real}}$	0	1.25	9.4 [87]

Table 17:   The scalar WIMPs that are compatible with the result in Fig. 22. The observed DM energy density is explained by the thermal relic of the WIMP with m_{DM} shown in the fourth column.

larger than the central value of the mass of the observed signal, which means that the scalar interpretation of the signal cannot explain the whole of the dark matter relic abundance without introducing some non-thermal production mechanism.

5.3   Conclusion

In this section, we have discussed the indirect search of WIMPs at future $100\,\mathrm{TeV}$ hadron colliders based on the precision measurement of the production processes of a charged lepton

pair and that of a charged lepton and a neutrino. In particular, we have demonstrated that not only we can discover the WIMPs, but also we can determine their properties such as their masses, $SU(2)_L$ and $U(1)_Y$ charges, and spins via the processes of our concern. It is based on two facts: the high energy lepton production channel enables us to study its momentum distribution in great detail, and the WIMP correction shows characteristic features, including a dip-like structure as the final state invariant mass being twice the WIMP mass. The latter feature also helps us to distinguish the WIMP signals from backgrounds and systematic errors, as they are not expected to show a dip-like structure. In order to fully exploit the differences between the distributions the WIMP signals and systematic errors, we have adopted the profile likelihood method as our statistical treatment.

First, we have shown in Fig. 17 the detection reach of WIMPs from the NC processes (mediated by photon or Z-boson), the CC processes (mediated by W-boson), and the combination of these two results. We have seen that the addition of the CC processes improves the detection reach from the previous analysis [1]. From the combined analysis, the bounds at the 5σ (95% C.L.) level for Higgsino and Wino are $850\,\text{GeV}$ ($1.7\,\text{TeV}$) and $1.3\,\text{TeV}$ ($2.3\,\text{TeV}$), respectively. We have also shown the $95\,\%$ C.L. reach for 5-plet fermion and 7-plet scalar: ??? TeV and ??? TeV for the optimistic analysis and ??? TeV and ??? TeV for the analysis with a fitting procedure.   (♣ **Fill the values** ♣) This result, in particular that for short lifetime Higgsino, indicates the importance of our method for the WIMP search.

Next, we have considered the determination of the mass and $SU(2)_L$ and $U(1)_Y$ charges of the observed WIMP. By combining the NC and the CC events, the position and the height of the dip in the WIMP effect on the cross section gives us enough information for determining all the three parameters. In Figs. 20 and 21, we have shown the plots of the test statistics that test the validity of several choices of parameters. As a result, the $SU(2)_L$ charge of the observed signal is correctly identified under the assumption of a single WIMP multiplet, and the $U(1)_Y$ charge and mass are also determined precisely. In order for the determination of the WIMP spin, we have plotted the contours of the test statistics that test the validity of the scalar WIMP models with some fixed values of masses and charges. The results are shown in Figs. 22 and 23, which reveals that the spin is not completely determined by solely using our method. Use of another approach to determine the WIMP properties, or of some assumption like that the observed signal corresponds to the dark matter in our Universe, may help us to obtain further information regarding the WIMP spin.

Section 6

Conclusion

(♣ To be written ♣)

Section A

Conventions and notations

In this appendix, we summarize the conventions and notations used throughout the thesis. Firstly, we use the natural units with

$$c = \hbar = k_B = 1, \tag{A.1}$$

where c, $\hbar$, and k_B are the speed of light, the reduced Planck constant, and the Boltzmann constant, respectively.

Our convention of the four-dimensional Lorenzian metric is $g^{\mu\nu} = \mathrm{diag}(1, -1, -1, -1)$. We sometimes use the Pauli matrices defined as

$$\sigma_1 = \begin{pmatrix} 0 & 1 \\ 1 & 0 \end{pmatrix}, \quad \sigma_2 = \begin{pmatrix} 0 & -i \\ i & 0 \end{pmatrix}, \quad \sigma_3 = \begin{pmatrix} 1 & 0 \\ 0 & -1 \end{pmatrix}, \tag{A.2}$$

with i being the imaginary unit. The slash on any character denotes the so-called Feynmann slash, defined as $\slashed{p} \equiv p^\mu \gamma_\mu$ with four-by-four gamma matrices given by

$$\gamma^0 = \begin{pmatrix} \mathbf{0} & \mathbf{1} \\ \mathbf{1} & \mathbf{0} \end{pmatrix}, \quad \gamma^i = \begin{pmatrix} \mathbf{0} & \sigma_i \\ -\sigma_i & \mathbf{0} \end{pmatrix}, \tag{A.3}$$

The unique exception of this rule is $\slashed{E}_T$, which is used to denote the missing transverse momentum in hadron collider experiments.

We use the notation g_1, g_2, and g_3 for the gauge coupling constant of the SM $U(1)_Y$, $SU(2)_L$, and $SU(3)_c$ gauge group. We use the so-called grand unified theory normalization of g_1; the corresponding charge assignment is different from the conventional assignment of $U(1)_Y$ (with, *e.g.*, charge $-1/2$ for the left-handed leptons) by a factor of $\sqrt{3/5}$. We also define and use the fine-structure constants

$$\alpha_1 = \frac{g_1^2}{4\pi}, \quad \alpha_2 = \frac{g_2^2}{4\pi}, \quad \alpha_s = \frac{g_3^2}{4\pi}, \tag{A.4}$$

using the low energy values of gauge coupling constants.

Section B

Review of supersymmetry

(♣ More later ♣)

In this appendix, we briefly review the $\mathcal{N} = 1$ supersymmetry, which is an essential element of the MSSM explained in Sec. **??**. Our argument is based on [56, 160].

The $\mathcal{N} = 1$ supersymmetry is

First example is the MSSM, extension of the SM with the so-called $\mathcal{N} = 1$ supersymmetry (SUSY) [56, 160] that relates a bosonic particle and a fermionic particle. The supersymmetry transformations for a complex scalar ϕ and its "superpartner" Weyl fermion ψ are defined as

$$\delta\phi = (\epsilon\psi), \quad \delta\phi^* = \left(\epsilon^\dagger\psi^\dagger\right), \tag{B.1}$$

$$\delta\psi = -i\left(\sigma^\mu\epsilon^\dagger\right)\partial_\mu\phi, \quad \delta\psi^\dagger = i\left(\epsilon\sigma^\mu\right)\partial_\mu\phi^*, \tag{B.2}$$

where $\sigma^\mu \equiv (\mathbf{1}, \boldsymbol{\sigma})$ with $\boldsymbol{\sigma}$ being Pauli matrices, while ϵ is an anti-commuting Weyl fermionic object that parameterizes the SUSY transformation. The summation over the spinor indices is assumed inside each parenthesis. These transformations, if denoted by operators ϵQ and $\epsilon^\dagger Q^\dagger$, are known to form a closed algebra

$$\left[Q, Q^\dagger\right] = 2i\sigma^\mu\partial_\mu, \tag{B.3}$$

$$\left[Q, Q\right] = \left[Q^\dagger, Q^\dagger\right] = 0, \tag{B.4}$$

when fields are on-shell.[♮38]

    (♣ chiral and vector superfield ♣)
    (♣ $m_f = m_S$ for each multiplet ♣)
    (♣ F-term and D-term potential ♣)

[♮38]In order for the algebra to be closed off-shell, one can introduce a new scalar field F without a kinetic term that is often called as an *auxiliary* field. F works as a Lagrange multiplier whose equation of motion (♣ What? ♣)

Section C

Collider simulation of the MDM model

In this appendix, we explain the procedure we have adopted to implement the MDM model into the numerical calculation performed in Sec. 4. We first make the `FeynRules v2.3` [161] model file for the MDM model by modifying the SM model file $sm.fr$.[♮39] By running `FeynRules`, we can convert the model file to the Universal `FeynRules` Format (UFO) [163], which can be used as a model file for `MadGraph5`.[♮40]

In the Listing 1, we show a part of our `FeynRules` model file `mdm.fr`. This corresponds to the lines that contain additions and modifications to `sm.fr` to take account of the 5-plet fermion as an example of the MDM. . . . denotes a description that is the same as `sm.fr` and thus omitted in the listing.

Listing 1: `mdm.fr`

```
1  (* **************************************** *)
2  (* ***** SU(2)L representation matrix ****** *)
3  (********************************************)
4
5  replaceMDM = {repMDM[a_,b_,c_] :>
6    {{{0,1,0,0,0},{1,0,Sqrt[3/2],0,0},{0,Sqrt[3/2],0,Sqrt[3/2],0},{0,0,
         Sqrt[3/2],0,1},{0,0,0,1,0}},
7    {{0,-I,0,0,0},{I,0,-I Sqrt[3/2],0,0},{0,I Sqrt[3/2],0,-I Sqrt
         [3/2],0},{0,0,I Sqrt[3/2],0,-I},{0,0,0,I,0}},
8    {{2,0,0,0,0},{0,1,0,0,0},{0,0,0,0,0},{0,0,0,-1,0},{0,0,0,0,-2}}}[[a
         [[2]],b[[2]],c[[2]]]]
9  };
10
11 (* ************************** *)
12 (* ****** Gauge groups ****** *)
13 (* ************************** *)
14
15 M$GaugeGroups = {
16   U1Y == {...},
17   SU2L == {
18     Abelian -> False,
19     CouplingConstant -> gw,
20     GaugeBoson -> Wi,
21     StructureConstant -> Eps,
22     Representations -> {{Ta,SU2D},{TM,SU2M}},
```

[♮39]Model files for the SM and several relatively simple extensions of the SM are found in the model database equipped in the official wiki [162].

[♮40]The use of collider physics public codes such as `FeynRules` and `MadGraph5` can be systematically learned by referring the well summarized lecture notes provided by Sho Iwamoto [164].

```
23      Definitions -> {Ta[a_,b_,c_]->PauliSigma[a,b,c]/2, FSU2L[i_,j_,k_]:>
           I Eps[i,j,k], TM[a_,b_,c_]->repMDM[a,b,c]}
24   },
25   SU3C == {...}
26 };
27
28 (* ************************* *)
29 (* ******** Indices ********* *)
30 (* ************************* *)
31
32 IndexRange[Index[SU2W ]] = Unfold[Range[3]];
33 IndexRange[Index[SU2D ]] = Unfold[Range[2]];
34 IndexRange[Index[SU2M ]] = Unfold[Range[5]];
35 IndexRange[Index[Gluon ]] = NoUnfold[Range[8]];
36 IndexRange[Index[Colour ]] = NoUnfold[Range[3]];
37 IndexRange[Index[Generation]] = Range[3];
38
39 IndexStyle[SU2W, j];
40 IndexStyle[SU2D, k];
41 IndexStyle[SU2M, l];
42 IndexStyle[Gluon, a];
43 IndexStyle[Colour, m];
44 IndexStyle[Generation, f];
45
46 (* ************************* *)
47 (* **** Particle classes **** *)
48 (* ************************* *)
49
50 M$ClassesDescription = {
51   ...
52
53 (* Physical MDM Dirac components *)
54   F[5] == {
55     ClassName -> chi0,
56     SelfConjugate -> True,
57     WeylComponents -> chi0w,
58     Mass -> {mMDM0, 1000},
59     Width -> 0,
60     MajoranaPhase -> 0,
61     PropagatorLabel -> "chi0",
62     PropagatorType -> Straight,
63     PropagatorArrow -> None,
64     ParticleName -> "chi0",
65     FullName -> "chi0"
66   },
67   F[6] == {
68     ClassName -> chi1,
69     SelfConjugate -> False,
70     WeylComponents -> {chi1pw, chi1mwbar},
71     Mass -> {mMDM1, 1000},
```

```
72      Width -> 0,
73      MajoranaPhase -> 0,
74      QuantumNumbers -> {Q -> 1},
75      PropagatorLabel -> "chi1",
76      PropagatorType -> Straight,
77      PropagatorArrow -> Forward,
78      ParticleName -> "chi+",
79      AntiParticleName -> "chi-",
80      FullName -> "chi1"
81    },
82    F[7] == {
83      ClassName -> chi2,
84      SelfConjugate -> False,
85      WeylComponents -> {chi2pw, chi2mwbar},
86      Mass -> {mMDM2, 1000},
87      Width -> 0,
88      MajoranaPhase -> 0,
89      QuantumNumbers -> {Q -> 2},
90      PropagatorLabel -> "chi2",
91      PropagatorType -> Straight,
92      PropagatorArrow -> Forward,
93      ParticleName -> "chi++",
94      AntiParticleName -> "chi--",
95      FullName -> "chi2"
96    },
97
98 (* Fermions: unphysical fields *)
99    F[11] == {
100     ClassName -> LL,
101     Unphysical -> True,
102     Indices -> {Index[SU2D], Index[Generation]},
103     FlavorIndex -> SU2D,
104     SelfConjugate -> False,
105     QuantumNumbers -> {Y -> -1/2},
106     Definitions -> { LL[sp1_,1,ff_] :> Module[{sp2}, ProjM[sp1,sp2] vl[
          sp2,ff]], LL[sp1_,2,ff_] :> Module[{sp2}, ProjM[sp1,sp2] l[sp2,ff
          ]] }
107   },
108   F[12] == {
109     ClassName -> lR,
110     Unphysical -> True,
111     Indices -> {Index[Generation]},
112     FlavorIndex -> Generation,
113     SelfConjugate -> False,
114     QuantumNumbers -> {Y -> -1},
115     Definitions -> { lR[sp1_,ff_] :> Module[{sp2}, ProjP[sp1,sp2] l[sp2,
          ff]] }
116   },
117   F[13] == {
118     ClassName -> QL,
```

```
119      Unphysical -> True,
120      Indices -> {Index[SU2D], Index[Generation], Index[Colour]},
121      FlavorIndex -> SU2D,
122      SelfConjugate -> False,
123      QuantumNumbers -> {Y -> 1/6},
124      Definitions -> {
125        QL[sp1_,1,ff_,cc_] :> Module[{sp2}, ProjM[sp1,sp2] uq[sp2,ff,cc]],
126        QL[sp1_,2,ff_,cc_] :> Module[{sp2,ff2}, CKM[ff,ff2] ProjM[sp1,sp2]
             dq[sp2,ff2,cc]] }
127      },
128    F[14] == {
129      ClassName -> uR,
130      Unphysical -> True,
131      Indices -> {Index[Generation], Index[Colour]},
132      FlavorIndex -> Generation,
133      SelfConjugate -> False,
134      QuantumNumbers -> {Y -> 2/3},
135      Definitions -> { uR[sp1_,ff_,cc_] :> Module[{sp2}, ProjP[sp1,sp2] uq[
             sp2,ff,cc]] }
136      },
137    F[15] == {
138      ClassName -> dR,
139      Unphysical -> True,
140      Indices -> {Index[Generation], Index[Colour]},
141      FlavorIndex -> Generation,
142      SelfConjugate -> False,
143      QuantumNumbers -> {Y -> -1/3},
144      Definitions -> { dR[sp1_,ff_,cc_] :> Module[{sp2}, ProjP[sp1,sp2] dq[
             sp2,ff,cc]] }
145      },
146
147  (* Unphysical MDM multiplet *)
148    W[1] == {
149      ClassName -> MDM,
150      Unphysical -> True,
151      Chirality -> Left,
152      SelfConjugate -> False,
153      Indices -> {Index[SU2M]},
154      FlavorIndex -> SU2M,
155      Definitions -> {
156        MDM[sp1_,1] -> chi2pw[sp1],
157        MDM[sp1_,2] -> chi1pw[sp1],
158        MDM[sp1_,3] -> chi0w[sp1],
159        MDM[sp1_,4] -> chi1mw[sp1],
160        MDM[sp1_,5] -> chi2mw[sp1] }
161      },
162
163  (* Unphysical MDM Weyl components *)
164    W[2] == {
165      ClassName -> chi0w,
```

```
166      Unphysical -> True,
167      Chirality -> Left,
168      SelfConjugate -> False
169    },
170    W[3] == {
171      ClassName -> chi1pw,
172      Unphysical -> True,
173      Chirality -> Left,
174      SelfConjugate -> False,
175      QuantumNumbers -> {Q -> 1}
176    },
177    W[4] == {
178      ClassName -> chi1mw,
179      Unphysical -> True,
180      Chirality -> Left,
181      SelfConjugate -> False,
182      QuantumNumbers -> {Q -> -1}
183    },
184    W[5] == {
185      ClassName -> chi2pw,
186      Unphysical -> True,
187      Chirality -> Left,
188      SelfConjugate -> False,
189      QuantumNumbers -> {Q -> 2}
190    },
191    W[6] == {
192      ClassName -> chi2mw,
193      Unphysical -> True,
194      Chirality -> Left,
195      SelfConjugate -> False,
196      QuantumNumbers -> {Q -> -2}
197    }
198  };
199
200  (* ************************ *)
201  (* ******* Parameters ******* *)
202  (* ************************ *)
203
204  M$Parameters = {
205    ...
206
207    mmm == {
208      ParameterType -> External,
209      BlockName -> MDMBLOCK,
210      OrderBlock -> 1,
211      Value -> 1000,
212      TeX -> Subscript[m, MDM],
213      Description -> "MDM mass"
214    }
215  };
```

```
216
217  (* ************************* *)
218  (* ******* Lagrangian ******* *)
219  (* ************************* *)
220
221    ...
222
223  LMDM  := Block[{mu},
224    ExpandIndices[I MDMbar.sibar[mu].DC[MDM, mu] - mmm/2 chi0bar.chi0 - mmm
          chi1bar.chi1 - mmm chi2bar.chi2,
225    FlavorExpand->{SU2W,SU2M}]/.replaceMDM//WeylToDirac];
226
227  Lagrangian:= LGauge + LFermions + LMDM + LHiggs + LYukawa + LGhost;
```

Section D

Properties of the transverse mass

In this appendix, we summarize the properties of the transverse mass, which is used for the analysis of the mono-lepton final state in Sec. 5. The transverse mass is useful when there is a unique invisible particle (which we will call I) such as a neutrino in the final state. As already mentioned in Sec. 5.1, the transverse mass m_T is defined event by event using the measured value of the missing transverse momentum $\not{E}_T$ as

$$m_T^2 \equiv 2p_T \, \not{E}_T \, (1 - \cos \phi), \tag{D.1}$$

where p_T denotes the transverse momentum of a visible final state particle (which will call P) and ϕ is the difference between the azimuth angles of visible and missing transverse momenta. It is important that we can infer the invariant mass of particles P and I with m_T, if both P and I are (approximately) massless.

Let p_P and p_I be the four momenta of P and I, respectively. When there is only one invisible particle in the event, the transverse momentum of I is roughly identified with $\not{E}_T$. Hereafter, we assume the exact equality among them just for simplicity, which corresponds to neglect the detector errors, transverse momentum of initial partons, soft emissions that are invisible for detectors, and so on. Then, we can write the components of four momenta as

$$p_P = (E_P, p_T \cos \phi_P, p_T \sin \phi_P, p_{Pz}), \tag{D.2}$$

$$p_I = (E_I, \not{E}_T \cos \phi_I, \not{E}_T \sin \phi_I, p_{Iz}), \tag{D.3}$$

with $\phi \equiv \phi_P - \phi_I$. Note that massless conditions are satisfied, namely $E_P^2 = p_T^2 + p_{Pz}^2$ and $E_I^2 = \not{E}_T^2 + p_{Iz}^2$. We can derive a relation between m_T and $m_{PI} \equiv \sqrt{(p_P + p_I)^2}$

$$m_T \leq m_{PI}, \tag{D.4}$$

where the equation holds when

$$p_{Pz} \not{E}_T - p_T p_{Iz} = 0. \tag{D.5}$$

When the above equation roughly holds, $m_{PI} - m_T$ is proportional to $(p_{Pz} \not{E}_T - p_T p_{Iz})^2$.

It is more intuitive to understand the situation in the center-of-mass system (CMS), focusing on the pair production process of particles P and I. In this case, the transverse momentum of the event is simply given by

$$m_T^{(\mathrm{CMS})} = m_{PI} \sin \theta^{(\mathrm{CMS})}, \tag{D.6}$$
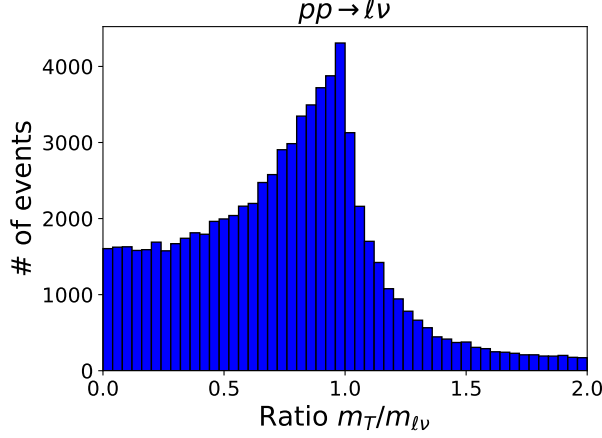
Figure 24:　Distribution of $m_T/m_{\ell\nu}$ for the pair production process of $P = \ell$ and $I = \nu$. Figure for $\sqrt{s} = 100\,\mathrm{TeV}$ and $\mathcal{L} = 1\,\mathrm{ab}^{-1}$.

where $\theta^{(\mathrm{CMS})}$ is the angle between the momentum of P and the beamline in the CMS. Although the definition of m_T is not Lorentz invariant and generally $m_T^{(\mathrm{CMS})} \neq m_T$, the former gives a good approximation of the latter when the two-particle system is not highly boosted. Let us simply assume $m_T = m_T^{(\mathrm{CMS})}$ and consider the repeated production of P and I with fixed m_{PI}. When we postulate the uniform distribution of the production cross section against $\cos\theta^{(\mathrm{CMS})}$ for simplicity, the distribution of the transverse mass $f(m_T)$ calculated according to Eq. (D.6) possesses a sharp peak at $m_T = m_{PI}$, described by

$$f(m_T) = \frac{m_T}{m_{PI}} \cos^{-1}\left[\arcsin\left(\frac{m_T}{m_{PI}}\right)\right]. \tag{D.7}$$

This peak, often called the Jacobian peak, enables us to estimate m_{PI} from the distribution of m_T.

In Fig. 24, we show the distribution of the ratio $m_T/m_{\ell\nu}$ for the pair production process of $P = \ell$ and $I = \nu$. We use the setup of $\sqrt{s} = 100\,\mathrm{TeV}$ and $\mathcal{L} = 1\,\mathrm{ab}^{-1}$. To evaluate the missing transverse momentum $\not{E}_T$ for each event, we have performed the detector simulation using Delphes similar to the analysis in Sec. 5. We can clearly see the peak at $m_T/m_{\ell\nu} = 1$, though it is somewhat smeared compared with Eq. (D.7) due to the effect of the Lorentz boost and the non-trivial angular dependence of the production cross section. Besides, the small tail of the distribution for $m_T > m_{\ell\nu}$ can be understood as the effects we have neglected so far, such as the detector errors.

Section E

Profile likelihood method

In this appendix, we briefly review the profile likelihood method used in Sec. 5.2.2. In particular, we describe the motivation and justification to consider this method.

First of all, the experimental outcome can be expressed as a set of random variables $\boldsymbol{x} \equiv \{x_1, \cdots, x_n\}$, with n being the number of observables. The distribution of these variables is due to both the intrinsic physical randomness (*i.e.*, the statistical fluctuation) and the uncertainty in detector responses such as the efficiency, momentum reconstruction, and so on. We assume $\boldsymbol{x}$ obey some probability distribution function and express it as $f(\boldsymbol{x}; \boldsymbol{\theta})$, where $\boldsymbol{\theta} = \{\theta_1, \cdots, \theta_m\}$ parametrize (in many cases unknown) uncertainties listed above. When we repeat N experiments and obtain N sets of observables expressed as $\boldsymbol{x}^a$ ($a = 1, \cdots, N$), we define the likelihood function L as

$$L = \prod_{a=1}^{N} f(\boldsymbol{x}^a; \boldsymbol{\theta}). \tag{E.1}$$

Since L should take a relatively larger value if the assumed distribution f approximates the reality very well, we may perform the maximization of L against the choice of $\boldsymbol{\theta}$ to obtain the correct probability distribution. Such a maximization procedure can be performed analytically only for several simple distribution functions. Thus, in many cases, we need a numerical calculation of the maximization procedure, which can be performed with the `MINUIT` package [165].

In our analysis in Sec. 5, the data is given in the form of the histogram. In this case, x_i ($i = 1, \cdots, n$) denotes the observed number of events in each bin labeled by i, with n being the number of bins. Then the likelihood L, which is the product of the probability distribution function for each bin, is expressed as

$$L(\boldsymbol{x}; \boldsymbol{\theta}) \equiv \prod_{i} f_i(\boldsymbol{x}; \boldsymbol{\theta}) = \prod_{i} \exp\left[-\frac{(x_i - \mu_i(\boldsymbol{\theta}))^2}{2x_i} \right], \tag{E.2}$$

with $\mu_i(\boldsymbol{\theta})$ being the average number of events of the bin i calculated using the parameters $\boldsymbol{\theta}$. Note that $x_i \gg 1$ is assumed for each bin and the central limit theorem is used to replace the Poisson to the Gaussian distribution. Then, it is clear that the maximization of L is equivalent to the minimization of χ^2 defined as

$$\chi^2 \equiv -2 \ln L(\boldsymbol{x}; \boldsymbol{\theta}) = \sum_{i=1}^{n} \frac{(x_i - \mu_i(\boldsymbol{\theta}))^2}{x_i}, \tag{E.3}$$

which is the so-called Neyman's χ^2 variable. χ^2 obeys the chi-squared distribution when the distribution of x_i is well approximated by the Gaussian and can be easily used to estimate the errors of $\boldsymbol{\theta}$ around the optimized values.

Similarly, one can apply the likelihood maximization to the model test. Let $\boldsymbol{\theta}_{\mathrm{true}}$ and $\boldsymbol{\theta}_{\mathrm{test}}$ be the model in reality and that we want to test, respectively. For example, in the new physics search, the former corresponds to a new physics model of our concern, while the latter to the SM. Then we can define the test-statistic

$$q(\boldsymbol{\theta}_{\mathrm{test}}) = -2\ln \frac{L(\boldsymbol{x}; \boldsymbol{\theta}_{\mathrm{test}})}{L(\boldsymbol{x}; \boldsymbol{\theta}_{\mathrm{true}})}, \tag{E.4}$$

which plays the role of the so-called $\Delta\chi^2$ variable according to the discussion above. Again q may obey a chi-squared distribution with some degrees of freedom, and can be used to obtain sensitivities to the new physics, *e.g.,* the $95\,\%$ C.L. exclusion and the 5σ discovery. Note that the denominator of the test statistic can also be expressed as $L(\boldsymbol{x}; \hat{\boldsymbol{\theta}})$, where the hat denotes the values of $\boldsymbol{\theta}$ that maximize the function L.

However, the situation may be more complicated since some of the parameters $\boldsymbol{\theta}$ are not directly related to the model parameters, but express the background yield, detector effects, systematic errors, and so on, which should be determined from experimental data. Such additional parameters are often called nuisance parameters. To treat nuisance parameters, it is convenient to rely on the profile likelihood method [158].

For this purpose, we divide the parameters into two categories: the model parameter of our interest $\boldsymbol{\mu}$ and nuisance parameters $\boldsymbol{\theta}$. Similarly to the discussion without the nuisance parameters, let $\boldsymbol{\mu}$ be the model that we want to test. The test static is defined as

$$q(\boldsymbol{\mu}) = -2\ln \frac{L(\boldsymbol{x}; \boldsymbol{\mu}, \hat{\hat{\boldsymbol{\theta}}}(\boldsymbol{\mu}))}{L(\boldsymbol{x}; \hat{\boldsymbol{\mu}}, \hat{\boldsymbol{\theta}})}, \tag{E.5}$$

where the meaning of the hat is the same as above, while $\hat{\hat{\boldsymbol{\theta}}}(\boldsymbol{\mu})$ denotes the values that maximize L with fixed values of $\boldsymbol{\mu}$. The motivation for this definition is provided by the Wilk's theorem [166], which proves that $q(\boldsymbol{\mu})$ asymptotically obeys the chi-squared distribution whose degrees of freedom equal to the number of model parameters $\boldsymbol{\mu}$. Note that this statement is highly non-trivial since the individual term $-2\ln L$ *does not* obey a chi-squared distribution in this case. Thanks to the theorem, we can perform the same analysis under the existence of nuisance parameters and, in particular, absorb the effects of systematic errors into the choice of parameters $\boldsymbol{\theta}$.

(♣ Clarify d.o.f ♣)
(♣ Comment on distribution of nuisance parameters? ♣)

References

[1] S. Chigusa, Y. Ema, T. Moroi, Probing electroweakly interacting massive particles with Drell-Yan process at 100 TeV hadron colliders, Phys. Lett. B789 (2019) 106–113. arXiv:1810.07349, doi:10.1016/j.physletb.2018.12.011.

[2] T. Abe, S. Chigusa, Y. Ema, T. Moroi, Indirect studies of electroweakly interacting particles at 100 TeV hadron colliders, Phys. Rev. D100 (5) (2019) 055018. arXiv:1904.11162, doi:10.1103/PhysRevD.100.055018.

[3] R. Kitano, Y. Nomura, A Solution to the supersymmetric fine-tuning problem within the MSSM, Phys. Lett. B631 (2005) 58–67. arXiv:hep-ph/0509039, doi:10.1016/j.physletb.2005.10.003.

[4] C. Brust, A. Katz, S. Lawrence, R. Sundrum, SUSY, the Third Generation and the LHC, JHEP 03 (2012) 103. arXiv:1110.6670, doi:10.1007/JHEP03(2012)103.

[5] M. Papucci, J. T. Ruderman, A. Weiler, Natural SUSY Endures, JHEP 09 (2012) 035. arXiv:1110.6926, doi:10.1007/JHEP09(2012)035.

[6] H. Baer, V. Barger, P. Huang, X. Tata, Natural Supersymmetry: LHC, dark matter and ILC searches, JHEP 05 (2012) 109. arXiv:1203.5539, doi:10.1007/JHEP05(2012)109.

[7] J. D. Wells, Implications of supersymmetry breaking with a little hierarchy between gauginos and scalars, in: 11th International Conference on Supersymmetry and the Unification of Fundamental Interactions (SUSY 2003) Tucson, Arizona, June 5-10, 2003, 2003. arXiv:hep-ph/0306127.

[8] J. D. Wells, PeV-scale supersymmetry, Phys. Rev. D71 (2005) 015013. arXiv:hep-ph/0411041, doi:10.1103/PhysRevD.71.015013.

[9] N. Arkani-Hamed, S. Dimopoulos, Supersymmetric unification without low energy supersymmetry and signatures for fine-tuning at the LHC, JHEP 06 (2005) 073. arXiv:hep-th/0405159, doi:10.1088/1126-6708/2005/06/073.

[10] G. F. Giudice, A. Romanino, Split supersymmetry, Nucl. Phys. B699 (2004) 65–89, [Erratum: Nucl. Phys.B706,487(2005)]. arXiv:hep-ph/0406088, doi:10.1016/j.nuclphysb.2004.11.048,10.1016/j.nuclphysb.2004.08.001.

[11] N. Arkani-Hamed, S. Dimopoulos, G. F. Giudice, A. Romanino, Aspects of split supersymmetry, Nucl. Phys. B709 (2005) 3–46. arXiv:hep-ph/0409232, doi:10.1016/j.nuclphysb.2004.12.026.

[12] N. Arkani-Hamed, S. Dimopoulos, S. Kachru, Predictive landscapes and new physics at a TeV (2005). arXiv:hep-th/0501082.

[13] L. Randall, R. Sundrum, Out of this world supersymmetry breaking, Nucl. Phys. B557 (1999) 79–118. arXiv:hep-th/9810155, doi:10.1016/S0550-3213(99)00359-4.

[14] G. F. Giudice, M. A. Luty, H. Murayama, R. Rattazzi, Gaugino mass without singlets, JHEP 12 (1998) 027. arXiv:hep-ph/9810442, doi:10.1088/1126-6708/1998/12/027.

[15] D. S. Akerib, et al., Results from a search for dark matter in the complete LUX exposure, Phys. Rev. Lett. 118 (2) (2017) 021303. arXiv:1608.07648, doi:10.1103/PhysRevLett.118.021303.

[16] X. Cui, et al., Dark Matter Results From 54-Ton-Day Exposure of PandaX-II Experiment, Phys. Rev. Lett. 119 (18) (2017) 181302. arXiv:1708.06917, doi:10.1103/PhysRevLett.119.181302.

[17] E. Aprile, et al., Dark Matter Search Results from a One Tonne×Year Exposure of XENON1T, Phys. Rev. Lett. 121 (11) (2018) 111302. arXiv:1805.12562, doi:10.1103/PhysRevLett.121.111302.

[18] J. Hisano, K. Ishiwata, N. Nagata, A complete calculation for direct detection of Wino dark matter, Phys. Lett. B690 (2010) 311–315. arXiv:1004.4090, doi:10.1016/j.physletb.2010.05.047.

[19] J. Hisano, K. Ishiwata, N. Nagata, Direct Search of Dark Matter in High-Scale Supersymmetry, Phys. Rev. D87 (2013) 035020. arXiv:1210.5985, doi:10.1103/PhysRevD.87.035020.

[20] J. Hisano, K. Ishiwata, N. Nagata, QCD Effects on Direct Detection of Wino Dark Matter, JHEP 06 (2015) 097. arXiv:1504.00915, doi:10.1007/JHEP06(2015)097.

[21] R. J. Hill, M. P. Solon, Universal behavior in the scattering of heavy, weakly interacting dark matter on nuclear targets, Phys. Lett. B707 (2012) 539–545. arXiv:1111.0016, doi:10.1016/j.physletb.2012.01.013.

[22] R. J. Hill, M. P. Solon, WIMP-nucleon scattering with heavy WIMP effective theory, Phys. Rev. Lett. 112 (2014) 211602. arXiv:1309.4092, doi:10.1103/PhysRevLett.112.211602.

[23] J. Hisano, K. Ishiwata, N. Nagata, T. Takesako, Direct Detection of Electroweak-Interacting Dark Matter, JHEP 07 (2011) 005. `arXiv:1104.0228`, `doi:10.1007/JHEP07(2011)005`.

[24] A. Albert, et al., Searching for Dark Matter Annihilation in Recently Discovered Milky Way Satellites with Fermi-LAT, Astrophys. J. 834 (2) (2017) 110. `arXiv:1611.03184`, `doi:10.3847/1538-4357/834/2/110`.

[25] M. L. Ahnen, et al., Limits to Dark Matter Annihilation Cross-Section from a Combined Analysis of MAGIC and Fermi-LAT Observations of Dwarf Satellite Galaxies, JCAP 1602 (02) (2016) 039. `arXiv:1601.06590`, `doi:10.1088/1475-7516/2016/02/039`.

[26] H. Abdallah, et al., Search for dark matter annihilations towards the inner Galactic halo from 10 years of observations with H.E.S.S, Phys. Rev. Lett. 117 (11) (2016) 111301. `arXiv:1607.08142`, `doi:10.1103/PhysRevLett.117.111301`.

[27] G. A. Gómez-Vargas, M. A. Sánchez-Conde, J.-H. Huh, M. Peiró, F. Prada, A. Morselli, A. Klypin, D. G. Cerdeño, Y. Mambrini, C. Muñoz, Constraints on WIMP annihilation for contracted dark matterin the inner Galaxy with the Fermi-LAT, JCAP 1310 (2013) 029. `arXiv:1308.3515`, `doi:10.1088/1475-7516/2013/10/029`.

[28] B. Bhattacherjee, M. Ibe, K. Ichikawa, S. Matsumoto, K. Nishiyama, Wino Dark Matter and Future dSph Observations, JHEP 07 (2014) 080. `arXiv:1405.4914`, `doi:10.1007/JHEP07(2014)080`.

[29] R. Krall, M. Reece, Last Electroweak WIMP Standing: Pseudo-Dirac Higgsino Status and Compact Stars as Future Probes, Chin. Phys. C42 (4) (2018) 043105. `arXiv:1705.04843`, `doi:10.1088/1674-1137/42/4/043105`.

[30] H. Abdalla, et al., Searches for gamma-ray lines and 'pure WIMP' spectra from Dark Matter annihilations in dwarf galaxies with H.E.S.S, JCAP 1811 (11) (2018) 037. `arXiv:1810.00995`, `doi:10.1088/1475-7516/2018/11/037`.

[31] M. Aaboud, et al., Search for long-lived charginos based on a disappearing-track signature in pp collisions at $\sqrt{s}$ = 13 TeV with the ATLAS detector, JHEP 06 (2018) 022. `arXiv:1712.02118`, `doi:10.1007/JHEP06(2018)022`.

[32] Search for direct pair production of higgsinos by the reinterpretation of the disappearing track analysis with 36.1 fb^{-1} of $\sqrt{s}$ = 13 TeV data collected with the ATLAS experiment, Tech. Rep. ATL-PHYS-PUB-2017-019, CERN, Geneva (Dec 2017). URL `http://cds.cern.ch/record/2297480`

[33] A. M. Sirunyan, et al., Search for disappearing tracks as a signature of new long-lived particles in proton-proton collisions at $\sqrt{s} = 13$ TeV, JHEP 08 (2018) 016. arXiv:1804.07321, doi:10.1007/JHEP08(2018)016.

[34] B. Ostdiek, Constraining the minimal dark matter fiveplet with LHC searches, Phys. Rev. D92 (2015) 055008. arXiv:1506.03445, doi:10.1103/PhysRevD.92.055008.

[35] H. Baer, A. Mustafayev, X. Tata, Monojets and mono-photons from light higgsino pair production at LHC14, Phys. Rev. D89 (5) (2014) 055007. arXiv:1401.1162, doi:10.1103/PhysRevD.89.055007.

[36] D. S. M. Alves, J. Galloway, J. T. Ruderman, J. R. Walsh, Running Electroweak Couplings as a Probe of New Physics, JHEP 02 (2015) 007. arXiv:1410.6810, doi:10.1007/JHEP02(2015)007.

[37] C. Gross, O. Lebedev, J. M. No, Drell-Yan constraints on new electroweak states: LHC as a $pp \to l^+l^-$ precision machine, Mod. Phys. Lett. A32 (16) (2017) 1750094. arXiv:1602.03877, doi:10.1142/S0217732317500948.

[38] M. Farina, G. Panico, D. Pappadopulo, J. T. Ruderman, R. Torre, A. Wulzer, Energy helps accuracy: electroweak precision tests at hadron colliders, Phys. Lett. B772 (2017) 210–215. arXiv:1609.08157, doi:10.1016/j.physletb.2017.06.043.

[39] K. Harigaya, K. Ichikawa, A. Kundu, S. Matsumoto, S. Shirai, Indirect Probe of Electroweak-Interacting Particles at Future Lepton Colliders, JHEP 09 (2015) 105. arXiv:1504.03402, doi:10.1007/JHEP09(2015)105.

[40] S. Matsumoto, S. Shirai, M. Takeuchi, Indirect Probe of Electroweakly Interacting Particles at the High-Luminosity Large Hadron Collider, JHEP 06 (2018) 049. arXiv:1711.05449, doi:10.1007/JHEP06(2018)049.

[41] M. L. Mangano, et al., Physics at a 100 TeV pp Collider: Standard Model Processes, CERN Yellow Report (3) (2017) 1–254. arXiv:1607.01831, doi:10.23731/CYRM-2017-003.1.

[42] R. Contino, et al., Physics at a 100 TeV pp collider: Higgs and EW symmetry breaking studies, CERN Yellow Report (3) (2017) 255–440. arXiv:1606.09408, doi:10.23731/CYRM-2017-003.255.

[43] T. Golling, et al., Physics at a 100 TeV pp collider: beyond the Standard Model phenomena, CERN Yellow Report (3) (2017) 441–634. arXiv:1606.00947, doi:10.23731/CYRM-2017-003.441.

[44] M. Ahmad, et al., CEPC-SPPC Preliminary Conceptual Design Report. 1. Physics and Detector (2015).

[45] C.-S. S. Group, CEPC-SPPC Preliminary Conceptual Design Report. 2. Accelerator (2015).

[46] M. Low, L.-T. Wang, Neutralino dark matter at 14 TeV and 100 TeV, JHEP 08 (2014) 161. arXiv:1404.0682, doi:10.1007/JHEP08(2014)161.

[47] M. Cirelli, F. Sala, M. Taoso, Wino-like Minimal Dark Matter and future colliders, JHEP 10 (2014) 033, [Erratum: JHEP01,041(2015)]. arXiv:1407.7058, doi:10.1007/JHEP10(2014)033,10.1007/JHEP01(2015)041.

[48] T. Han, S. Mukhopadhyay, X. Wang, Electroweak Dark Matter at Future Hadron Colliders, Phys. Rev. D98 (3) (2018) 035026. arXiv:1805.00015, doi:10.1103/PhysRevD.98.035026.

[49] R. Mahbubani, P. Schwaller, J. Zurita, Closing the window for compressed Dark Sectors with disappearing charged tracks, JHEP 06 (2017) 119, [Erratum: JHEP10,061(2017)]. arXiv:1703.05327, doi:10.1007/JHEP06(2017)119,10.1007/JHEP10(2017)061.

[50] S. Weinberg, Implications of Dynamical Symmetry Breaking, Phys. Rev. D13 (1976) 974–996, [Addendum: Phys. Rev.D19,1277(1979)]. doi:10.1103/PhysRevD.19.1277,10.1103/PhysRevD.13.974.

[51] E. Gildener, Gauge Symmetry Hierarchies, Phys. Rev. D14 (1976) 1667. doi:10.1103/PhysRevD.14.1667.

[52] L. Susskind, Dynamics of Spontaneous Symmetry Breaking in the Weinberg-Salam Theory, Phys. Rev. D20 (1979) 2619–2625. doi:10.1103/PhysRevD.20.2619.

[53] M. Tanabashi, et al., Review of Particle Physics, Phys. Rev. D98 (3) (2018) 030001. doi:10.1103/PhysRevD.98.030001.

[54] A. Salam, J. A. Strathdee, On Superfields and Fermi-Bose Symmetry, Phys. Rev. D11 (1975) 1521–1535. doi:10.1103/PhysRevD.11.1521.

[55] M. T. Grisaru, W. Siegel, M. Rocek, Improved Methods for Supergraphs, Nucl. Phys. B159 (1979) 429. doi:10.1016/0550-3213(79)90344-4.

[56] S. P. Martin, A Supersymmetry primer (1997) 1–98[Adv. Ser. Direct. High Energy Phys.18,1(1998)]. arXiv:hep-ph/9709356, doi:10.1142/9789812839657_0001,10.1142/9789814307505_0001.

[57] N. Sakai, T. Yanagida, Proton Decay in a Class of Supersymmetric Grand Unified Models, Nucl. Phys. B197 (1982) 533. `doi:10.1016/0550-3213(82)90457-6`.

[58] G. R. Farrar, P. Fayet, Phenomenology of the Production, Decay, and Detection of New Hadronic States Associated with Supersymmetry, Phys. Lett. 76B (1978) 575–579. `doi:10.1016/0370-2693(78)90858-4`.

[59] S. Dimopoulos, H. Georgi, Softly Broken Supersymmetry and SU(5), Nucl. Phys. B193 (1981) 150–162. `doi:10.1016/0550-3213(81)90522-8`.

[60] S. Weinberg, Supersymmetry at Ordinary Energies. 1. Masses and Conservation Laws, Phys. Rev. D26 (1982) 287. `doi:10.1103/PhysRevD.26.287`.

[61] S. Dimopoulos, S. Raby, F. Wilczek, Supersymmetry and the Scale of Unification, Phys. Rev. D24 (1981) 1681–1683. `doi:10.1103/PhysRevD.24.1681`.

[62] L. O'Raifeartaigh, Spontaneous Symmetry Breaking for Chiral Scalar Superfields, Nucl. Phys. B96 (1975) 331–352. `doi:10.1016/0550-3213(75)90585-4`.

[63] P. Fayet, J. Iliopoulos, Spontaneously Broken Supergauge Symmetries and Goldstone Spinors, Phys. Lett. 51B (1974) 461–464. `doi:10.1016/0370-2693(74)90310-4`.

[64] P. Fayet, Supergauge Invariant Extension of the Higgs Mechanism and a Model for the electron and Its Neutrino, Nucl. Phys. B90 (1975) 104–124. `doi:10.1016/0550-3213(75)90636-7`.

[65] T. E. W. Group, 2012 Update of the Combination of CDF and D0 Results for the Mass of the W Boson (2012). `arXiv:1204.0042`.

[66] J. Alcaraz, P. Azzurri, A. Bajo-Vaquero, E. Barberio, A. Blondel, D. Bourilkov, P. Checchia, R. Chierici, R. Clare, J. D'Hondt, G. Della Ricca, M. Dierckxsens, D. Duchesneau, G. Duckeck, M. Elsing, M. W. Grünewald, A. Gurtu, J. B. Hansen, R. Hawkings, S. Jezequel, R. W. L. Jones, T. Kawamoto, E. Lançon, W. Liebig, L. Malgeri, S. Mele, M. N. Minard, K. Mönig, C. Parkes, U. Parzefall, B. Pietrzyk, G. Quast, P. B. Renton, S. Riemann, K. Sachs, D. Strom, A. Strässner, R. Tenchini, F. Teubert, M. A. Thomson, S. Todorova-Nová, A. Valassi, A. Venturi, H. Voss, C. P. Ward, N. K. Watson, P. S. Wells, S. Wynhoff, P. de Jong, B. de la Cruz, A Combination of Preliminary Electroweak Measurements and Constraints on the Standard Model, 2006, Tech. Rep. hep-ex/0612034. ALEPH-2006-001 PHYSICS-2006-001. CERN-L3-310. CERN-PH-EP-2006-042. DELPHI-2006-014 PHYS-948. L3-Note-2833. LEPEWWG-2006-01. OPAL-PR-419, CERN, Geneva, preprint not submitted to publication (Dec 2006). URL `https://cds.cern.ch/record/1016509`

[67] J. Beringer, et al., Review of Particle Physics (RPP), Phys. Rev. D86 (2012) 010001. doi:10.1103/PhysRevD.86.010001.

[68] G. Aad, et al., Measurements of Higgs boson production and couplings in diboson final states with the ATLAS detector at the LHC, Phys. Lett. B726 (2013) 88–119, [Erratum: Phys. Lett.B734,406(2014)]. arXiv:1307.1427, doi:10.1016/j.physletb.2014.05.011,10.1016/j.physletb.2013.08.010.

[69] S. Chatrchyan, et al., Measurement of the properties of a Higgs boson in the four-lepton final state, Phys. Rev. D89 (9) (2014) 092007. arXiv:1312.5353, doi:10.1103/PhysRevD.89.092007.

[70] First combination of Tevatron and LHC measurements of the top-quark mass (2014). arXiv:1403.4427.

[71] V. Tishchenko, et al., Detailed Report of the MuLan Measurement of the Positive Muon Lifetime and Determination of the Fermi Constant, Phys. Rev. D87 (5) (2013) 052003. arXiv:1211.0960, doi:10.1103/PhysRevD.87.052003.

[72] S. Bethke, World Summary of α_s (2012)[Nucl. Phys. Proc. Suppl.234,229(2013)] (2012). arXiv:1210.0325, doi:10.1016/j.nuclphysbps.2012.12.020.

[73] D. Buttazzo, G. Degrassi, P. P. Giardino, G. F. Giudice, F. Sala, A. Salvio, A. Strumia, Investigating the near-criticality of the Higgs boson, JHEP 12 (2013) 089. arXiv:1307.3536, doi:10.1007/JHEP12(2013)089.

[74] J. R. Ellis, K. Enqvist, D. V. Nanopoulos, F. Zwirner, Observables in Low-Energy Superstring Models, Mod. Phys. Lett. A1 (1986) 57. doi:10.1142/S0217732386000105.

[75] R. Barbieri, G. F. Giudice, Upper Bounds on Supersymmetric Particle Masses, Nucl. Phys. B306 (1988) 63–76. doi:10.1016/0550-3213(88)90171-X.

[76] G. F. Giudice, A. Masiero, A Natural Solution to the mu Problem in Supergravity Theories, Phys. Lett. B206 (1988) 480–484. doi:10.1016/0370-2693(88)91613-9.

[77] J. L. Feng, T. Moroi, Supernatural supersymmetry: Phenomenological implications of anomaly mediated supersymmetry breaking, Phys. Rev. D61 (2000) 095004. arXiv:hep-ph/9907319, doi:10.1103/PhysRevD.61.095004.

[78] J. L. Feng, K. T. Matchev, T. Moroi, Multi - TeV scalars are natural in minimal supergravity, Phys. Rev. Lett. 84 (2000) 2322–2325. arXiv:hep-ph/9908309, doi:10.1103/PhysRevLett.84.2322.

[79] J. L. Feng, K. T. Matchev, T. Moroi, Focus points and naturalness in supersymmetry, Phys. Rev. D61 (2000) 075005. arXiv:hep-ph/9909334, doi:10.1103/PhysRevD.61.075005.

[80] M. Ibe, T. Moroi, T. T. Yanagida, Possible Signals of Wino LSP at the Large Hadron Collider, Phys. Lett. B644 (2007) 355–360. arXiv:hep-ph/0610277, doi:10.1016/j.physletb.2006.11.061.

[81] M. Ibe, T. T. Yanagida, The Lightest Higgs Boson Mass in Pure Gravity Mediation Model, Phys. Lett. B709 (2012) 374–380. arXiv:1112.2462, doi:10.1016/j.physletb.2012.02.034.

[82] N. Arkani-Hamed, A. Gupta, D. E. Kaplan, N. Weiner, T. Zorawski, Simply Unnatural Supersymmetry (2012). arXiv:1212.6971.

[83] M. Cirelli, N. Fornengo, A. Strumia, Minimal dark matter, Nucl. Phys. B753 (2006) 178–194. arXiv:hep-ph/0512090, doi:10.1016/j.nuclphysb.2006.07.012.

[84] M. Cirelli, A. Strumia, M. Tamburini, Cosmology and Astrophysics of Minimal Dark Matter, Nucl. Phys. B787 (2007) 152–175. arXiv:0706.4071, doi:10.1016/j.nuclphysb.2007.07.023.

[85] M. Cirelli, A. Strumia, Minimal Dark Matter: Model and results, New J. Phys. 11 (2009) 105005. arXiv:0903.3381, doi:10.1088/1367-2630/11/10/105005.

[86] M. E. Machacek, M. T. Vaughn, Two Loop Renormalization Group Equations in a General Quantum Field Theory. 1. Wave Function Renormalization, Nucl. Phys. B222 (1983) 83–103. doi:10.1016/0550-3213(83)90610-7.

[87] M. Farina, D. Pappadopulo, A. Strumia, A modified naturalness principle and its experimental tests, JHEP 08 (2013) 022. arXiv:1303.7244, doi:10.1007/JHEP08(2013)022.

[88] L. Di Luzio, R. Gröber, J. F. Kamenik, M. Nardecchia, Accidental matter at the LHC, JHEP 07 (2015) 074. arXiv:1504.00359, doi:10.1007/JHEP07(2015)074.

[89] E. Del Nobile, M. Nardecchia, P. Panci, Millicharge or Decay: A Critical Take on Minimal Dark Matter, JCAP 1604 (04) (2016) 048. arXiv:1512.05353, doi:10.1088/1475-7516/2016/04/048.

[90] T. Gherghetta, G. F. Giudice, J. D. Wells, Phenomenological consequences of supersymmetry with anomaly induced masses, Nucl. Phys. B559 (1999) 27–47. arXiv:hep-ph/9904378, doi:10.1016/S0550-3213(99)00429-0.

[91] H. Fukuda, N. Nagata, H. Otono, S. Shirai, Higgsino Dark Matter or Not: Role of Disappearing Track Searches at the LHC and Future Colliders, Phys. Lett. B781 (2018) 306–311. arXiv:1703.09675, doi:10.1016/j.physletb.2018.03.088.

[92] M. Ibe, S. Matsumoto, R. Sato, Mass Splitting between Charged and Neutral Winos at Two-Loop Level, Phys. Lett. B721 (2013) 252–260. arXiv:1212.5989, doi:10.1016/j.physletb.2013.03.015.

[93] N. Arkani-Hamed, A. Delgado, G. F. Giudice, The Well-tempered neutralino, Nucl. Phys. B741 (2006) 108–130. arXiv:hep-ph/0601041, doi:10.1016/j.nuclphysb.2006.02.010.

[94] J. Hisano, S. Matsumoto, M. Nagai, O. Saito, M. Senami, Non-perturbative effect on thermal relic abundance of dark matter, Phys. Lett. B646 (2007) 34–38. arXiv:hep-ph/0610249, doi:10.1016/j.physletb.2007.01.012.

[95] T. Moroi, M. Nagai, M. Takimoto, Non-Thermal Production of Wino Dark Matter via the Decay of Long-Lived Particles, JHEP 07 (2013) 066. arXiv:1303.0948, doi:10.1007/JHEP07(2013)066.

[96] M. Beneke, A. Bharucha, F. Dighera, C. Hellmann, A. Hryczuk, S. Recksiegel, P. Ruiz-Femenia, Relic density of wino-like dark matter in the MSSM, JHEP 03 (2016) 119. arXiv:1601.04718, doi:10.1007/JHEP03(2016)119.

[97] F. Zwicky, Die Rotverschiebung von extragalaktischen Nebeln, Helvetica Physica Acta 6 (1933) 110.

[98] F. Zwicky, On the Masses of Nebulae and of Clusters of Nebulae, Astrophysical Journal 86 (1937) 217.

[99] V. Trimble, Existence and Nature of Dark Matter in the Universe, Ann. Rev. Astron. Astrophys. 25 (1987) 425–472. doi:10.1146/annurev.aa.25.090187.002233.

[100] H. W. Babcock, The rotation of the Andromeda Nebula, Lick Observatory Bulletin 19 (1939) 41–51. doi:10.5479/ADS/bib/1939LicOB.19.41B.

[101] K. G. Begeman, A. H. Broeils, R. H. Sanders, Extended rotation curves of spiral galaxies: Dark haloes and modified dynamics, Mon. Not. Roy. Astron. Soc. 249 (1991) 523.

[102] G. Jungman, M. Kamionkowski, A. Kosowsky, D. N. Spergel, Weighing the universe with the cosmic microwave background, Phys. Rev. Lett. 76 (1996) 1007–1010. arXiv:astro-ph/9507080, doi:10.1103/PhysRevLett.76.1007.

[103] G. Jungman, M. Kamionkowski, A. Kosowsky, D. N. Spergel, Cosmological parameter determination with microwave background maps, Phys. Rev. D54 (1996) 1332–1344. `arXiv:astro-ph/9512139`, `doi:10.1103/PhysRevD.54.1332`.

[104] N. Aghanim, et al., Planck 2018 results. VI. Cosmological parameters (2018). `arXiv:1807.06209`.

[105] P. Gondolo, G. Gelmini, Cosmic abundances of stable particles: Improved analysis, Nucl. Phys. B360 (1991) 145–179. `doi:10.1016/0550-3213(91)90438-4`.

[106] G. Bélanger, F. Boudjema, A. Pukhov, A. Semenov, MicrOMEGAs: A Program for calculating the relic density in the MSSM, Comput. Phys. Commun. 149 (2002) 103–120. `arXiv:hep-ph/0112278`, `doi:10.1016/S0010-4655(02)00596-9`.

[107] G. Bélanger, F. Boudjema, A. Goudelis, A. Pukhov, B. Zaldivar, micrOMEGAs5.0 : Freeze-in, Comput. Phys. Commun. 231 (2018) 173–186. `arXiv:1801.03509`, `doi:10.1016/j.cpc.2018.04.027`.

[108] J. Hisano, S. Matsumoto, M. M. Nojiri, O. Saito, Non-perturbative effect on dark matter annihilation and gamma ray signature from galactic center, Phys. Rev. D71 (2005) 063528. `arXiv:hep-ph/0412403`, `doi:10.1103/PhysRevD.71.063528`.

[109] T. Marrodán Undagoitia, L. Rauch, Dark matter direct-detection experiments, J. Phys. G43 (1) (2016) 013001. `arXiv:1509.08767`, `doi:10.1088/0954-3899/43/1/013001`.

[110] M. W. Goodman, E. Witten, Detectability of Certain Dark Matter Candidates, Phys. Rev. D31 (1985) 3059, [,325(1984)]. `doi:10.1103/PhysRevD.31.3059`.

[111] E. Aprile, The XENON1T Dark Matter Search Experiment, Springer Proc. Phys. 148 (2013) 93–96. `arXiv:1206.6288`, `doi:10.1007/978-94-007-7241-0_14`.

[112] F. J. Kerr, D. Lynden-Bell, Review of galactic constants, Mon. Not. Roy. Astron. Soc. 221 (1986) 1023.

[113] A. M. Green, Astrophysical uncertainties on direct detection experiments, Mod. Phys. Lett. A27 (2012) 1230004. `arXiv:1112.0524`, `doi:10.1142/S0217732312300042`.

[114] M. C. Smith, et al., The RAVE Survey: Constraining the Local Galactic Escape Speed, Mon. Not. Roy. Astron. Soc. 379 (2007) 755–772. `arXiv:astro-ph/0611671`, `doi:10.1111/j.1365-2966.2007.11964.x`.

[115] J. D. Lewin, P. F. Smith, Review of mathematics, numerical factors, and corrections for dark matter experiments based on elastic nuclear recoil, Astropart. Phys. 6 (1996) 87–112. `doi:10.1016/S0927-6505(96)00047-3`.

[116] J. Billard, L. Strigari, E. Figueroa-Feliciano, Implication of neutrino backgrounds on the reach of next generation dark matter direct detection experiments, Phys. Rev. D89 (2) (2014) 023524. arXiv:1307.5458, doi:10.1103/PhysRevD.89.023524.

[117] L. Roszkowski, E. M. Sessolo, A. J. Williams, What next for the CMSSM and the NUHM: Improved prospects for superpartner and dark matter detection, JHEP 08 (2014) 067. arXiv:1405.4289, doi:10.1007/JHEP08(2014)067.

[118] J. M. Gaskins, A review of indirect searches for particle dark matter, Contemp. Phys. 57 (4) (2016) 496–525. arXiv:1604.00014, doi:10.1080/00107514.2016.1175160.

[119] J. F. Navarro, C. S. Frenk, S. D. M. White, The Structure of cold dark matter halos, Astrophys. J. 462 (1996) 563–575. arXiv:astro-ph/9508025, doi:10.1086/177173.

[120] J. F. Navarro, C. S. Frenk, S. D. M. White, A Universal density profile from hierarchical clustering, Astrophys. J. 490 (1997) 493–508. arXiv:astro-ph/9611107, doi:10.1086/304888.

[121] M. Fornasa, A. M. Green, Self-consistent phase-space distribution function for the anisotropic dark matter halo of the Milky Way, Phys. Rev. D89 (6) (2014) 063531. arXiv:1311.5477, doi:10.1103/PhysRevD.89.063531.

[122] A. Genina, A. Benítez-Llambay, C. S. Frenk, S. Cole, A. Fattahi, J. F. Navarro, K. A. Oman, T. Sawala, T. Theuns, The core - cusp problem: a matter of perspective, Monthly Notices of the Royal Astronomical Society 474 (1) (2017) 1398 - 1411. doi:10.1093/mnras/stx2855.
URL http://dx.doi.org/10.1093/mnras/stx2855

[123] J. Einasto, On the Construction of a Composite Model for the Galaxy and on the Determination of the System of Galactic Parameters, Trudy Astrofizicheskogo Instituta Alma-Ata 5 (1965) 87–100.

[124] A. W. Graham, D. Merritt, B. Moore, J. Diemand, B. Terzic, Empirical models for Dark Matter Halos. I. Nonparametric Construction of Density Profiles and Comparison with Parametric Models, Astron. J. 132 (2006) 2685–2700. arXiv:astro-ph/0509417, doi:10.1086/508988.

[125] A. Burkert, The Structure of dark matter halos in dwarf galaxies, IAU Symp. 171 (1996) 175, [Astrophys. J.447,L25(1995)]. arXiv:astro-ph/9504041, doi:10.1086/309560.

[126] A. Geringer-Sameth, S. M. Koushiappas, M. Walker, Dwarf galaxy annihilation and decay emission profiles for dark matter experiments, Astrophys. J. 801 (2) (2015) 74. arXiv:1408.0002, doi:10.1088/0004-637X/801/2/74.

[127] M. A. S¥ 'anchez-Conde, M. Cannoni, F. Zandanel, M. E. G¥ 'omez, F. Prada, Dark matter searches with cherenkov telescopes: nearby dwarf galaxies or local galaxy clusters?, Journal of Cosmology and Astroparticle Physics 2011 (12) (2011) 011–011. doi:10.1088/1475-7516/2011/12/011.
URL https://doi.org/10.1088%2F1475-7516%2F2011%2F12%2F011

[128] L. Roszkowski, E. M. Sessolo, S. Trojanowski, WIMP dark matter candidates and searches—current status and future prospects, Rept. Prog. Phys. 81 (6) (2018) 066201. arXiv:1707.06277, doi:10.1088/1361-6633/aab913.

[129] M. Benedikt, M. Capeans Garrido, F. Cerutti, B. Goddard, J. Gutleber, J. M. Jimenez, M. Mangano, V. Mertens, J. A. Osborne, T. Otto, J. Poole, W. Riegler, D. Schulte, L. J. Tavian, D. Tommasini, F. Zimmermann, Future Circular Collider, Tech. Rep. CERN-ACC-2018-0058, CERN, Geneva, submitted for publication to Eur. Phys. J. ST. (Dec 2018).
URL https://cds.cern.ch/record/2651300

[130] D. Binosi, J. Collins, C. Kaufhold, L. Theussl, Jaxodraw: A graphical user interface for drawing feynman diagrams. version 2.0 release notes, Computer Physics Communications 180 (9) (2009) 1709 – 1715. doi:https://doi.org/10.1016/j.cpc.2009.02.020.
URL http://www.sciencedirect.com/science/article/pii/S0010465509000757

[131] J. Vermaseren, Axodraw, Computer Physics Communications 83 (1) (1994) 45 – 58. doi:https://doi.org/10.1016/0010-4655(94)90034-5.
URL http://www.sciencedirect.com/science/article/pii/0010465594900345

[132] J. Gao, L. Harland-Lang, J. Rojo, The Structure of the Proton in the LHC Precision Era, Phys. Rept. 742 (2018) 1–121. arXiv:1709.04922, doi:10.1016/j.physrep.2018.03.002.

[133] K. Kovařík, P. M. Nadolsky, D. E. Soper, Hadron structure in high-energy collisions (2019). arXiv:1905.06957.

[134] V. N. Gribov, L. N. Lipatov, Deep inelastic e p scattering in perturbation theory, Sov. J. Nucl. Phys. 15 (1972) 438–450, [Yad. Fiz.15,781(1972)].

[135] L. N. Lipatov, The parton model and perturbation theory, Sov. J. Nucl. Phys. 20 (1975) 94–102, [Yad. Fiz.20,181(1974)].

[136] G. Altarelli, G. Parisi, Asymptotic Freedom in Parton Language, Nucl. Phys. B126 (1977) 298–318. `doi:10.1016/0550-3213(77)90384-4`.

[137] Y. L. Dokshitzer, Calculation of the Structure Functions for Deep Inelastic Scattering and e+ e- Annihilation by Perturbation Theory in Quantum Chromodynamics., Sov. Phys. JETP 46 (1977) 641–653, [Zh. Eksp. Teor. Fiz.73,1216(1977)].

[138] J. Alwall, M. Herquet, F. Maltoni, O. Mattelaer, T. Stelzer, MadGraph 5 : Going Beyond, JHEP 06 (2011) 128. `arXiv:1106.0522`, `doi:10.1007/JHEP06(2011)128`.

[139] J. Alwall, R. Frederix, S. Frixione, V. Hirschi, F. Maltoni, O. Mattelaer, H. S. Shao, T. Stelzer, P. Torrielli, M. Zaro, The automated computation of tree-level and next-to-leading order differential cross sections, and their matching to parton shower simulations, JHEP 07 (2014) 079. `arXiv:1405.0301`, `doi:10.1007/JHEP07(2014)079`.

[140] T. Sjöstrand, S. Ask, J. R. Christiansen, R. Corke, N. Desai, P. Ilten, S. Mrenna, S. Prestel, C. O. Rasmussen, P. Z. Skands, An Introduction to PYTHIA 8.2, Comput. Phys. Commun. 191 (2015) 159–177. `arXiv:1410.3012`, `doi:10.1016/j.cpc.2015.01.024`.

[141] J. de Favereau, C. Delaere, P. Demin, A. Giammanco, V. Lemaître, A. Mertens, M. Selvaggi, DELPHES 3, A modular framework for fast simulation of a generic collider experiment, JHEP 02 (2014) 057. `arXiv:1307.6346`, `doi:10.1007/JHEP02(2014)057`.

[142] M. L. Mangano, M. Moretti, F. Piccinini, M. Treccani, Matching matrix elements and shower evolution for top-quark production in hadronic collisions, JHEP 01 (2007) 013. `arXiv:hep-ph/0611129`, `doi:10.1088/1126-6708/2007/01/013`.

[143] R. D. Ball, V. Bertone, S. Carrazza, L. Del Debbio, S. Forte, A. Guffanti, N. P. Hartland, J. Rojo, Parton distributions with QED corrections, Nucl. Phys. B877 (2013) 290–320. `arXiv:1308.0598`, `doi:10.1016/j.nuclphysb.2013.10.010`.

[144] S. Asai, S. Chigusa, T. Kaji, T. Moroi, M. Saito, R. Sawada, J. Tanaka, K. Terashi, K. Uno, Studying gaugino masses in supersymmetric model at future 100 TeV pp collider, JHEP 05 (2019) 179. `arXiv:1901.10389`, `doi:10.1007/JHEP05(2019)179`.

[145] C. H. Chen, M. Drees, J. F. Gunion, Searching for invisible and almost invisible particles at e+ e- colliders, Phys. Rev. Lett. 76 (1996) 2002–2005. `arXiv:hep-ph/9512230`, `doi:10.1103/PhysRevLett.76.2002`.

[146] S. D. Thomas, J. D. Wells, Phenomenology of Massive Vectorlike Doublet Leptons, Phys. Rev. Lett. 81 (1998) 34–37. arXiv:hep-ph/9804359, doi:10.1103/PhysRevLett.81.34.

[147] M. Capeans, G. Darbo, K. Einsweiller, M. Elsing, T. Flick, M. Garcia-Sciveres, C. Gemme, H. Pernegger, O. Rohne, R. Vuillermet, ATLAS Insertable B-Layer Technical Design Report, Tech. Rep. CERN-LHCC-2010-013. ATLAS-TDR-19 (Sep 2010).
URL https://cds.cern.ch/record/1291633

[148] ATLAS Insertable B-Layer Technical Design Report Addendum, Tech. Rep. CERN-LHCC-2012-009. ATLAS-TDR-19-ADD-1, addendum to CERN-LHCC-2010-013, ATLAS-TDR-019 (May 2012).
URL https://cds.cern.ch/record/1451888

[149] B. Abbott, et al., Production and Integration of the ATLAS Insertable B-Layer, JINST 13 (05) (2018) T05008. arXiv:1803.00844, doi:10.1088/1748-0221/13/05/T05008.

[150] M. Saito, R. Sawada, K. Terashi, S. Asai, Discovery reach for wino and higgsino dark matter with a disappearing track signature at a 100 TeV pp collider, Eur. Phys. J. C79 (6) (2019) 469. arXiv:1901.02987, doi:10.1140/epjc/s10052-019-6974-2.

[151] J. M. Lindert, et al., Precise predictions for $V+$ jets dark matter backgrounds, Eur. Phys. J. C77 (12) (2017) 829. arXiv:1705.04664, doi:10.1140/epjc/s10052-017-5389-1.

[152] M. Aaboud, et al., Search for dark matter and other new phenomena in events with an energetic jet and large missing transverse momentum using the ATLAS detector, JHEP 01 (2018) 126. arXiv:1711.03301, doi:10.1007/JHEP01(2018)126.

[153] L. Di Luzio, R. Gröber, G. Panico, Probing new electroweak states via precision measurements at the LHC and future colliders, JHEP 01 (2019) 011. arXiv:1810.10993, doi:10.1007/JHEP01(2019)011.

[154] S. Matsumoto, S. Shirai, M. Takeuchi, Indirect Probe of Electroweak-Interacting Particles with Mono-Lepton Signatures at Hadron Colliders (2018). arXiv:1810.12234.

[155] M. Aaboud, et al., Search for a new heavy gauge boson resonance decaying into a lepton and missing transverse momentum in 36 fb^{-1} of pp collisions at $\sqrt{s} = 13$ TeV with the ATLAS experiment, Eur. Phys. J. C78 (5) (2018) 401. arXiv:1706.04786, doi:10.1140/epjc/s10052-018-5877-y.

[156] A. M. Sirunyan, et al., Search for high-mass resonances in final states with a lepton and missing transverse momentum at $\sqrt{s}$ = 13 TeV, JHEP 06 (2018) 128. `arXiv:1803.11133`, `doi:10.1007/JHEP06(2018)128`.

[157] T. Aaltonen, et al., Search for new particles decaying into dijets in proton-antiproton collisions at s**(1/2) = 1.96-TeV, Phys. Rev. D79 (2009) 112002. `arXiv:0812.4036`, `doi:10.1103/PhysRevD.79.112002`.

[158] G. Cowan, K. Cranmer, E. Gross, O. Vitells, Asymptotic formulae for likelihood-based tests of new physics, Eur. Phys. J. C71 (2011) 1554, [Erratum: Eur. Phys. J.C73,2501(2013)]. `arXiv:1007.1727`, `doi:10.1140/epjc/s10052-011-1554-0,10.1140/epjc/s10052-013-2501-z`.

[159] A. Buckley, J. Ferrando, S. Lloyd, K. Nordström, B. Page, M. Rüfenacht, M. Schönherr, G. Watt, LHAPDF6: parton density access in the LHC precision era, Eur. Phys. J. C75 (2015) 132. `arXiv:1412.7420`, `doi:10.1140/epjc/s10052-015-3318-8`.

[160] J. Wess, J. A. Bagger, Supersymmetry and supergravity; 2nd ed., Princeton Series in Physics, Princeton Univ. Press, Princeton, NJ, 1992.
URL `https://cds.cern.ch/record/320631`

[161] A. Alloul, N. D. Christensen, C. Degrande, C. Duhr, B. Fuks, FeynRules 2.0 - A complete toolbox for tree-level phenomenology, Comput. Phys. Commun. 185 (2014) 2250–2300. `arXiv:1310.1921`, `doi:10.1016/j.cpc.2014.04.012`.

[162] A. Alloul, N. D. Christensen, C. Degrande, C. Duhr, B. Fuks, FeynRules model database.
URL `https://feynrules.irmp.ucl.ac.be/wiki/ModelDatabaseMainPage`

[163] C. Degrande, C. Duhr, B. Fuks, D. Grellscheid, O. Mattelaer, T. Reiter, UFO - The Universal FeynRules Output, Comput. Phys. Commun. 183 (2012) 1201–1214. `arXiv:1108.2040`, `doi:10.1016/j.cpc.2012.01.022`.

[164] S. Iwamoto, FeynLecture: Tools for BSM Physics.
URL `https://www.misho-web.com/phys/feynlecture.html`

[165] F. James, MINUIT Function Minimization and Error Analysis: Reference Manual Version 94.1 (1994).

[166] S. S. Wilks, The large-sample distribution of the likelihood ratio for testing composite hypotheses, Ann. Math. Statist. 9 (1) (1938) 60–62. `doi:10.1214/aoms/1177732360`.
URL `https://doi.org/10.1214/aoms/1177732360`